NORTH ATLANTIC AIR-SEA INTERACTIONS DRIVEN BY ATMOSPHERIC AND OCEANIC STOCHASTIC FORCING IN A SIMPLE BOX MODEL

A

THESIS

Presented to the Faculty
of the University of Alaska Fairbanks
in Partial Fulfillment of the Requirements
for the Degree of

MASTER OF SCIENCE

By
Rebecca Anne Legatt, B.S.

Fairbanks, Alaska
December 2010

Abstract

North Atlantic (NA) variability has wide-spread implications locally and globally. This study investigates mechanisms driving NA variability using a simple box model incorporating time evolution of interacting upper ocean temperature anomalies, horizontal (Gyre) and vertical (meridional overturning circulation, or MOC) circulation, driven by surface air temperature, wind, and Labrador Sea temperature forcings. Simulated upper ocean responses to external atmospheric forcing result in solutions with redder spectra than solutions by white noise atmospheric forcing, implying that the ocean acts as a low-pass filter to this external forcing. Simulated ocean dynamic response may be viewed as a response to a cumulative atmospheric forcing over an interval defined by system damping properties. A strong anti-correlation links simulated MOC and Gyre circulation intensity suggesting a mechanism, in which system heat balance is maintained via communication between the dynamic components, (e.g. excess of heat supply from a stronger Gyre circulation would be balanced by lack of heat from a weaker MOC circulation and vise versa). Wind was the dominant forcing for NA upper ocean temperature anomalies and the intensity of MOC and Gyre circulations. Further investigations of NA variability mechanisms are important as they have serious implications on global heat transport.

Table Contents

Page

Page

List of Figures

Page

List of Tables

Page

List of Appendices

Page

Acknowledgements

There are many individuals that I would like to acknowledge for supporting me during my graduate studies in Alaska. My success here was only made possible by the guidance and support of everyone that is a part of my life and for that I am truly grateful.

First I would like to specially thank my advisor, Dr. Igor Polyakov, for taking a chance on a small-town undergraduate from North Dakota. I am truly grateful that he challenged me to excel in my research project, offering steady guidance, encouragement and patience along the way. I feel lucky to have had the opportunity to work with such an outstanding scientist. I am also truly grateful to Dr. Polyakov for offering me the opportunity to work on the research team for the 2009 Nansen and Amundsen Basin Observational Systems cruise.

I would also like to thank my committee members, Dr. Uma Bhatt and Dr. Xiangdong Zhang for the guidance and support provided during the completion of my thesis and for fruitful discussions during committee meetings. In addition I would like to thank Dr. Nicole Mölders for her support and feedback while completing my thesis, and Barbara Day in the Department of Atmospheric Sciences for answering numerous questions and providing assistance through the years.

I am truly appreciative for the many productive discussions and suggestions regarding Hurst analysis shared with Dr. David Newman from the Department of Physics. He also shared several codes that were utilized in generating external model forcings and answered many questions along the way. I am also very grateful for the fruitful signal processing and analytical solution discussions that were shared with Dr. Roman Bekryaev from Voeikov Main Geophysical Observatory, and St. Petersburg State University in St. Petersburg, Russia.

I thank Dr. Larry Hinzman and the support staff at the International Arctic Research Center for support of my studies. I also thank IARC for funding my travels

to the State of the Arctic Meeting and participation in the 2009 International Polar Year Polar Field School at the University Center in Svalbard.

I would like to thank Dr. Uma Bhatt for checking in on me during tough times, offering some of the best advice and feedback when the "going got tough". In graduate school I have learned that your fellow graduate students become your second family, and I would like to thank them so very much for their support and encouragement, especially Anna Liljedahl, Ashley Wallace, Austin Cross, Julie Malingowski, Oceana Francis, and Jeanie Talbot. In addition I would like to thank my weekend fishing friends and other amazing people I have met on the road while exploring Alaska in my time off.

Last, but definitely not least, I would like to thank my mom, Shirley Legatt, my dad, August Legatt, and my brother, Luke Legatt for their incredible support. Countless phone calls of encouragement and packages sent in the mail kept me going. The famous family quotes from my dad "Go Get 'Em" and "God is testing you" echoed in my mind and kept me going on my most challenging days. Without their loving support I would not have been able to accomplish the goals I have set thus far in life.

1. Introduction

1.1 General overview of the North Atlantic Ocean

Extending northward from the Equator to a latitude near 70°N is the North Atlantic Ocean (Figure 1.1). The ocean is physically bound to the north by the islands of Greenland and Iceland, as well as the Labrador, Greenland, and Norwegian Seas. This basin is confined to the west at approximately 75°W by the northern coast of Brazil, the eastern limits of the Caribbean Sea and Gulf of Mexico, and the east coast of North America. The eastern extent of the basin is located near 15°W, and is bound by the west coast of Africa and Europe, and the Straight of Gibraltar. While the Atlantic Ocean extends south towards the shelf of Antarctica, the southern extent of the North Atlantic Ocean is physically limited to the Equator.

Figure 1.1 Bathymetry map of the North Atlantic. From Encyclopædia Britannica, 2010.

The bathymetry of the North Atlantic Ocean is displayed in Figure 1.1 with the continental shelves of bordering continents sloping down to the depths of the North American and Cape Verde Basins. The Mid-Atlantic Ridge dividing these basins has formed as the North American and Eurasian tectonic plates moved apart since Jurassic times. The mid-ocean spreading resulted in the ridge that curves through the North Atlantic starting just northeast of Greenland and extending through the South Atlantic Ocean. The average depth of the ocean plains ranges from approximately 3,700 to 5,500 meters (Encyclopædia Britannica, 2010), while locations along the Mid-Atlantic Ridge are much shallower with portions of the ridge even extending above sea level in Iceland to form the Reykjanes Ridge (Redfern, 2001).

Prevailing wind patterns over the North Atlantic exert stress on the ocean surface, influencing the dominant surface ocean currents. The Northeast trade winds drive surface waters near the equator westward across the North Atlantic Basin in the North Equatorial Current (Figure 1.2) with a maximum stress exerted on the surface near 15°N (Tomczak and Godfrey, 2003). This current transports surface waters to the west where they encounter the continental shelf of North America and feed the Florida and Antilles Current.

The Florida Current flows through the Yukatan Strait and enters the Gulf of Mexico with a mean water transport rate of 30 Sv (Tomczak and Godfrey, 2003; Wunsch and Roemmich, 1985), while the Antilles Current passes to the east of the Caribbean Islands. These two currents combine off the East Coast of Florida to feed the Gulf Stream Current, flowing along the bathymetry of the East Coast of the US with a transport rate of 70 - 100 Sv (Tomczak and Godfrey, 2003).

At approximately 35°N, near Cape Hatteras, North Carolina, this western boundary current departs from the continental shelf of North America. It is the strongest current in the basin with transport rates accelerating as the current departs from the continental shelf to a maximum near 55°W of 150 Sv (Hendry 1982; Hogg, 1992; Tomczak and Godfrey, 2003).

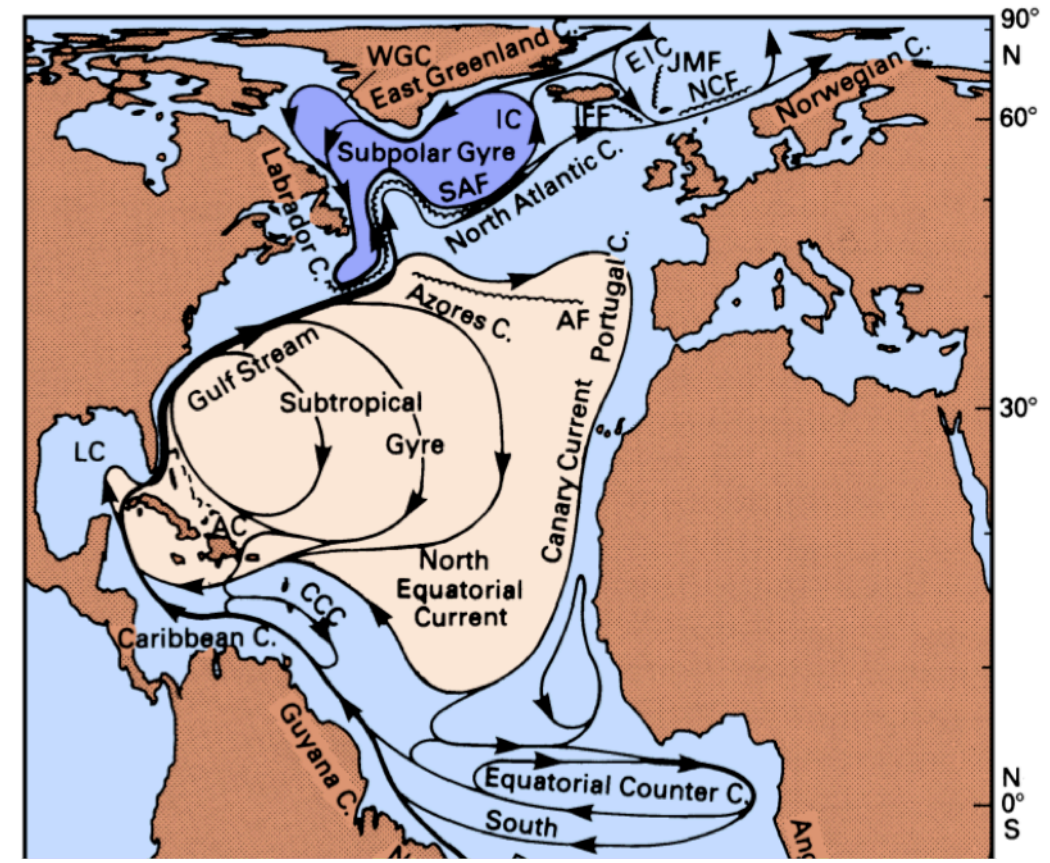

Figure 1.2 Map of North Atlantic Ocean surface currents. From Tomczak and Godfrey, 2003.

From approximately 30°N to 55°N the prevailing westerly winds dominate the atmosphere exerting stress on the ocean surface across the basin from the southwest to the northeast. The strength of this wind pattern is dependent upon the sea level pressure (SLP) gradient between the Azores High and Icelandic Low, expressed as the North Atlantic Oscillation index, or NAO (Walker, 1924; Marshall et al., 2001a; Hurrell et al., 2003). During winter months the largest temperature gradients are present, causing the deepening of the Icelandic Low and the enhancement of the Azores High. Periods of enhanced (weakened) SLP gradient are described by the positive phase of the NAO (negative phase of the NAO), which cause stronger (weaker) westerly winds and enhance (weaken) the Gulf Stream Current.

As the Gulf Stream extends northeast across the basin a section is deflected eastward in the Azores Current to continue in the Canary Current completing the

Subtropical Gyre, while the main current continues to the Norwegian Seas from approximately 35°N to 60°N, transporting a net northward heat flux of 1.2 PW (1 PW = 10^{15} W) from the mid to high latitudes (Hall and Bryden, 1982; Roemmich and Wunsch, 1985; Lavin et al., 1998). The northern branch of the extended Gulf Current is once again split here, with one current branch following the bathymetry of the western Iceland continental shelf, turning towards the west as it is influenced by the polar easterly winds forming the Subpolar Gyre. The other branch of the extended Gulf Current feeds the Norwegian Current passing along the west coast of Scandenavia, where the surface water mass is transformed due to local processes.

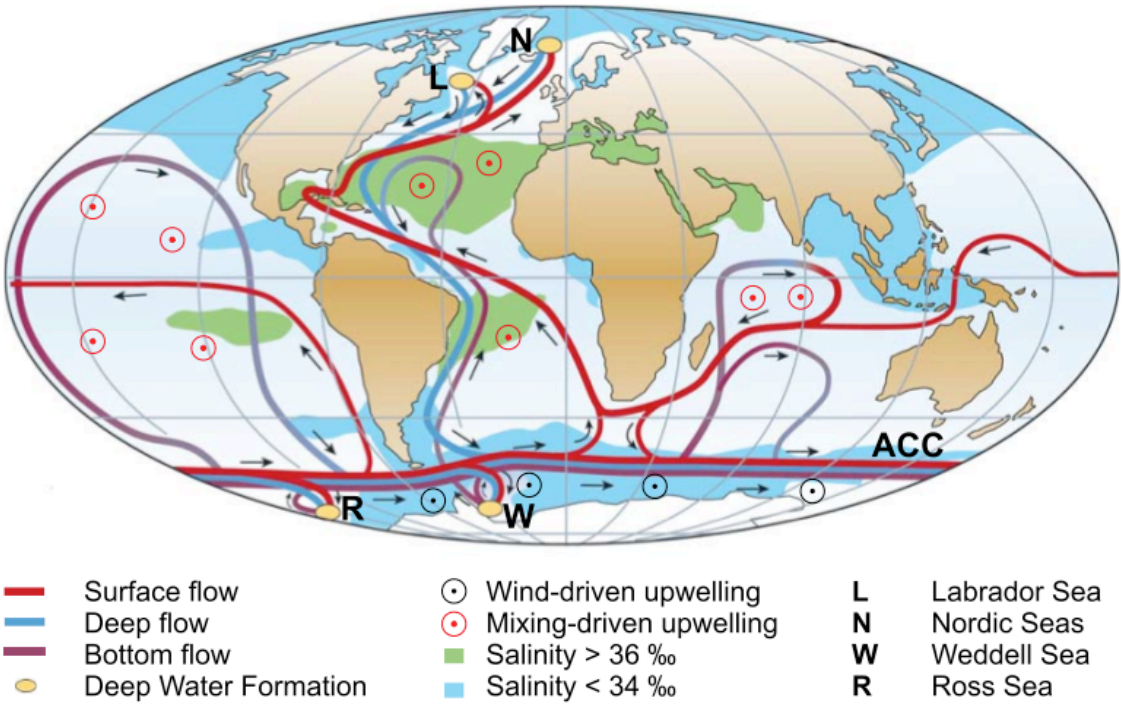

Figure 1.3 Diagram of global ocean circulation. Surface flows are shown in red, deep flows are shown in blue, and bottom flows are shown in purple. From Schmittner et al., 2007.

The net meridional heat transport by these surface currents is responsible for the moderate climates of Europe and Scandinavia (Hurrell et al., 2003; Schmittner et al., 2007) and it is also an important surface component of a large-scale vertical ocean circulation belt known as the Meridional Overturning

Circulation (MOC; Marshall et al., 2001a), which is driven by differences in the densities of ocean water masses in the North Atlantic. The MOC is one of the main mechanisms driving the overall global ocean conveyor belt (Figure 1.3), which effectively transports heat through the oceans worldwide (Schmittner et al., 2007).

1.2 North Atlantic water masses

Due to redistribution of waters with oceanic circulation, air-sea interactions, and atmospheric forcing, ocean waters contained in the North Atlantic are not uniform. Distinct properties like temperature, salinity and oxygen concentration distinguish water masses of different origins, and as a result the water column may be broken into layers such as the North Atlantic Deep Water (NADW), Labrador Sea Water (LA), Greenland Sea Water (GS), and Eurafrican Mediterranean Water (EMW) according to variations in these properties (Figure 1.4).

The ocean's mixed layer is characterized as a surface layer of relatively uniform density where the direct impact of atmospheric forcing is clearly seen in water properties (Marshall and Plumb, 2008). In the tropics there is strong absorption of incoming solar radiation, and precipitation dominates evaporation (Tomczak and Godfrey, 2003). High sea surface temperature (SST) at low latitudes (seen in the shallow warm layer greater than or equal to 20°C in the top panel of Figure 1.4 between 20°S and 20°N) causes an increase in sea level height with decreasing surface density, resulting in a fairly stable and shallow mixed layer.

In the sub-tropical region near 20-35°N, dominated by easterly winds, evaporation exceeds precipitation and salinity plays a key role in determining the depth of the mixed layer. The surface water here is still warm, but as freshwater leaves the ocean surface through evaporation, the surface water becomes more saline with values greater than 35 psu, leading to a deeper mixed layer (middle panel of Figure 1.4; Marshall and Plumb, 2008). The Straight of Gibraltar is also located in this sub-tropical region, which allows the very saline waters from the Mediterranean Sea to enter the North Atlantic Basin. This water mass is identified

by its moderate temperatures and high salinity as the EMW layer, characterized by a potential temperature of 4°C and a salinity of 35.5 psu (middle panel of Figure 1.4; Tomczak and Godfrey, 2003). This water mass gathers in this intermediate layer of the Atlantic because it is denser than the surface mixed layer due to salinity properties, but it is less dense than the NADW due to thermal properties.

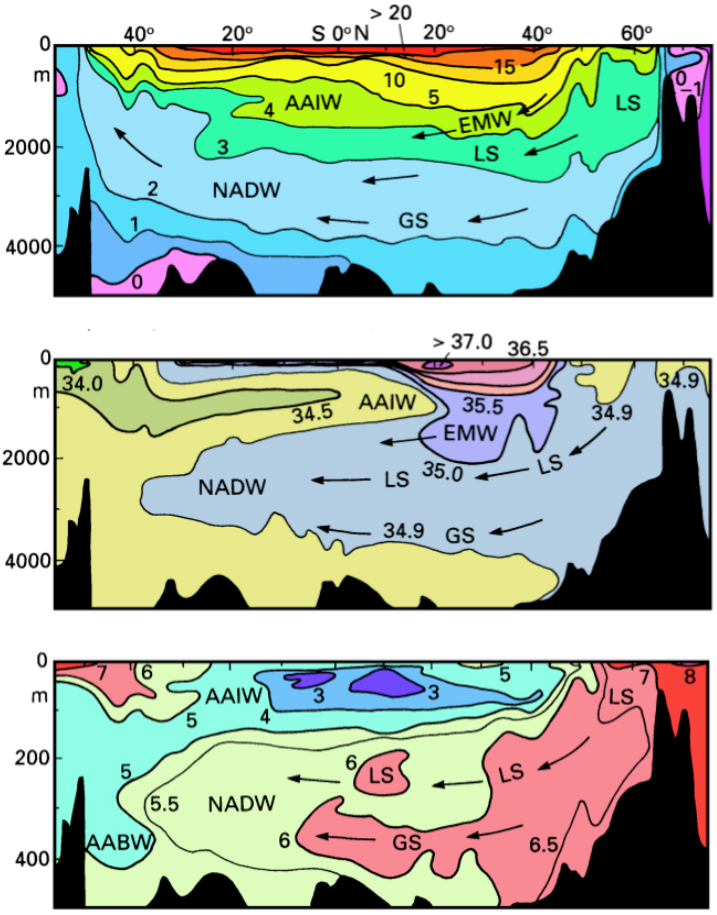

Figure 1.4 Cross-sectional North Atlantic profiles of (top) potential temperature (C), (Middle) salinity (psu), and (bottom) oxygen concentration (ml/l) for the Atlantic Ocean at approximately 45°W. Arrows indicate direction of water transport. Labeled water masses include: North Atlantic Deep Water (NADW), Antarctic Intermediate Water (AAIW), Eurafrican Mediterranean Water (EMW), Labrador Sea Water (LS), Greenland Sea Water (GS), and the Antarctic Bottom Water (AABW). From Tomczak and Godfrey, 2003.

In mid latitudes near 35 - 60°N the surface water is cooler and precipitation dominates evaporation due to the storms brought across the North Atlantic by the jet stream. The water mass structures in this layer vary across the basin with warmer surface waters east of the Mid-Atlantic Ridge owing to the extended Gulf Current, and cooler surface waters in the west of the Mid-Atlantic Ridge owing to the Greenland and Labrador Currents.

In the high latitudes north of 60°N and west of the Mid-Atlantic Ridge, evaporation exceeds precipitation, however surface salinity is mainly determined by seasonal changes in surface freshwater melt by glaciers and icebergs as well as runoff from bordering continents. In this part of the basin the Sub Polar Gyre intensifies in winter months bringing denser waters to the surface that are replaced by less dense waters below (van Aken, 2007). In the Labrador and Nordic Sea basins, the net effects of warm stratified saline surface water parcels, cyclonic winds, and latent and sensible heat flux at the air-sea interface results at times in an unstable water column (Marshall and Schott, 1999; Pickart and Spall, 2007). This system then undergoes a process known as deep sea convection, where denser surface waters are mixed down and replaced by less dense waters from below (van Aken, 2007). This physical process leads to the formation of the densest water in the North Atlantic basin, the NADW, which makes up part of the global MOC (Tomczak and Godfrey, 2003). Production of the NADW has a large impact on the MOC with increased production leading to an enhancement of the overall water mass transport by the MOC. East of the Mid-Atlantic Ridge, surface salinity values are also impacted at extreme northerly latitudes by seasonal changes in sea ice, which forms in the Norwegian seas each winter. In this process freshwater is frozen in the surface ice and a brine solution is rejected and released below. This increases the salinity above 34.9 psu (Tomczak and Godfrey, 2003), creating a higher density surface layer that sinks to the ocean floor following the bottom bathymetry of the North Atlantic to form the NADW occupying depths between 1000 and 4000m

(Figure 1.1; Tomczak and Godfrey, 2003), which returns equatorward as part of the MOC (Figure 1.3).

2. North Atlantic variability

In this chapter of the thesis, spatial and temporal scales of North Atlantic atmospheric and oceanic variability are discussed. The most important time scales of variability over the North Atlantic are decadal with a period of approximately 10 years (e.g. Deser and Blackmon, 1993), and multidecadal, with a period of 50 - 80 years (e.g. Delworth and Mann, 2000). Key climate variability indices involving the North Atlantic are presented, followed by an overview of proposed mechanisms that may be driving the observed climate patterns. The chapter concludes with a discussion of the impacts and importance of North Atlantic variability both regionally and globally.

2.1 North Atlantic atmospheric variability

The most dominant and persistent mode of atmospheric variability over the North Atlantic basin is the NAO (Hurrell et al., 2003). The NAO is usually defined as normalized, time-averaged index of sea level pressure differences between its two centers of action, the Azores and Iceland (Rogers, 1984; Hurrell, 1995a). Although the centers of action for this definition may not always account for the largest explanation of variance, the major advantage of this definition is the consistent historical observation records at each center of action, dating back to 1864 (Marshall et al., 2001b).

The NAO is the key pattern responsible for the atmospheric redistribution of heat surplus from the subtropical Atlantic to the Arctic. By the definition above, a positive (negative) phase of the NAO implies a stronger (weaker) than average pressure gradient between these two centers of action, resulting in an increase (decrease) of poleward heat transport by stronger (weaker) than average westerlies across the Atlantic basin. Due to the enhanced pressure gradient during positive phases of the NAO (NAO +) stronger winter storms develop that cross the Atlantic

with average storms tracking northeast across the basin towards northern Europe (left panel Figure 2.1), while negative phases of the NAO (NAO -) are associated with fewer and weaker winter storms taking on a more zonal track towards south central Europe (right panel Figure 2.1; Wanner et al, 2001).

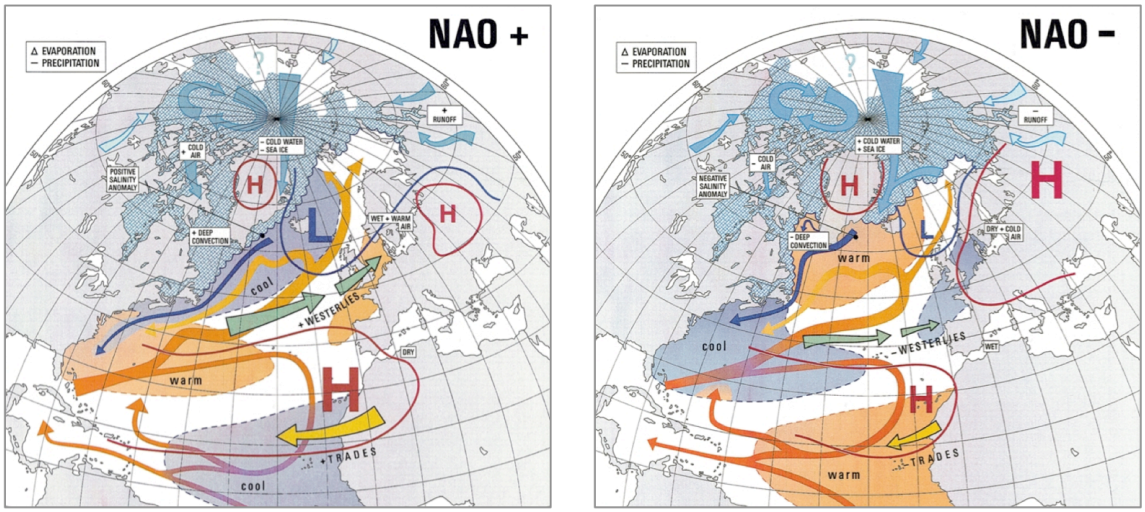

Figure 2.1 Graphical representation of positive (left) and negative (right) NAO phases. Filled dashed contours represent warm (orange) and cool (blue) SST patterns. Sea-ice extent is represented by the hatched blue regions. Directional arrows show the flow systems in ocean, atmosphere and rivers. SLP systems are represented as High (H, red) and Low (L, blue) with relative contour locations, and white rectangles describe characteristic climate conditions or important processes. From Wanner et al., 2001.

While present in all seasons, the strongest NAO patterns appear in winter months when the north-south temperature gradient is at its peak, resulting in an amplification of the SLP gradient between these two centers of action. The NAO has also been linked with the leading atmospheric mode over the Northern Hemisphere (NH), the Northern Hemisphere Annular Mode (NAM, also referred to as the Arctic Oscillation, AO), defined as the leading Empirical Orthogonal Function (EOF) of monthly mean SLP in the NH. As seen in Figure 2.2, the spatial patterns of the AO and the NAO are remarkably similar, leading some scientists to view the NAO as a regional expression of the AO (Marshall et al., 2001a). The leading EOF mode of the

NAO explains approximately 37% of the 500 hPa geopotential height variability over the basin (right panel of Figure 2.2) during the December, January, February (DJF) months (Wallace and Gutzler, 1981; Esbensen, 1984; Barnston and Livezey, 1987; Kushnir and Wallace, 1989; Wallace, 1996, Cayan 1992).

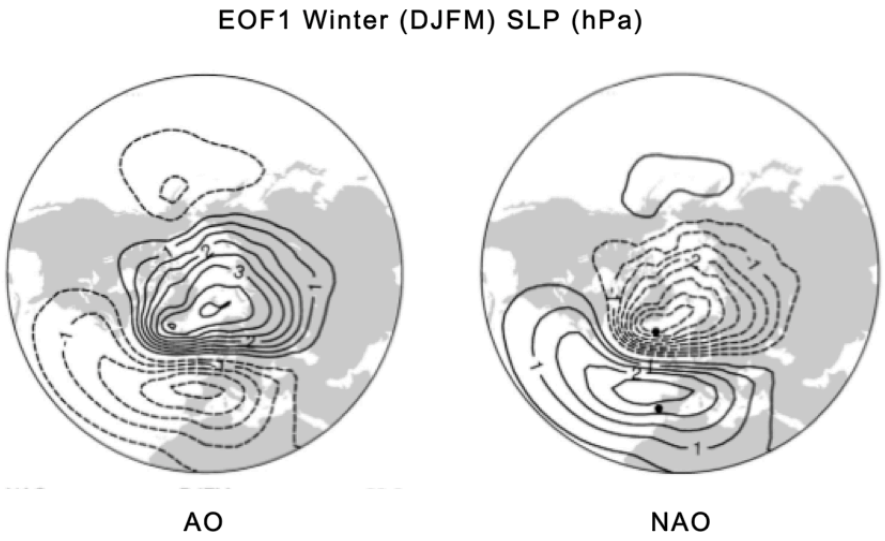

Figure 2.2 First EOF of winter (DJFM) mean SLP anomalies (1899-2006) for (left) the AO (20-90N) and (right) the NAO (20-70N, 90W-40E). Contour interval of 0.5 hPa with dots in right panel representing locations of centers of action (Lisbon, Portugal and Stykkisholmur, Iceland). From Hurrell and Deser, 2009.

There are a wide variety of temporal scales expressed by the NAO as can be seen in the monthly standardized NAO Index from 1950-2010 and its spectra shown in Figure 2.3. The bottom panel shows the slightly white power spectra at short periods (< 3 months), increasing to a seasonal peak, followed by redder power spectra as the period increases beyond a year for this monthly index. In this analysis a slight maximum appears in the spectra with a period near 7 - 8 years, and a smaller maximum appears with a period near 2 years. This feature can also be seen in the 13-month averaged NAO (black bars, top panel of Figure 2.3) with the NAO switching between positive and negative phases at an approximately decadal time scale.

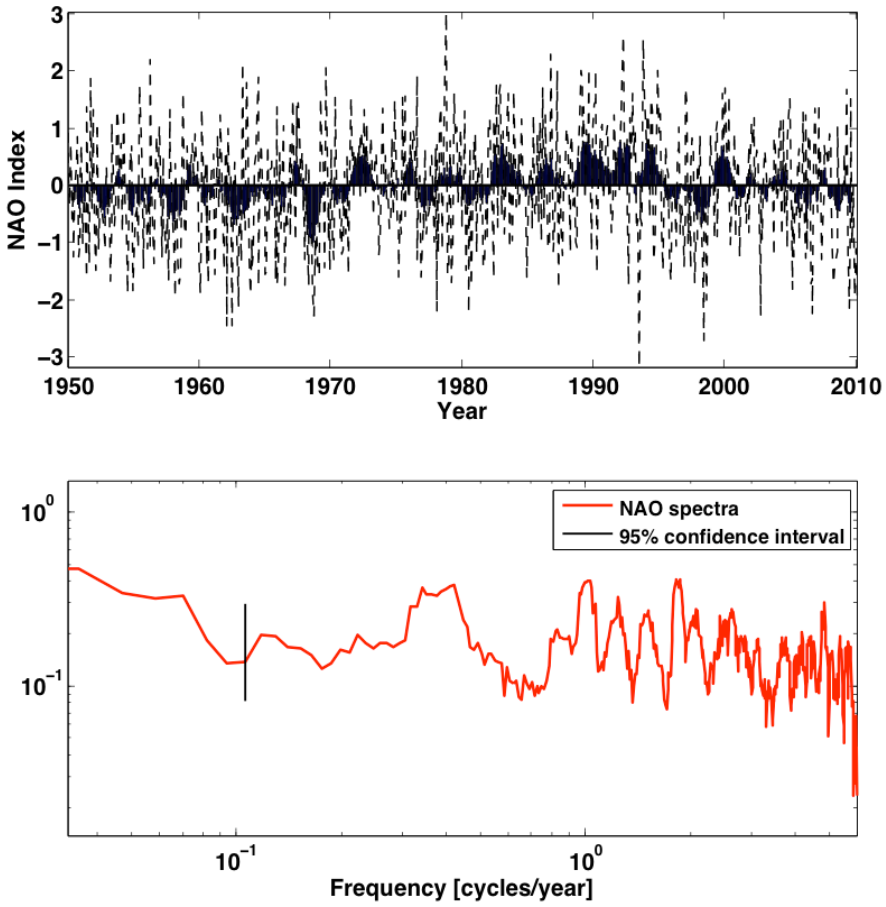

Figure 2.3 (Top) Standardized EOF based NAO Index 1950-2010 , monthly index (black dashed line), 13 month mean (black bars). (Bottom) Power spectra for monthly NAO Index (red). Based on data obtained from NOAA Climate Prediction Center (2010).

2.2 North Atlantic oceanic variability

When examining atmospheric and oceanic temporal and spatial variability patterns over the North Atlantic, some similarities appear. For example, regression analysis of sea surface temperatures (SST) on the wintertime NAO Index provide an indication of a key link between atmospheric and oceanic variability, with a tripole pattern emerging over the North Atlantic Ocean (Figure 2.4a), coinciding with the SST for a NAO+ phase (Figure 2.1, left). These SST patterns are likely the direct feedback of air-sea turbulent heat flux anomalies with energy being released to the atmosphere over the positive SST anomaly subtropical region and energy being

absorbed by the ocean over the negative SST anomaly subpolar region. These latent and sensible heat anomalies are associated with NAO wind forcing patterns as seen in Figure 2.4b and 2.4c. Ocean currents like the Gulf Stream, and ocean circulations including the Subtropical and Subpolar gyres also play a role in the SST anomaly patterns (McCartney and Talley, 1984; Kerr, 1997; Sutton and Allen, 1997).

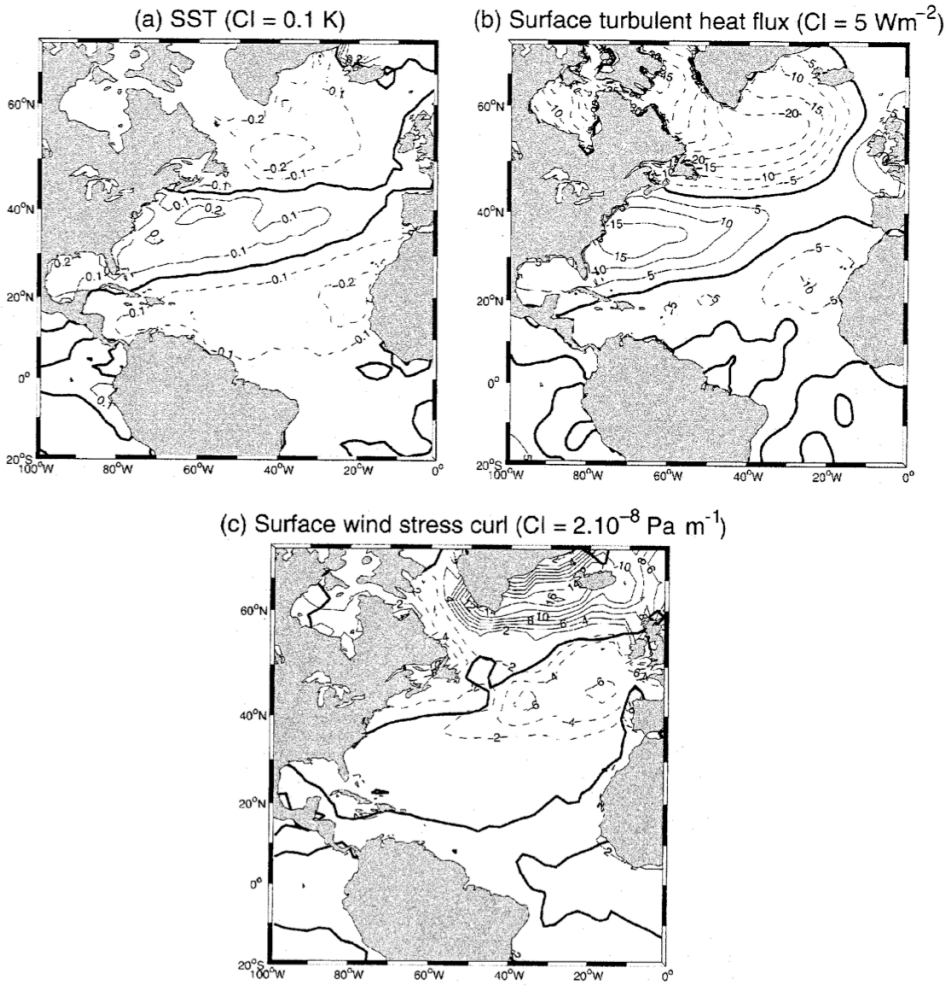

Figure 2.4 Regression maps for North Atlantic anomalies of (a) SST (CI = 0.1 K, negative values dashed), (b) surface latent and sensible heat flux (CI = 5 Wm^{-2} , dashed out of the ocean), (c) surface wind stress curl (CI = 2 x 10^{-3} Pa m^{-1} , dashed for anticyclonic) onto the NAO index. From Marshall et al. (2001b).

These processes occurring at the air-sea interface allow the atmosphere to modify the surface wind stress and heat fluxes, resulting in the modification of ocean surface layer temperatures, however this process does not take place instantaneously, SST anomalies lag atmospheric anomalies by approximately 1 month (Marshall et al., 2001a). This lag time results in the peak SST tripole pattern emerging in the late winter months following a NAO+. Watanabe and Kimoto (2000) found that this tripole persisted for approximately one year, which is four times longer than would be expected by local air-sea dampening processes (decay scale of ~3 months, Frankignoul et al., 1998). The spectra of this tripole pattern, (see Figure 3b in Marshall et al., 2001b) is red, suggesting that upper mixed layer ocean processes may enhance the persistence of atmospheric modes of variability (Hasselman, 1976; Alexander and Deser, 1995). Czaja and Marshall (2001) examined SST variability trends based on SST differences on either side of the Gulf Stream and found a re-emergence of opposite sign in the SST differences with a 6 year delay, suggesting that heat advection by anomalous ocean currents and atmospheric feedback as possible causes. According to Marshall et al. (2001a), wintertime SST anomalies from the subpolar gyre appear to propagate eastwards on a decade time scale. In addition, ocean gyre intensity was studied by Curry and McCartney (2001) and was found to have interannual to interdecadal links to the NAO.

Another climate variability pattern found in North Atlantic is referred to as the Atlantic Multidecadal Oscillation (AMO). The AMO is defined as the detrended area averaged time series of SST north of the equator (Enfield et al., 2001). As seen in Figure 2.5, the decadal running mean of the AMO reveals an oscillating signal of mean North Atlantic SST anomalies with a period near 65-75 years, and a maximum amplitude near +/- 0.4°C over the instrumental record (IPCC, 2007). Schlesinger and Ramankutty (1994) identified a similar multidecadal pattern (65-70 years) in North Atlantic surface temperature oscillation through singular spectrum analysis of temperature records dating back to the 1850s. Similar multidecadal climate

trends have also been found in paleoclimate reconstructions over the North Atlantic dating back to 1650 A.D. with periods of approximately 60-110 years (Delworth and Mann, 2000; Gray et al., 2004). In addition, climate models agree with observations suggesting that the thermohaline circulation may be the primary source of the multidecadal oscillating SST anomaly signal (Delworth and Mann, 2000; Latif, 2001; Sutton and Hodson, 2003; Knight et al., 2005).

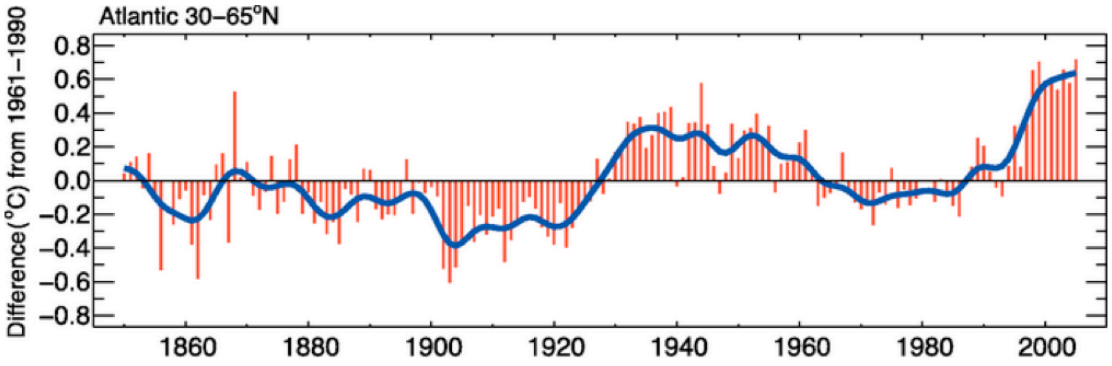

Figure 2.5 AMO Index from 1850 to 2005, represented by annual anomalies of SST in the North Atlantic (30-65°N) relative to 1961-1990 mean SST (°C). Smooth blue line shows decadal variations. From IPCC, 2007.

To further examine the North Atlantic Ocean temperature variability we can examine the vertical water column trends. Polyakov et al. (2009) present an EOF analysis of the two leading modes of zonal average water temperature variability in the North Atlantic basin (Figure 2.6). The first EOF associated with the nonlinear trend provides an explanation of 28.1% of the variance, while the second EOF associated with multidecadal variability explains 20.2% of the variance. The inset of Figure 2.6a displays the associated time series for EOF-1 which demonstrates a positive trend that has a correlation of R=0.95 with anthropogenic radiative forcing (red line of Figure 2.6a inset). The associated time series for EOF-2 however correlates favorably with the AMO Index (R=0.59). These significantly separated

vertical ocean temperature variability patterns suggest two distinctly different temporal variability scales.

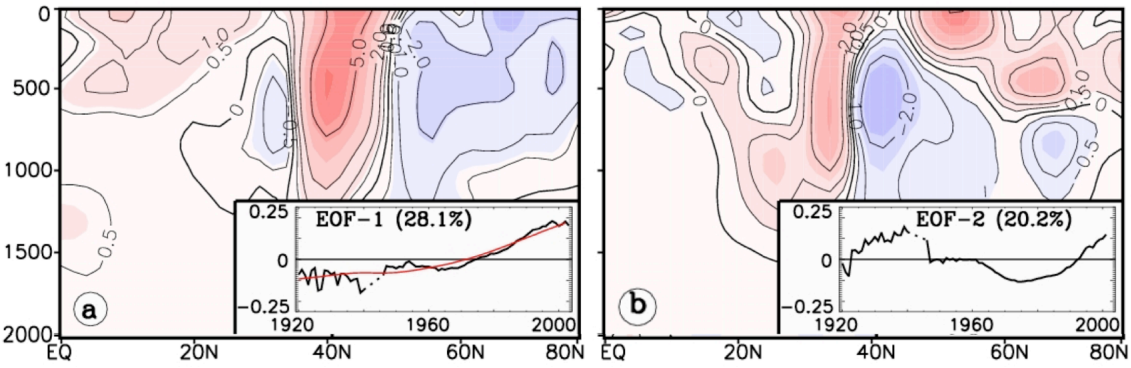

Figure 2.6 Patterns of zonal average North Atlantic Ocean temperature variability associated with (a) EOF-1, nonlinear trend; insert shows PC1, (C, black) and radiative forcing, (red) for comparison (b) EOF-2, multidecadal variability; insert shows PC2, C for comparison. From Polyakov et al., 2009.

The deep ocean variability is largely linked to variability in the MOC, and as a result it imposes longer time scales of variability. For example, ocean convection processes contribute to North Atlantic variability with the dominant convection processes ongoing in the Labrador Sea (Dickson et al., 1996; Lab Sea Group, 1998). One such example of a deep ocean variability event is the Great Salinity Anomaly (GSA), which occurred 1968 to 1971 (Levitus, 1989). During the event deep convection processes in the Labrador Sea were interrupted by a large, fresh surface layer, which can be seen in Figure 2.7 where the isohalines become tightly packed and the salinity gradient between the surface and middle ocean layers inhibits convection processes. Studies have shown the GSA may have been caused by the combined effects of atmospheric forcing and a great manifestation of quasi-decadal fluctuations (Kushnir, 1994; Reverdin et al., 1997; Belkin et al., 1998). McCartney (1997) found a link between end of winter mixed water properties and propagating SST anomalies, suggesting that the LSW underwent warming and cooling phases consistent with NAO phases. Dickson et al. (2002) also found decadal timescale

hydrographic trends in Arctic and subarctic seas that could imprint onto the deep layers of the Labrador Sea in turn impacting the MOC. It is clear that climate patterns of variability exist throughout all layers of the ocean as well as in the atmosphere.

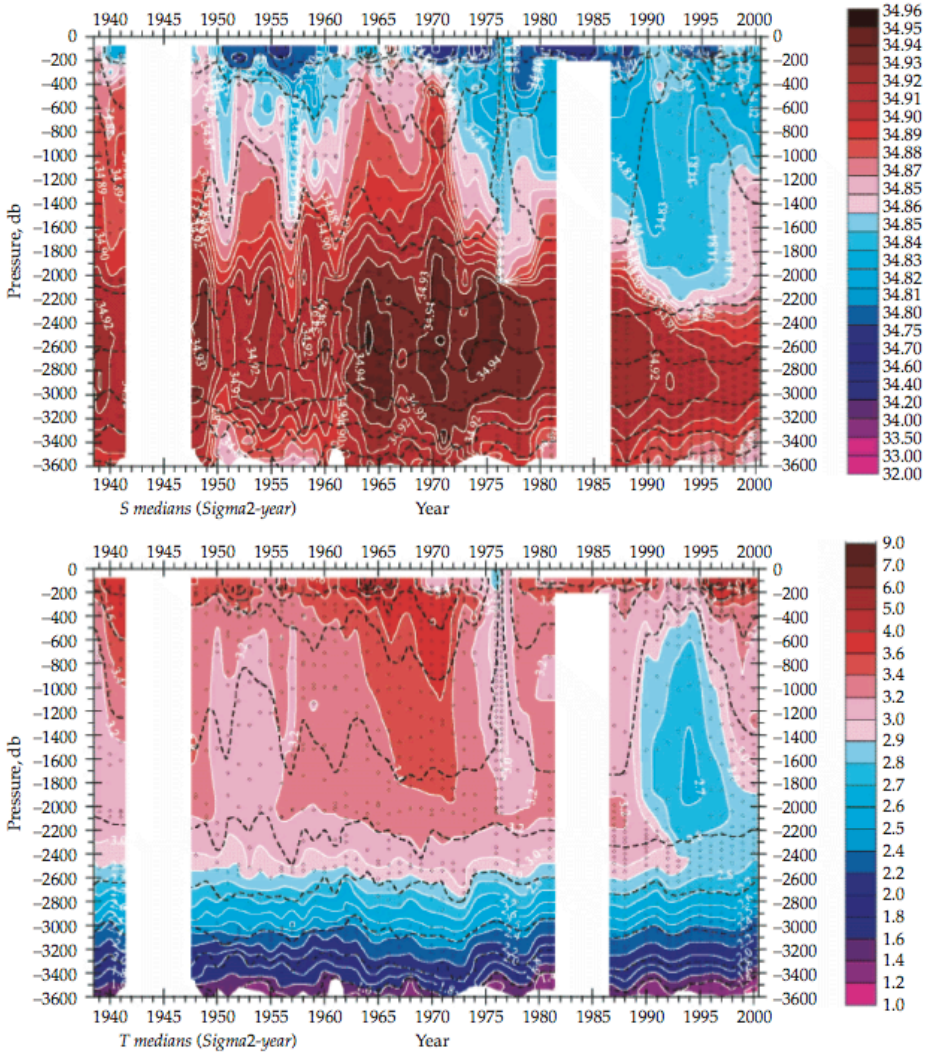

Figure 2.7 Median changes in central Labrador Sea potential temperature (top panel) and salinity (bottom panel, 1938-2000). Provided by Igor Yashayaev.

2.3 Mechanisms governing North Atlantic atmospheric variability

Upon examining the normalized monthly NAO index in Figure 2.3 the signal appears relatively white at high frequencies, and there is no clearly favored cycle over which the NAO behavior is easily predicted. This idea logically makes sense as we reflect on the physical processes governing this North Atlantic system. SLP patterns vary considerable when looking at short timescales. The behavior of the pattern is governed by synoptic scale mean eddy flow interaction and the complex internal dynamics of the atmosphere. Observational evidence however points to two primary temporal variability scales of interest concerning the NAO when looking towards longer time periods. Studies concerning low frequency SST variability and its association with the atmosphere revealed a decadal variability of about 10 - 15 years (Deser and Blackmon, 1993; Kushnir, 1994) possibly provoked by air-sea interactions, and multi-decadal variability of about 40 - 80 years (Delworth and Mann, 2000) possibly linked to MOC circulations.

Several leading hypothesis have emerged as mechanisms driving atmospheric variability. Interaction between the atmosphere's troposphere and stratosphere may provide the key to one of the foremost atmospheric mechanisms governing atmospheric variability. Perlwitz and Graf (1995) and Kodera et al. (1999) both found a strong connection between North Atlantic tropospheric circulation and the stratospheric polar vortex. It is hypothesized that variations of upper troposphere winds caused by periods of NAO+ or NAO- may condition a waveguide, such as the westerlies. This conditioning may enhance the propagation of planetary waves in the upper troposphere, where this waveguide could provide a medium by which upper level stratospheric winds could be mixed down to the surface (Perlwitz and Graff, 1995; Baldwin and Dunkerton, 1999). Thus the tropospheric NAO feature could be provoked by an enhanced stratospheric polar vortex (Marshall et al., 2001b). Several ideas have been presented for means by which the polar vortex could be enhanced, including global warming, ozone

depletion, and tropical volcanic eruptions (Perlwitz and Graff, 1995; Thompson and Wallace, 1998).

Another large-scale climate pattern is persistent on the opposite side of the globe in the Pacific Ocean basin and is known as the El Nino/Southern Oscillation (ENSO). By definition, ENSO "describes the basin-wide changes in air-sea interaction in the equatorial Pacific region" (Glantz, 1996). Unlike the NAO, scientists are fairly confident in the mechanisms driving this climate pattern, with SST patterns across the equatorial Pacific forcing the atmospheric boundary layer, in turn impacting the ocean's response to changing surface wind stresses, resulting in the oscillating ENSO coupled ocean-atmosphere system (Marshall and Plumb, 2008). The time period between warm El Nino events varies between 2 and 8 years (Trenberth, 1997). Since this is a large scale coupled air-sea climate pattern, the impacts of ENSO may stretch beyond the limits of the Pacific basin, and some scientists suggest it may be impacting the NAO through modulation of the Hadley cell, which may act as a connecting "bridge", or teleconnection between the Pacific and Atlantic basins (Marshall et al., 2001b). Several observational studies have found the Pacific ENSO may impact Atlantic wind fields and SST on interannual time scales (Hameed et al., 1993; Nobre and Shukla, 1996) with a time lag of 4 - 5 months (Enfield and Mayer, 1997) possibly caused by weaker trade winds reducing surface latent heat flux in the tropical Atlantic (Klein et al, 1999).

2.4 Mechanisms governing North Atlantic oceanic variability

The atmospheric mechanisms alone cannot explain the reddening of the NAO spectra associated with decadal variability, nor the decadal and multidecadal variability patterns observed in the ocean. However, atmospheric forcing affects oceanic variability patterns. For example, observations show that the effects of atmospheric forcing leave behind patterns in SST, surface heat flux, and surface wind stress (Figure 2.4). Observations have also shown that the ocean may integrate high-frequency atmospheric forcing which may re-emerge each winter in

the mixed ocean layer impacting the overlying atmosphere (Alexander and Deser, 1995). Finally, due to the much greater heat capacity of ocean water compared with air, the water mass may acquire a "memory" of winter conditions through subduction into the thermocline (Stommel, 1979; Marshall and Molteni, 1993) or through seasonal sequestering of winter conditions from below the seasonal thermocline (Qiu and Huang, 1995).

One of the proposed oceanic mechanisms involves processes at the air-sea interface in mid-latitudes. Barsugli and Battisti (1998) offer a simple model in which the ocean mixed layer is in thermal equilibrium with atmospheric forcing. As the system is in equilibrium, heat exchange is reduced, resulting in the thermal damping of the NAO or other atmospheric forcing. Barsugli and Battisti (1998) suggest that thermal coupling with the ocean mixed layer provides a mechanism by which the persistence of atmospheric modes such as the NAO are enhanced. Czaja and Frankignoul (1999) support this oceanic influence with observations, as they found evidence that a significant fraction (~25%) of winter NAO variance could be predicted from the prior basin scale SST pattern.

A modeling study was performed by Rodwell et al. (1999) in which the Hadley Center model was forced with an SST tripole forcing similar to the pattern depicted in Figure 2.4a. They set the lower boundary conditions with the tripole SST pattern, and found that the ensemble of model runs displayed the low frequency components of both modeled and observed NAOs tracking one another over a 50 year period. Interpretation of these results suggests that by understanding ocean variability, low frequency NAO variability may also be better understood.

Variations in the ocean gyres may provide another mechanism for reddening of the SST spectrum by changing the heat transport (and SST patterns) over the basin, indirectly impacting the atmosphere as well. Bjerknes (1964) was one of the first to investigate air-sea interactions over the North Atlantic. Following the groundwork laid by Bjerknes (1964), Marshall et al. (2001b) summarized a system of atmosphere and ocean interactions over the North Atlantic for oscillating NAO

phases (Figure 2.8). They first consider a North Atlantic climate where a positive NAO has persisted for a period of time (Figure 2.8, left). In this scenario, the enhanced wind stress would drive an anti-cyclonic gyre anomaly (intergyre gyre, IGG, circle with anti-cyclonic directional arrows in top left panel of Figure 2.8) at the confluence of the subpolar and subtropical gyres. Marshall et al. (2001b) suggests that this IGG would interact with the mean North Atlantic current trajectory (diagonal line across basin in top panels of Figure 2.8), resulting in enhanced poleward heat transport. Over a decadal timescale, net northward heat flux (curly arrows in bottom left panel of Figure 2.8) may increase the SST over the northern portion of the basin, and through air-sea interactions this anomalously warm surface ocean could imprint on the atmosphere resulting in anomalously warm air temperatures, decreasing the temperature North-South gradient across the basin and through thermal wind processes result in a weakened atmospheric jet stream (Marshall et al., 2001b). As a result of these processes the SLP gradient would decrease between the Azores and Iceland (i.e. - NAO anomaly), and the net heat transport across the basin would take on a more zonal flow, driving a weaker cyclonic IGG (circle with cyclonic directional arrows in top right Figure 2.8). This climate setup is representative of a negative NAO state, while over time zonal heat transport would result in anomalously higher SST in the southern part of the basin and lower SST in the northern part of the basin, increasing the temperature gradient communicated to the atmosphere and allowing an oscillation back to a positive NAO state of the climate system. The time delay between the coupling of the ocean gyres with the atmospheric jet stream in this oscillatory system has a decadal scale and may be linked to the time required for the first baroclinic mode of oceanic Rossby wave to cross the mid-Atlantic basin (Latif and Barnett, 1994; Jin, 1997, Weng and Neelin, 1998, Cessi, 2000, Goodman and Marshall, 1999, Neelin and Weng, 1999; Marshall et al., 2001). While some coupled ocean models have attempted to model this system, observations have yet to confirm or deny the coupled system mechanism described by Marshall et al. (2001b).

Vertical transport through thermohaline circulations (curly arrows, Figure 2.8) may also modify ocean heat transport, as SST anomalies coinciding with NAO phases induce anomalies in the MOC, providing another mechanism to explain patterns of the North Atlantic variability (Marshall et al., 2001b). Timmerman et al., (1998) suggests processes modulating heat transport by the MOC, which indirectly impact the atmosphere through air-sea interactions with SST anomalies, may regulate decadal variability over the North Atlantic. There is also some debate regarding the mechanism behind multidecadal variability with some arguing that it is ocean driven (Delworth et al., 1993) and others arguing that it is a combined coupled air-sea mechanism (Selten et al., 1999; Hakkinen, 2000). While large-scale observations have yet to test mechanisms of multidecadal oceanic variability, experimental evidence from coupled GCM runs by Delworth and Mann (2000) supports the theory that MOC circulation does indeed play a role in SST variability on multidecadal time scale of ~70 years. On decadal timescales, convective processes in the Labrador Sea and other Arctic and subarctic seas have also been

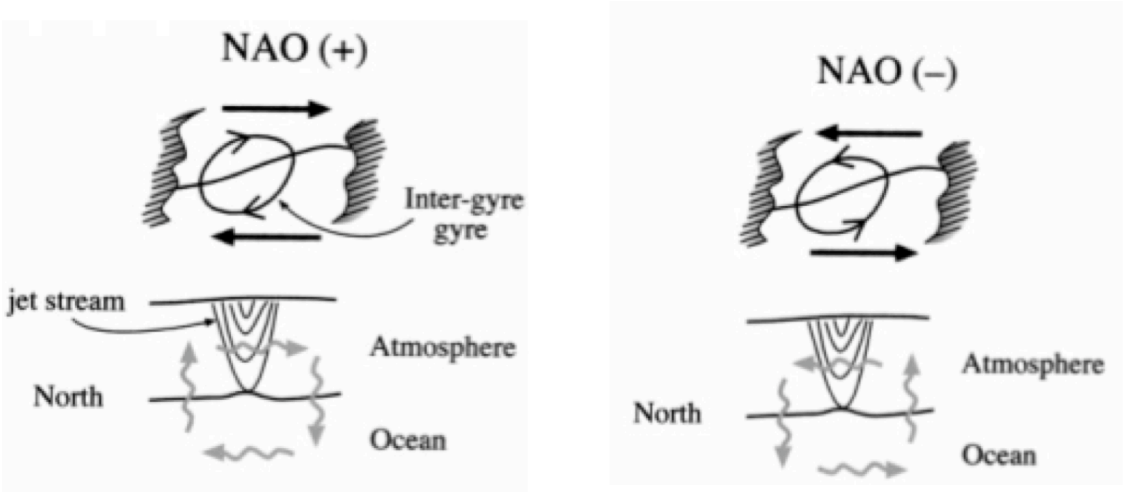

Figure 2.8 Diagram displaying theoretical feedback of NAO phases on the ocean (top + NAO, bottom - NAO). Solid arrows represent surface winds and curly arrows represent anomalous air-sea heat flux or MOC heat transport. From Marshall et al. 2001.

linked with North Atlantic variability (Dickson et al., 2002). Spall (1996) found that the southward propagation of LSW may impact the stability of the western boundary current off the east coast of the USA, indirectly impacting the circulation by the Gulf Stream current as well as air-sea interactions.

2.5 Global and local impacts of North Atlantic variability

It is of great importance to understand the mechanisms driving decadal and multidecadal patterns of variability in the North Atlantic because the impacts of the variability are vast both locally and globally. The NAO influences local and global surface temperature trends, storm tracks and precipitation, ocean circulations, ecology, and even local economies (Hurrell et al., 2003, Figure 2.10), while the AMO has been linked with surface air temperature and precipitation patterns, as well as Atlantic hurricane trends impacting the United States (Enfield et al., 2001; Goldenberg et al., 2001).

Changes in the phase of the NAO result in different local temperature trends across continents surrounding the North Atlantic basin, as depicted in Figure 2.1 (left). These trends are important not only for their local impacts but also for the long-term global impacts. For instance variability of more and 1°C in the winter-averaged (December, January, February; DJF) surface temperatures are linked with one standard deviation change in the NAO index (Figure 2.9). The spatial pattern of these DJF surface temperatures shows highest variability over the European and North American continents (Figure 2.9). This may be significant, as recent (1980-2000) winter temperatures have been 1-2°C warmer than average over the Eurasian continent as well as much of North America (Hurrell et al., 2003). With much of the global temperature increases in recent decades occurring over northern continents in winter and spring seasons (Folland et al., 2001) periods of NAO+ or NAO- may have global climate change impacts.

Storm tracks and precipitation trends across the North Atlantic are modified by both the NAO and AMO phases. The general spatial patterns of precipitation

associated with NAO phases are depicted in Figure 2.1, with the largest impacts occurring in Europe. These patterns have significant impacts on the economies of European and Scandinavian nations, including agricultural harvests, hydroelectric energy generation (see Figure 2.10 for an example of these impacts for Norway), as well as other industries dependent upon winter snowfall (Beniston, 1997; Marshall et al., 2001a). Storm tracks over the North Atlantic also impact wave heights, with NAO+ associated with decreased wave heights south of 40°N and increased wave heights over the northeast Atlantic (Bacon and Carter, 1993; Kushnir et al., 1997). These wave height variations impact shipping practices, off-shore natural resource exploration, coastal development, as well as local ecology (Marshall et al., 2001a).

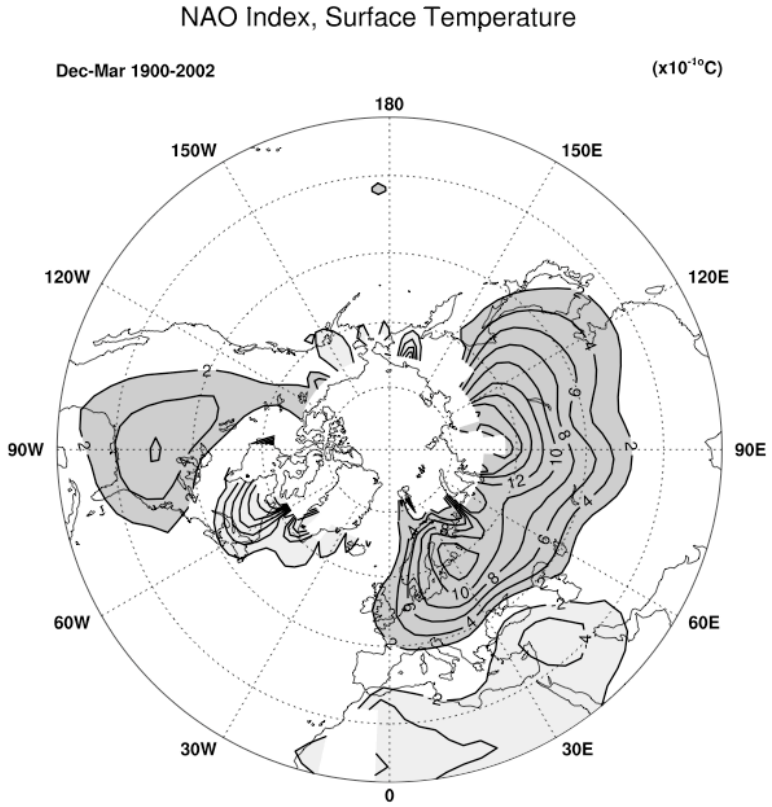

Figure 2.9 Changes in mean winter (December-March) land surface and sea surface temperatures (x 10^{-1} °C) corresponding to a unit deviation of the NAO index over 1900-2002. The contour increment is 0.2°C. Temperature changes >0.2°C are indicated by dark shading, and those <-0.2°C are indicated by light shading. Regions of insufficient data (e.g., over much of the Arctic) are not contoured, and the zero contour has been excluded. From Hurrell et al., 2003.

The warm phase of the AMO coincides with less than average rainfall over most of the United States (US), examples of such events include the droughts of the 1930's and 1950's (Enfield et al., 2001). Precipitation variations coinciding with warm and cold phases of the AMO are largest in summer months, resulting in large deviations from the normal outflow of water basins between phases with the outflow of the Mississippi varying by 10% and of Lake Okeechobee in Florida varying by as much as 40%. In addition to modifying the precipitation patterns, the warm phase of the AMO has been linked with the frequency of Atlantic hurricanes (Gray, 1990; Goldenberg et al., 2001), with large implications for coastal communities along the Gulf of Mexico and the eastern seaboard of the US.

In the North Atlantic the MOC defines the largest portion of oceanic heat transport, and intensity variations can have large-scale and widespread impacts. Under current greenhouse warming scenarios depicted in GCMs it has been suggested that the atmosphere may move to a state where a NAO+ phase is preferred (Marshall et al., 2001a). If the NAO+ phase were preferred, it can be inferred that there would be anomalous warming of the northern ocean mixed layer, which would decrease the density of the surface ocean waters and as GCM projections suggest, weaken the intensity of the MOC in the North Atlantic (Rahmstorf, 1999; Rahmstorf and Ganopolski, 1999; Delworth and Dixon, 2000). If this scenario were to play out, northern Europe and the northeastern North America would experience rapid cooling owing to the lack of poleward heat transport (Marshall et al., 2001a). Paleoclimate records show evidence that a similar rapid cooling event abruptly took place over the North Atlantic during and following the last Ice Age (Broecker and Denton, 1989; Marotzke, 2000). Both current coupled GCMs and paleoclimate records show that such a climate event may occur on a timescale as short as a few decades (Marshall et al., 2001a). While the current observational records are relatively short and the mechanisms driving North Atlantic variability are still open to interpretation and discussion, the implications of a weakened MOC should be taken seriously. Based on the widespread impacts of

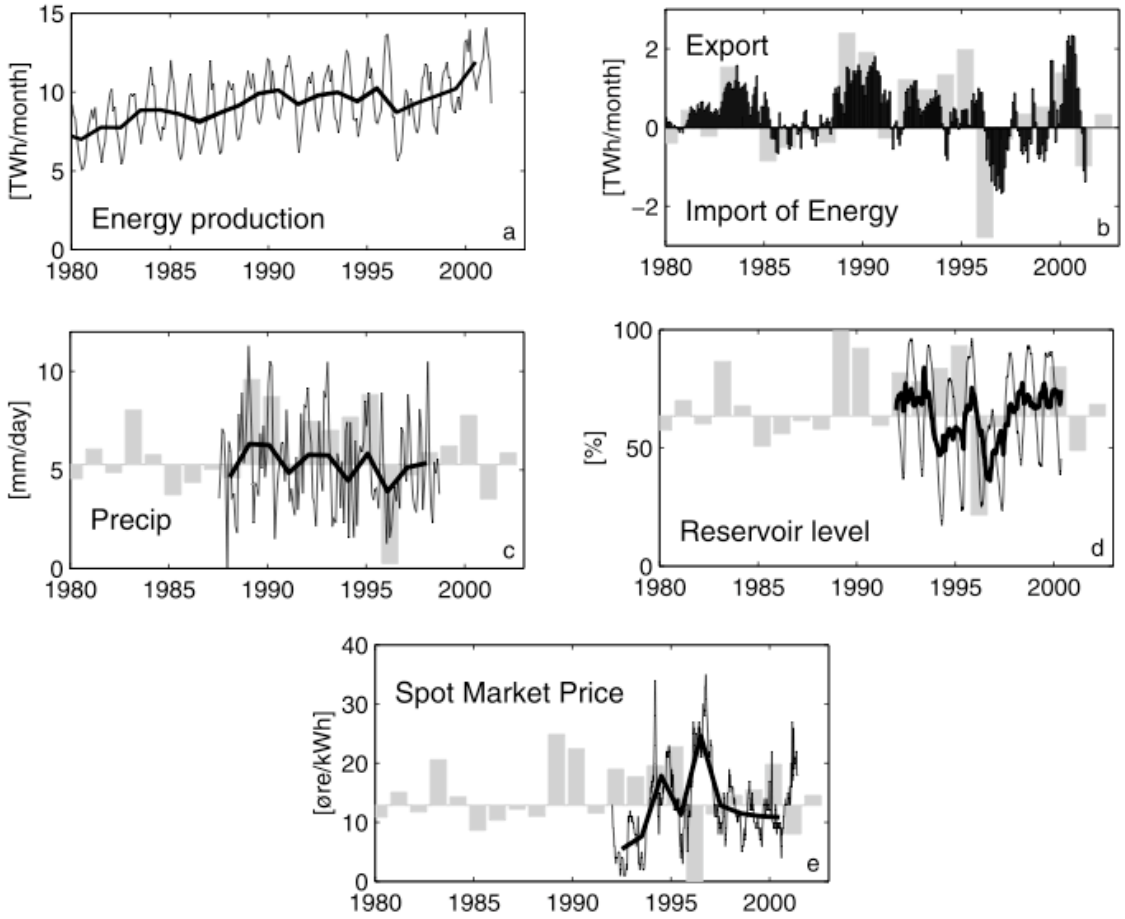

Figure 2.10 Comparison of winter NAO index (light gray bars, positive referring to +NAO phase) with local impacts in Norway. Monthly values are represented by a thin black line, and annual values by a thick black line. (a) Hydroelectric energy production in TWh, (b) Difference between energy production and consumption (Twh), positive values implying surplus energy to be exported, (c) EOF of average of rainfall over Scandinavia (mm/day), (d) Norwegian hydroelectric dam reservoir levels (%), (e) Electric energy market price. From Hurrell et al., 2003.

variability over the North Atlantic, attempts to better understand mechanisms driving variability over the basin should continue, with focus on changes occurring in the atmosphere, air-sea interface, as well as the interior ocean.

3. Model description

In this chapter of the thesis, an overview of the experimental box model and methods used to complete model experiments are discussed. The governing equations of the model first are summarized, followed by an explanation of the external stochastic system forcings. Methods of numerical solutions to the governing equations are presented, and the chapter concludes with a discussion of the design of model experiments completed with the box model.

3.1 Governing equations

In the analysis we used a model proposed by Marshall et al. (2001b). The model simulates changes in the intensity of North Atlantic Ocean gyres and upper ocean temperature anomalies in response to air-sea interactions. These interactions include the damping of upper ocean temperatures by latent and sensible heat fluxes at the air-sea interface, as well as heat transport by Ekman pumping in the upper ocean layers. Together these equations form the foundation of a simple box model used to describe the interactions and feedbacks between the model forcing components.

Following Marshall et al. (2001b), the North Atlantic Ocean is approximated by a box with an east-west dimension, L_x, of 3000 km, a north-south dimension, L_y, of 3000 km, and a depth, h, of 200m. The model divides the North Atlantic basin into north and south triangular ocean and atmosphere boxes (Figure 3.1). The triangles were split along a line that approximately coincides with the mean climatological zero wind stress line as is depicted in Figure 3.1. Marshall et al. (2001b) argued that the climatological anomalies in water temperature would be approximately equal and of opposite sign for the northern and southern boxes, and for simplification, the equations describing the model were set up for the northern triangular box ocean temperature anomalies.

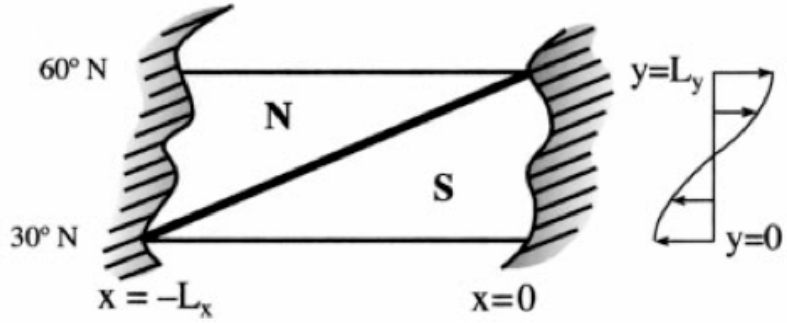

Figure 3.1 Diagram of box model. N and S show the northern and southern triangles of North Atlantic domain, divided by the thick black diagonal line, which coincides with the mean climatological zero wind stress line. The eastern boundary is set at x = 0, with the width of the basin set at L_x. The north-south scale is L_y, and extends from 30°N to 60°N. From Marshall et al. (2001).

The model equations describing this system are Eqs. 3.1–3.4. Equation 3.1 describes the anomaly in upper ocean mixed layer temperature, T, in the northern triangle of the box model resulting from changes in the MOC, intensity of the horizontal ocean gyre, and external stochastic forcing. The MOC streamfunction anomalies, Ψ_m, (i.e. anomalies in the vertical cell of the circulation) are defined by Eq. (3.3). The ocean gyre streamfunction anomalies, Ψ_g, (i.e. anomalies in the horizontal cell of the circulation) are defined in Eq. (3.2) with the wind stress term, τ, defined in Eq. (3.4). The stochastic forcing of the atmosphere, F_T, is defined in Eq. 3.1, while the stochastic wind forcing, F_τ, is included in Eq. 3.4. Note that following Marshall et al. (2001b), these equations are written in dimensionless form. The scaling factors used to transfer dimensional variables to non-dimensional are presented in Table 3.1.

$$\frac{\partial T}{\partial t} = m\Psi_m + g\Psi_{g|w} - \lambda T + F_T \qquad (3.1)$$

$$-\frac{\partial \Psi_g}{\partial t} + \frac{\partial \Psi_g}{\partial x} = -\tau \qquad (3.2)$$

$$\frac{\partial \Psi_m}{\partial t} = -sT \tag{3.3}$$

$$\tau = F_\tau - fT \tag{3.4}$$

In addition to the forcings described above following Marshall et al. (2001b) we include an addition term to explore the system response to Labrador Sea deep-sea convection processes. This Labrador forcing term may be added to Eq. (3.1) to result in:

$$\frac{\partial T}{\partial t} = m\Psi_m + g\Psi_{g|w} - \lambda T + F_T + \alpha T_{Lab}\ , \tag{3.5}$$

where α is a non-dimensional Labrador factor, and T_{Lab} is the Labrador Sea potential temperature, both will be defined clearly in Section 3.2.

The non-dimensional factors *g* and *m* describe the efficiency of heat transport by the horizontal gyre and MOC, while λ describes the effectiveness of damping of ocean temperature anomalies by air-sea interactions and feedback of Ekman layers. The solenoidal factor, *s*, refers to the efficiency of the thermal ocean dipoles driving the meridional overturning in the basin. The meridional overturning is similar to electric current being passed through the metal coils of a solenoid. The factor *f* describes the feedback of ocean temperatures on wind stress, and other non-dimensional terms used in the model (including definitions for the above factors) are explained in Table 3.2, while the model variables used to define the model parameters are defined in Table 3.3.

Table 3.1 Definitions of Marshall box model scaling factors

Scaling Factor	Description	Value
Y	Temperature anomaly scale	1° C
Ψ_M	MOC scale	15 Sv (=10^6 m^3 s^{-1})
Ψ_G	Gyre scale	10 Sv (=10^6 m^3 s^{-1})
t_{delay}	Time scale (time for Rossby wave to cross domain)	4 years
$Q_M = \rho_o c_o \overline{\Delta T}^z \Psi_M$	MOC heat transport scale	6.4297 x 10^{14} kg m^2 s^{-3}
$Q_G = \rho_o c_o \overline{\Delta T}^{zerocurl} \Psi_G$	Gyre circulation heat transport scale	3.2148 x 10^{14} kg m^2 s^{-3}
$Q_E = \rho_o \overline{\Delta T}^y L_x \frac{\tau_{wind}}{f_o}$	Ekman heat transport scale	6.2790 x 10^{13} kg m^2 s^{-3}
τ_{wind}	Surface wind stress scale	0.05 N m^{-2}
L_x	East-west domain dimension	3 x 10^6 m
L_y	North-south domain dimension	3 x 10^6 m
L_z	Vertical dimension of MOC	1000 m
h	Depth of mixed ocean layer	200 m
$A = 0.5 L_x L_y$	Area of triangular ocean basin	4.5 x 10^{12} m^2
λ_o	Ocean Ekman damping coefficient	20 W m^{-2} C^{-1}
$S = \frac{2 g^* \alpha L_z^2 L_x}{\Psi_M L_y}$	Solenoidal scale factor driving meridional overturning	1.5855 x 10^{-9} s^{-1} C^{-1}

Table 3.2 Values of non-dimensional factors used in Marshall Model equations

Non-Dimensional Factor	Description	Value
$m = \frac{Q_M}{AY}\frac{t_{delay}}{C_o}$	Factor describing efficiency of heat transport by MOC	16.8192
$g = \frac{Q_G}{AY}\frac{t_{delay}}{C_o}$	Factor describing efficiency of heat transport by ocean gyres	8.4096
$\lambda = d - fe$	Factor describing intensity of damping of ocean temperature anomalies by air-sea interactions and wind effects	1.0403
$s = S \cdot Y \cdot t_{delay}$	Solenoidal factor driving meridional overturning	0.2
$d = \lambda_o \frac{t_{delay}}{C_o}$	Damping coefficient for ocean temperature anomalies	2.3543
$e = \frac{H_{ek}}{Y}\frac{t_{delay}}{C_o}$	Positive factor describing feedback of wind effects on ocean temperature anomalies	1.6425
f	Factor for feedback of ocean temperature anomalies on wind stress	0.8

Table 3.3 Constants used in Marshall Model equations

Constant	Description	Value
ρ_o	Density of water	1280 kg m^{-3}
c_o	Specific heat of water	4186 J kg^{-1} C^{-1}
f_o	Coriolis parameter	10^{-4} s^{-1}
$\overline{\Delta T}^{z}$	Change in mean SST at 'Z' latitudes	8 °C
$\overline{\Delta T}^{zerocurl}$	Change in mean SST along mean zero wind curl line	6 °C
$\overline{\Delta T}^{y}$	Change in mean SST at latitudes corresponding to horizontal 'Z' lines	10 °C
$C_o = \rho_o c_o h$	Specific heat capacity of ocean basin	1.0716 x 10^{9} J m^{-2} C^{-1}
$g^* = \frac{0.2\Psi_M L_y}{2\alpha L_z^2 Y t_{delay}}$	Effective gravity referring to varying densities in water	7.9274 x 10^{-5}
α	Thermal expansion coefficient of water	0.00015 C^{-1}
$H_{ek} = \frac{Q_E}{A} = 2 \cdot \frac{c_o \overline{\Delta T}^{y}}{L_y} \frac{\tau_{wind}}{f_o}$	Pseudo air-sea heat flux by Ekman heat transport	13.9533 kg s^{-3}

An initial temperature perturbation, T_o, was not defined in the proposed box model by Marshall et al. (2001b). For the purpose of this study however we proceeded with a value of T_o=2°C, a value twice that of the model temperature anomaly scale, Y=1°C that was provided by Marshall et al. (2001b). While observations of SST anomalies over the North Atlantic basin indicate that a more likely sea surface temperature anomaly across the diagonal of the basin would be approximately 0.5°C (Czaja and Frankignoul, 2002; Hurrell et al, 2003), for the purpose of this simple modeling study it will serve the purpose of displaying the response of the system components and feedbacks. In addition, the choice of the initial ocean temperature anomaly value is not very important as we are using a linear model with a long integration. Initial MOC (Ψ_{mo}) and gyre (Ψ_{go}) streamfunctions were initialized with values of $\Psi_{mo} = \Psi_{go} = 0$ Sv.

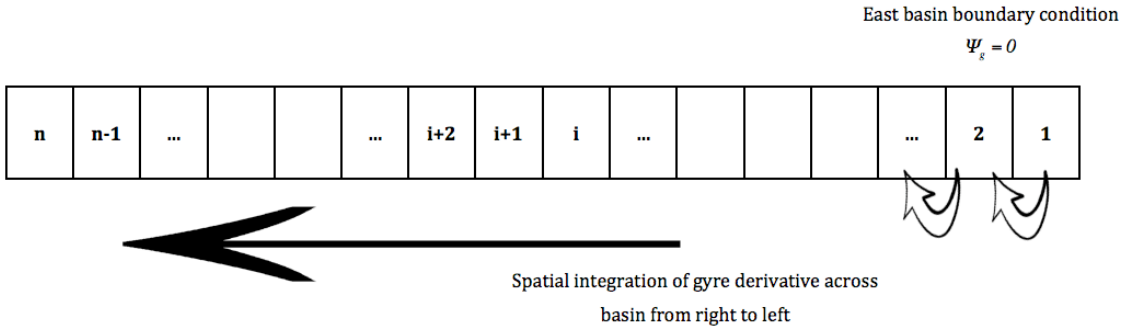

Figure 3.2 Diagram describing integration of spatial gyre derivative across the North Atlantic basin. The boundary condition for the gyre term is set equal to 0 at the eastern boundary of the basin and the spatial derivative is integrated from right to left across the basin with the first integration from location 1 to 2, the second integration from 2 to 3, etc. until arriving at the western boundary where the gyre value provides the initialization of the gyre streamfunction for the next time step.

In addition to the time derivatives included in the model governing equations there also exists a spatial derivative for the gyre streamfunction, as seen in the second term of Eq. (3.2). Thus, for solution, this equation required a boundary

condition. Following Marshall et al. (2001b), we defined $\Psi_g = 0$ at the eastern boundary and used it in the numerical simulations at each subsequent time integration step as depicted in the diagram in Figure 3.2.

3.2 External stochastic forcings

3.2.1 Original observational time series

The region of interest for this study comprises the North Atlantic between 30-70°N and 80-0°W. While this region is not inclusive of the entire North Atlantic domain, it closely matches the model region proposed by Marshall et al. (2001b, Figure 3.1). The SW-NE oriented diagonal of this region coincides with the theoretical model, and all of the forcing mechanisms are present in this basin with the exception of Labrador Sea processes. We extended the northern limits of the domain 10 degrees further north than the proposed domain of Marshall et al. (2001b; 30-60°N) in order to capture deep-sea convection processes in the Labrador Sea.

Several observational datasets were utilized while developing the external stochastic time series required to force the model. The observational SST time series, HadSST2, was obtained from the Climate Research Institute at the University of East Anglia (http://www.cru.uea.ac.uk/cru/data/temperature/). HadSST2 is a 5° x 5° gridded dataset from 1850 to present time of monthly SST anomalies relative to the 1961-1990 mean (see Rayner et al., 2006 for details). Initial processing divided this grid into an average monthly northern and southern triangle following the theoretical model of Marshall et al. (2001b). We proceeded using the northern triangle time series for the analysis as the theoretical model determined the values of the northern and southern triangles should be approximately of equal and opposite sign. The standard deviation of this observed timeseries was calculated to be $\sigma_{SST_N} = 0.58$°C. Next the monthly timeseries was prepared for the post-processing to be discussed later in this chapter, by linearly detrended, seasonally

filtered (by subtracting monthly mean values), and normalized by monthly standard devations.

The SAT observational data was obtained from the International Comprehensive Ocean-Atmosphere (ICOADS; http://www.esrl.noaa.gov/psd/data/gridded/data.coads.2deg.html). The ICOADS SAT time series includes the most extensive collection of surface marine data in a 2° x 2° gridded monthly dataset from 1800 to the present. After averaging the gridded dataset to form a basin average SAT timeseries the standard deviation of the observations was calculated to be $\sigma_{SAT} = 2.20$ °C. Then the monthly SAT time series was also prepared for post-processing. It was first linearly detrended, then de-trended by subtracting monthly means, and finally normalized by monthly standard deviations.

Wind observations were obtained from the NCEP/NCAR (National Centers for Environmental Prediction/National Center for Atmospheric Research) Reanalysis 2.5° x 2.5° gridded daily dataset from 1948 to the present (http://www.esrl.noaa.gov/psd/data/gridded/data.ncep.reanalysis.surface.html, Kalnay et al., 2006). These time series included zonal u and meridional v components of wind vector values at a 10-meter height above sea level. During the initial processing of these datasets, gridded values for both u and v component wind stress (τ) were estimated using Eq. (3.6 -3.8).

$$\tau = \rho_{air} C_D U_{10} |U_{10}| \qquad (3.6)$$

where, ρ_{air} (~1 kg/m^3) is the density of air, U_{10} is the magnitude of the u or v wind vector, and C_D is the drag coefficient, estimated by Yelland and Taylor (1996):

$$C_D = \frac{0.6 + 0.07U_{10}}{1000}, \qquad \text{for } 6 \le U_{10} \le 26 \qquad (3.7)$$

$$C_D = \frac{0.29 + \frac{3.1}{U_{10}} + \frac{7.7}{U_{10}^2}}{1000}, \qquad \text{for } 3 \le U_{10} < 6. \tag{3.8}$$

Wind stress values were then used to estimate Ekman pumping (w_e) over the basin following Frankignoul et al. (1997):

$$w_e = \frac{1}{\rho_{ocean} f_o}\left(\frac{\partial \tau_y}{\partial x} - \frac{\partial \tau_x}{\partial y}\right), \tag{3.9}$$

where, ρ_{ocean} (~10 kg/m^3) is the density of ocean water, f_o is the Coriolis parameter, and the partial derivatives represent the E-W change in τ_y and the N-S change in τ_x. The estimates of Ekman pumping (w_e) were temporally averaged at all domain grid points and the resulting pattern is displayed in the top panel of Figure 3.3, while the bottom panel displays average w_e values over each longitude of the basin. In addition to this climatological analysis, standard deviations of w_e were calculated for each averaged longitudinal belt of the domain to be used later in post-processing. Based on the theory of Ekman pumping, positive (negative) values represent cyclonic (anti-cyclonic) wind stress exerted on the surface resulting in a confluence (diffluence) of surface waters resulting in upwelling (downwelling) processes (Marshall and Plumb, 2008). From Figure 3.3 we can see the wind-driven upwelling processes dominating in Labrador and Nordic Seas of the northern triangle of the theoretical model proposed in Marshall et al. (2001b). This is what we would expect to see as we discussed deep sea convection processes in the sub-arctic seas in earlier chapters of this thesis. We also see downwelling processes dominating in the southern triangle of the basin with a maximum in the SW corner of the basin. A time series of daily and monthly mean w_e values was also generated, and similar to the other datasets linearly detrended, de-seasoned, and normalized. An overview of the daily w_e time series and some of its statistical properties can be found in Figure B.1 of Appendix B.

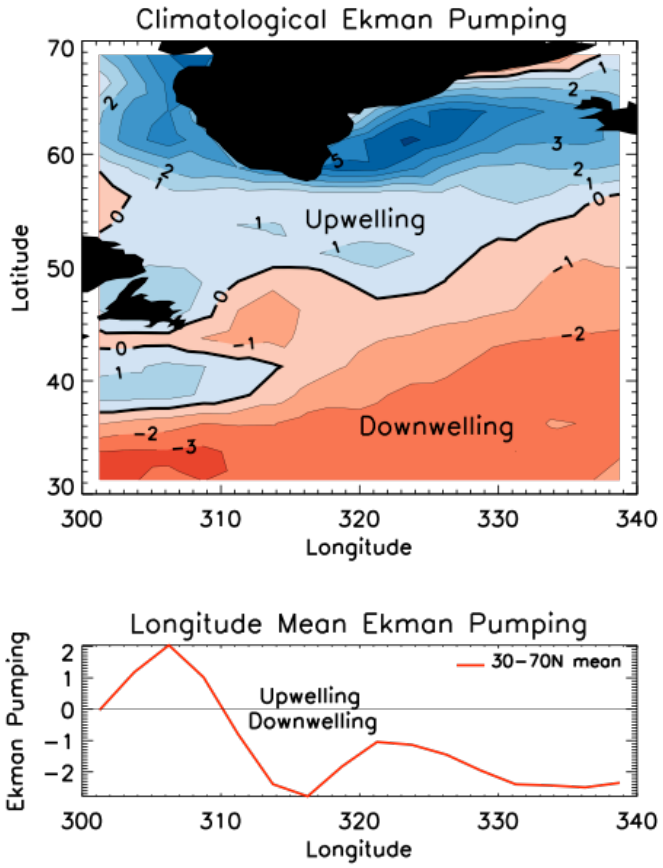

Figure 3.3 Climatological Ekman pumping (1948-2008). (Top) climatological Ekman pumping (10^{-6} m/s) over the North Atlantic Ocean derived from the NCEP Reanalysis winds at 10 m height. Regions of ocean upwelling are depicted in blue, and regions of downwelling in red. (Bottom) mean climatological Ekman pumping averaged over each longitude belt of the basin from 30°N to 70°N (10^{-6} m/s).

The final observational dataset used in this study was Labrador Sea potential temperature, obtained from Igor Yashayaev (personal communication). This annual timeseries provided Labrador Sea potential temperatures at depths ranging from approximately 50 to 3,500 meters for a period 1938 through 2001. While this time series may appear somewhat crude compared with the spatial and temporal coverage provided by other datasets, it is the best data available to work with at the present time. With the purpose of this dataset being to capture deep sea convection

activity in the Labrador Sea, we focused on an annual mean potential temperature averaged over 50 - 500 meters depth range, having a standard deviation of $\sigma_{Tlab} = 0.25$°C. This annual timeseries was detrended and normalized, and then a cubic spline was fit to the timeseries to fill the gaps (1975, 1979-1980, 1982-1983, 1985-1986, and 1989). The non-dimensional Labrador scale term (α) was estimated by correlating an annual-averaged northern triangle SST time series corresponding to the annual 50-500m Labrador potential temperature time series. In doing the maximum correlation of $R = 0.34$ was found at a time lag 0 years. The non-dimensional Labrador scaling term was then estimated as:

$$\alpha = R_{N_{SST}|T_{Lab}} \cdot \frac{\sigma_{N_{SST}}}{\sigma_{T_{Lab}}} = 0.337 \cdot \frac{0.58}{0.25} = 0.78. \qquad (3.10)$$

which was incorporated into Eq. 3.1 with the addition of the damping term.

3.2.2 Stochastic forcing development

Once the initial processing was completed for the observational time series, we continued with the development of external stochastic model forcings. The goal of this process was to generate a synthetic set of stochastic time series that captured the statistical properties of actual observations. We proceeded by incorporating a analysis technique referred to as Hurst exponent estimation, derived from the mathematical fields of fractals and chaos theory (Feder, 1988). This self-similar method was initially developed by Hurst (1951) to describe the flow and water storage in the Nile River watershed (Feder, 1988). Since then, applications of the Hurst exponent calculations have expanded to several research fields including analyzing the predictability of financial stock market and bond trends (Carbone et al., 2004; Qian and Rasheed, 2007), traffic flow and congestion patterns (Lan et al., 2003), as well as determining persistence of climate parameters such as precipitation, temperatures, and SLP (Rangarajan and Sant, 2003; Rehman and El-Gebeily, 2009).

The Hurst Exponent (H) is useful for each of these applications because it provides a quantification of long-term correlations within a time series across many time scales. A full derivation of the Hurst exponent may be found is included in Feder, (1988). Values for H range between 0 and 1 and may be classified into one of the following three patterns:

(1) $H = 0.5$, indicates a completely random series

(2) $0.0 < H < 0.5$, indicates an anti-persistent pattern

(3) $0.5 < H < 1.0$, indicates a persistent pattern.

In the case (1) the series is entirely random and thus lacks predictability. An example of such a timeseries can be found in the top panel of Figure 3.4, which displays a random time series of this Hurst exponent value. Anti-persistent patterns are found for case (2) with the magnitude of anti-persistence increasing as H approaches zero. In this situation an increasing tendency from timestep 1 to 2 would likely be followed by a decreasing tendency in the series from timestep 2 to 3 (Feder, 1988). The opposite is true for case (3), which indicated a persistent pattern, in which case an increasing trend in the series from timestep 1 to 2 would likely be followed by an increasing trend in the series from timestep 2 to 3. An example of increasing persistence can be found in the Figure 3.4 (middle, H=0.7; bottom, H=0.9).

H estimations provide a measure for long-term memory of a timeseries, which may be applied to this study in the generation of stochastic time series with statistical properties derived from observations. We calculated the H for each observational timeseries discussed earlier in this section, resulting in a value of H=0.88 for the monthly SAT timeseries and a value of H=0.87 for the annual Labrador timeseries. The Ekman pumping timeseries was handled slightly differently owing to the spatial gyre derivative contained in Eq. (3.1). For this case we wanted to determine the uniformity of H values over various latitudinal belts before proceeding with a set w_e H value for the monthly timeseries, the results may

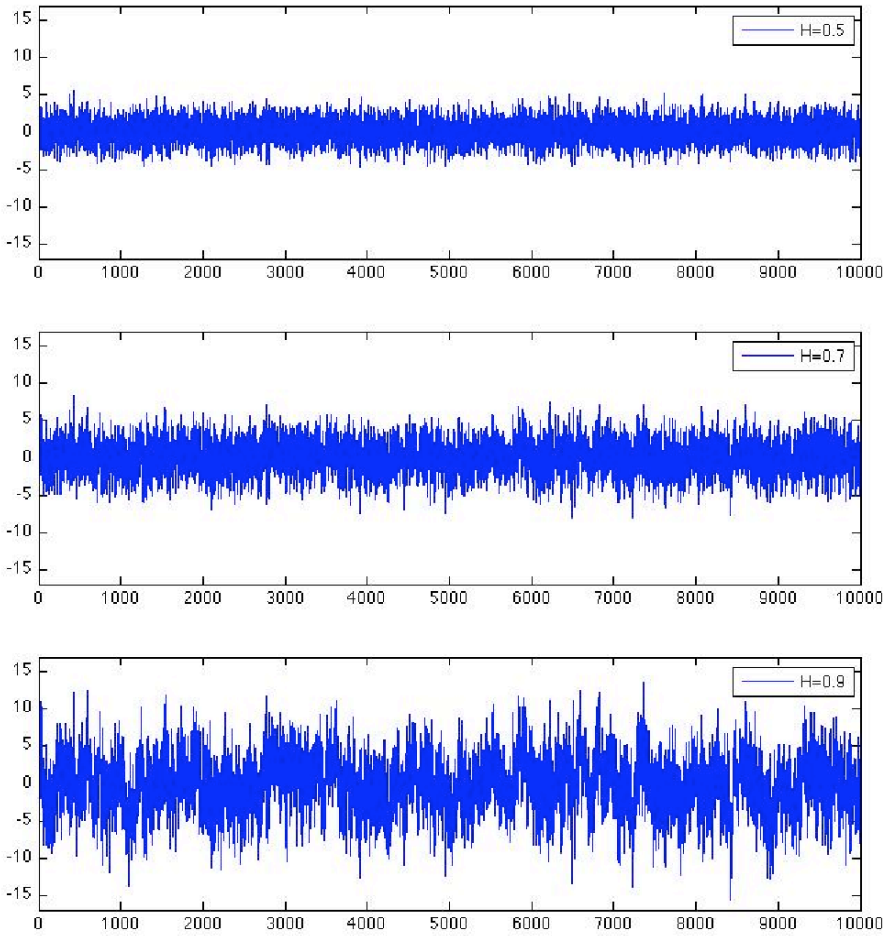

Figure 3.4 Examples of random time series with varying Hurst exponents (top, H=0.5; middle, H=0.7; bottom, H=0.9)

be seen in Table 3.4. It is clear that the H estimates across belted regions of the basin are very similar in nature, varying in magnitude of only 0.03.

Daily H estimates for Ekman pumping timeseries appeared higher overall than the monthly timeseries, but this may be expected as synoptic weather systems impacting surface wind stress tend to persist for several days at a time possibly increasing the H estimate value. For completeness we also calculated the H value for the annual average Ekman pumping timeseries, resulting a value of H=0.60. We proceeded from this point by utilizing the value of H=0.60 for the Ekman pumping series as it represented the minimum determined persistence (R/S) calculated over

a range of 1 to 30 years, and would allow us to be confident that a higher daily estimated H of the series wouldn't not be enhancing any model results.

Table 3.4 Hurst exponents estimated over various longitudinal belts (first column) of the domain for daily and monthly average Ekman pumping (We) values.

	Timeseries	
Longitude Belt	Daily We	Monthly We
60-70 N	0.67	0.63
50-60 N	0.67	0.6
40-50 N	0.68	0.58
30-40 N	0.67	0.6
30-70 N	0.68	0.6

After determining the H value for each timeseries, a program was utilized to generate a synthetic random daily timeseries, 500 years in length, with H for the SAT, Labrador, and w_e forcing parameters. Stochastic Hurst forcing timeseries were developed for the SAT and Labrador timeseries following:

$$SAT(l) = \sigma_{SAT} \cdot Synth_{SAT}(l) = F_T \tag{3.11}$$

$$LAB(l) = \sigma_{LAB} \cdot Synth_{LAB}(l) = T_{LAB} \tag{3.12}$$

where l represents time, and *Synth* represents the synthetic timeseries with H values determined above. Here F_T in Eq. (3.11) represents the stochastic atmospheric temperature forcing, and T_{LAB} in Eq. (3.12) represents the stochastic Labrador Sea potential temperature forcing for the model, and both will be incorporated into the main model Eq. (3.5).

Synthetic wind forcing has a spatial derivative and as a result in the model it is incorporated as follows:

$$W_e(x) = \sigma_{w_e(x)} \cdot Synth_{w_e}(l) = F_\tau, \tag{3.13}$$

where x represents the spatial location across the grid, and the standard deviation values coincide with the values at each longitudinal belt as were discussed earlier in this section. Here F_τ in Eq. (3.13) represents the stochastic wind forcing for the model, and will be incorporated into the main model Eq. (3.4).

Model experiments are executed with both the synthetic forcing as well as a random white noise forcing for comparison. Synthetic external forcing for the white noise experiments is generated following the same derivations in Equations (3.11 - 3.13) with the exception that the synthetic Hurst timeseries are replaced by a random seed timeseries.

3.3 Numerical solutions of the governing equations

Numerical methods are utilized to solve otherwise complicated and difficult (or even impossible to solve) differential equations. The original differential equations 3.1-3.3 describing changes in ocean temperature and circulation are approximated by finite differences as follows.

Applying the Taylor Series expansion to a function $T(t)$ and expressing time step as Δt results in:

$$T(t+\Delta t) = T(t) + \frac{\partial T(t)}{\partial t} + \frac{\partial^2 T(t)}{\partial t^2}\frac{\Delta t}{2} + O(\Delta t^3) + \ldots, \qquad (3.5)$$

where, $O(\Delta t^3) + \ldots$ represents higher order terms.

From (3.5), the first derivative $\frac{\partial T}{\partial t}$ may be approximated by the "central derivative", which incorporates the average of the function evaluated at the timestep Δt prior to and after the time of interest, t:

$$\frac{\partial T}{\partial t} = \frac{T(t+\Delta t) - T(t-\Delta t)}{2\Delta t} - O(\Delta t^2). \qquad (3.6)$$

The main advantage of this differencing scheme is 2nd order accuracy, with truncation errors of order Δt^2. These errors are smaller than those produced by 1st order accuracy methods such as the Euler-Forward and Backward finite-differencing schemes, resulting in truncation errors of order Δt (Chapra and Canale, 2006). As an example, if the timestep were to be set at half of its initial value, the 1st order forward scheme would produce a truncation error half of its initial value, while the centered difference scheme would produce a truncation error one quarter of its initial value.

Disadvantages for this scheme include (1) more computational time than 1st order methods due to evaluation of the function at $(t + \Delta t)$ and $(t - \Delta t)$ for each timestep evaluation, and (2) potential model instability as computational modes are generated over time (Pielke, 2002). Disadvantage (1), addressing additional computational time, may be estimated by selecting the largest timestep possible while meeting the Courant-Friedrich-Lewy (CFL) stability criterion following:

$$\nu = \left| \frac{U_{max} \Delta t}{\Delta x_{min}} \right| \leq 1, \tag{3.7}$$

where ν is the Courant number, U_{max} is the fastest model velocity, and Δx_{min} is the smallest spatial model dimension (LeVeque, 2002). If the Courant number is greater than 1, then the model may not resolve model processes as the speed of advection may be greater than the grid resolution (LeVeque, 2002). In order to determine the maximum timestep to maintain model convergence and stability, Eq. (3.7) may be solved for Δt:

$$\Delta t = \frac{\Delta x_{min}}{U_{max}}. \tag{3.8}$$

Disadvantage (2) concerning the splitting of the model solution for two numerical modes may be corrected by incorporating the Euler-Forward scheme every Nth timestep.

These two disadvantages were addressed in a series of test experiments. First (1) was addressed by determining the maximum timestep using the CFL condition (3.8) using the maximum model velocity of Rossby wave propagation:

$$U_{max} = \frac{L_x}{4 years} = 750{,}000 m \cdot year^{-1}, \qquad (3.9)$$

and the minimum spatial model dimension of basin depth, $L_z = 1{,}000 m$, resulting in a maximum timestep, $\Delta t = 0.0013 yr$. Next, the computational mode issue was addressed by executing the model over a timeperiod of 500 years, with the incorporation of the Euler-Forward scheme every N time steps (see Appendix A for details).

The horizontal gyre equation (Eq. 3.2 from the original differential equations) requires separate consideration when investigating numerical methods, owing to the addition of a spatial derivative. Due to the high computational time required by central differencing methods, described above as disadvantage (1), we will proceed with a forward in time, backward in space differencing scheme depicted as:

$$\frac{U_j^{n+1} - U_j^n}{\Delta t} + C \frac{U_{j+1}^n - U_j^n}{\Delta x} = 0, \qquad (3.10)$$

where, U represents the horizontal gyre streamfunction (Ψ_g), C is a model constant, n refers to the time index, j refers to the spatial index, and Δt and Δx represent the time and space steps. We can solve equation 3.10 for the next time index to yield:

$$U_j^{n+1} = U_j^n - \frac{C\Delta t}{\Delta x}\left(U_{j+1}^n - U_j^n\right), \qquad (3.11)$$

which is referred to as the upwind scheme as the spatial grid point j+1 is "upwind" of grid point j (Pielke, 2002).

While the forward differencing scheme may appear crude, it is still practical for the modeling schematics. There are limitations of the box model, including the rough estimations utilized in determining the non-dimensional model forcing coefficients, thus the integration method design of the numerical scheme is of less importance. In addition this differencing scheme has the advantage of shorter computational time, as it is only utilized for the relatively short (16 spatial steps) spatial integration across the basin.

3.4 Model experimental design

In Chapter 2, spatial and temporal variability scales over the North Atlantic were presented, with the dominant temporal scales being decadal and multi-decadal. These variability patterns were hypothesized to be forced by various mechanisms including atmospheric forcing, air-sea interactions, the intergyre gyre, meridional overturning circulation, deep-sea convection in the subpolar seas, as well as others. In order to evaluate which mechanisms may be most important for the variability of the North Atlantic system and how the mechanisms interact with one another, a series of experiments was developed utilizing the simple box model and external stochastic forcing fields. The four series of experiments designed include the Wind experiments, the SAT experiments, the Labrador experiments and the General Experiments. An overview of the experiments can be found in Table 3.5. In each series the model was forced by it's own unique external stochastic forcing series based on the experiment name. For instance the Wind experiment was forced by the stochastic wind forcing (based on discussions in Section 3.2). In addition the experiments contained in each series begin with the most basic model (i.e. W1, forced by stochastic wind forcing alone) and incorporate additional mechanism

feedbacks with increasing complexity until the most complex model is reached for each series (i.e. W3, forced by stochastic wind forcing, with MOC and Gyre feedback). In addition to the stochastically forced series experiments, a parallel set of experiments was carried out incorporating a white noise external forcing (based on discussions in Section 3.2) in order to compare the results of the Stochastic forcing with Hurst mechanisms to a random white noise forcing. The model results for each series of experiments are presented in further depth in Chapter 4.

Table 3.5 Summary of box model experiments. First column contains the names for each stochastic and white noise experiment (i.e. W1 and WW1) and the second column contains the forcings and feedbacks allowed for each experiment.

	Wind Experiments
W1/WW1	Wind forcing alone
W2/WW2	Wind forcing with Temperature feedback
W3/WW3	Wind forcing with Temperature and MOC feedback
	SAT Experiments
S1/SS1	SAT forcing alone
S2/SS2	SAT forcing with MOC feedback
S3/SS3	SAT forcing with Gyre feedback
S4/SS4	SAT forcing with MOC and Gyre feedback
	Labrador Experiments
L1/LL1	Labrador forcing alone
L2/LL2	Labrador forcing with MOC feedback
L3/LL3	Labrador forcing with Gyre feedback
L4/LL4	Labrador forcing with MOC and Gyre feedback
	General Experiments
G1/GG1	Wind, SAT, and Labrador forcing, with Temperature, MOC, and Gyre feedback

4. Results of model experiments

In this chapter of the thesis results from each of the experimental box model series described in Section 3.4 are presented and discussed. Each subsection highlights the results for each of four experiments. The description of each experiment includes evaluation of modeling results starting from the most complete model forced with synthetic forcing, and ending with the most complete model

forced by white noise. Impacts of various model terms/forces on results of simulations are also evaluated. Simulated responses of system components are discussed and compared statistically with model forcings. A comparison of results of simulated time series derived from synthetic and white noise forcing model experiments is also presented. The complete set of model results including spectral analysis for simulated time series for each experiment defined in Table 3.5 can be found in Appendices B (Wind experiment), C (SAT experiment), and D (Labrador experiment).

4.1 Results of Wind experiments

This section highlights the results of the experiments forced by synthetic wind forcing (W3) and white noise forcing (WW3), following the experimental design presented in Table 3.5. Model results for experiment W3 are shown in Figure 4.1. There are a few features that stand out when visually examining these results. It is apparent that a high anti-correlation exists between the simulated responses of the MOC and Gyre anomalies. The MOC response appears to lag behind the Gyre response.

A correlation and time lag analysis was performed utilizing the time series displayed in Figure 4.1 in order to provide quantitative estimates of the above findings. The results of this statistical analysis are displayed in the Wind experiment section of Table 4.1. These results for the W3 experiment confirm the high anti-correlation of R=-0.95 between the simulated MOC and Gyre anomaly responses with a time lag of -4 years. This anti-correlation suggests that heat balance in the North Atlantic may be maintained via communication between these two dynamic system components; for example, when the horizontal gyre weakens, resulting in a weaker northward heat transport, intensification of the MOC compensates for a decrease of heat in the northern North Atlantic by strengthening anomalous northward heat transport.

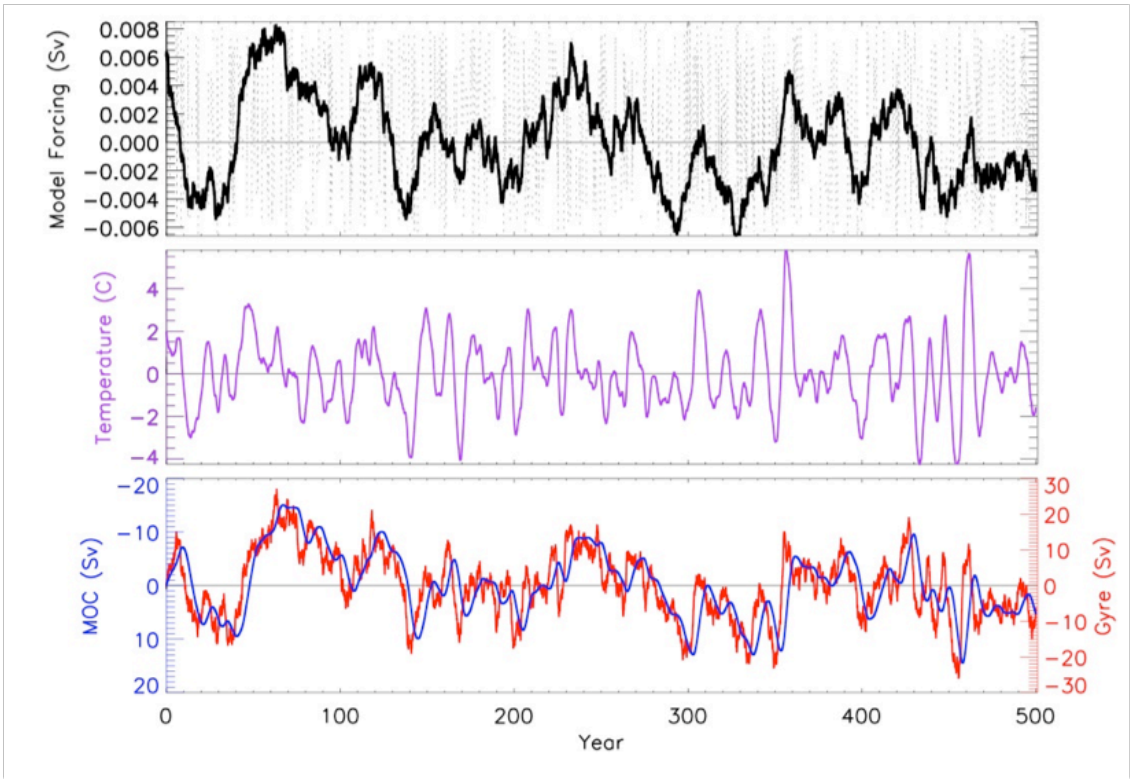

Figure 4.1 Model results for Wind experiment W3. Time series of simulated (middle) ocean temperature anomalies, (bottom) MOC (blue) and horizontal gyre (red) anomalies forced by (top) synthetic wind. Upper panel shows daily (dashed line) and 7 year running mean (solid line) wind forcing (Sv). Note that the MOC anomalies (bottom) are displayed using a reverse vertical scale.

Note that the pattern of variability in the smoothed stochastic wind forcing (top panel, Fig. 4.1) corresponds remarkably well with the resulting variability patterns of MOC and Gyre anomalies (bottom panel, Fig. 4.1). A high anti-correlation of R=-0.92 was found between the wind model forcing and the simulated MOC response with the MOC time series responding to the forcing with an 8-year delay. A high correlation of R=0.83 was found between the wind forcing and simulated Gyre anomaly response with the Gyre time series responding to the synthetic wind forcing with a 6-year delay. This striking correspondence may have significant implications for the understanding of the system response to external forcing. For example, it suggests that the state of the system is defined by the

cumulative effect of external forcing averaged over a limited time. In our case, this time is 7 years and is defined by a damping imposed on the system via the damping coefficient λ in Eq. 3.1. The simulated ocean temperature and gyre anomaly responses have a moderate correlation of R=0.55 at lag=0 years. The correlation with the simulated ocean temperature anomalies have a higher frequency of variability when compared with the simulated gyre anomalies, owing to the dynamics of the system "driving" the ocean temperature variability. This results in a higher correlation with between the Gyre and MOC responses than between the Gyre and temperature responses.

Table 4.1 Correlations and time lags for all model experiments. Maximum correlation values (R) and time lags for Wind (W, WW), SAT (S, SS) Labrador (L, LL), and General (G, GG) Experiments are displayed for model component responses (T, ocean temperature response; M, meridional overturning circulation response; G, horizontal gyre response).

	T/M		T/G		M/G		T/force		M/force		G/force	
	R	lag	R	lag	R	lag	R	lag	R	lag	R	lag
	Wind Experiments											
W1	-	-	0.88	4	-	-	0.52	-3	-	-	-0.20	-9
W2	-	-	0.96	-1	-	-	0.76	-2	-	-	0.69	0
W3	0.42	-4	0.55	0	-0.95	-4	0.44	1	-0.92	-8	0.83	-6
WW3	0.53	-3	0.80	-1	-0.74	-3	0.21	-3	0.32	79	0.20	-3
	SAT Experiments											
S1	-	-	-	-	-	-	-0.66	-4	-	-	-	-
S2	0.54	-3	-	-	-	-	0.42	-10	0.80	-4	-	-
S3	-	-	-0.81	3	-	-	-0.52	3	-	-	0.75	-2
S4	0.54	-3	-0.77	3	0.69	0	-0.37	4	0.75	-6	0.52	0
SS4	0.54	-2	-0.69	3	0.75	0	0.15	-10	0.33	-7	-0.19	-14
	Labrador Experiments											
L1	-	-	-	-	-	-	-0.68	-2	-	-	-	-
L2	0.56	-3	-	-	-	-	0.34	-10	0.80	-4	-	-
L3	-	-	-0.84	3	-	-	-0.48	3	-	-	0.71	-2
L4	0.57	-3	-0.81	3	0.69	0	-0.31	-4	0.75	-6	0.44	0
LL4	0.43	-2	-0.64	3	0.62	0	-0.25	5	0.80	-7	0.41	1
	General Experiments											
G1	0.40	-4	0.53	0	-0.93	-4	-	-	-	-	-	-
GG1	0.50	-3	0.77	-1	-0.76	-3	-	-	-	-	-	-

The results of the synthetically forced Wind experiment (W3) were compared to the results of the white noise forced Wind experiment (WW3). The results for WW3 are displayed in Figure 4.2. This figure used identical scales on the axis to allow visual comparison with Figure 4.1. Expectedly the overall magnitude of the white noise wind forcing as well as magnitudes of the model response to this forcing are much smaller than those of the synthetically forced model (Figs. 4.1 and

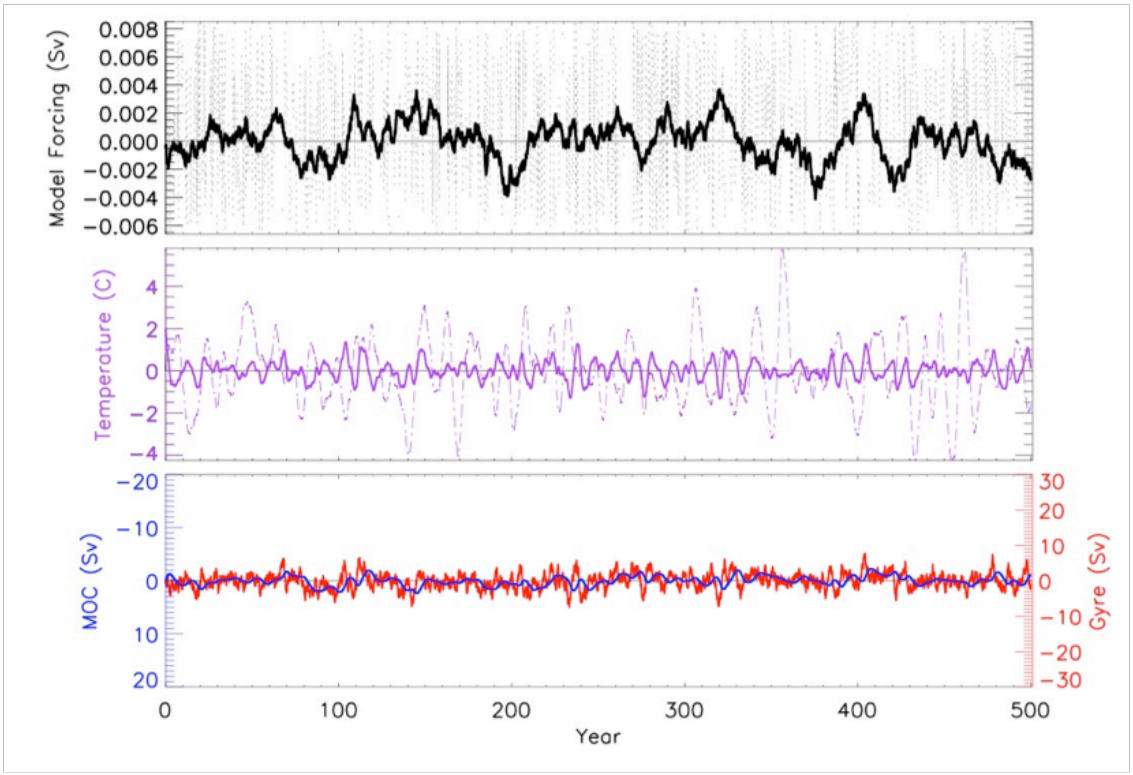

Figure 4.2 Model results for Wind experiment WW3. Figure panels and scales are displayed as in Figure 4.1 with the addition of the W3 simulated ocean temperature anomaly time series (dashed purple line) in the middle panel.

4.2). The white noise forcing time series does not correlate with any of the resulting system components, which is validated by the low correlations between the white noise forcing and model responses in Table 4.1 (First 3 columns). The components of the system, however, are still well linked as attested by high correlations between the simulated MOC and Gyre anomaly responses (R=-0.74 with MOC lagging Gyre

response by 3 years), and between the simulated ocean temperature response and Gyre response (R=0.80 with Gyre response lagging T by 1 year).

A spectral analysis comparing the white noise and synthetic wind forcing as well as the simulated MOC anomalies was completed in order to better understand how the system responds to external forcing. Figure 4.3 displays the results of this analysis. As suggested by theory (Marshall et al., 2001b; Frankignoul et al., 1998), the response of the system is "redder" compared with white noise forcing which is expressed in Figure 4.3 as redistribution of energy from a high-frequency band to a

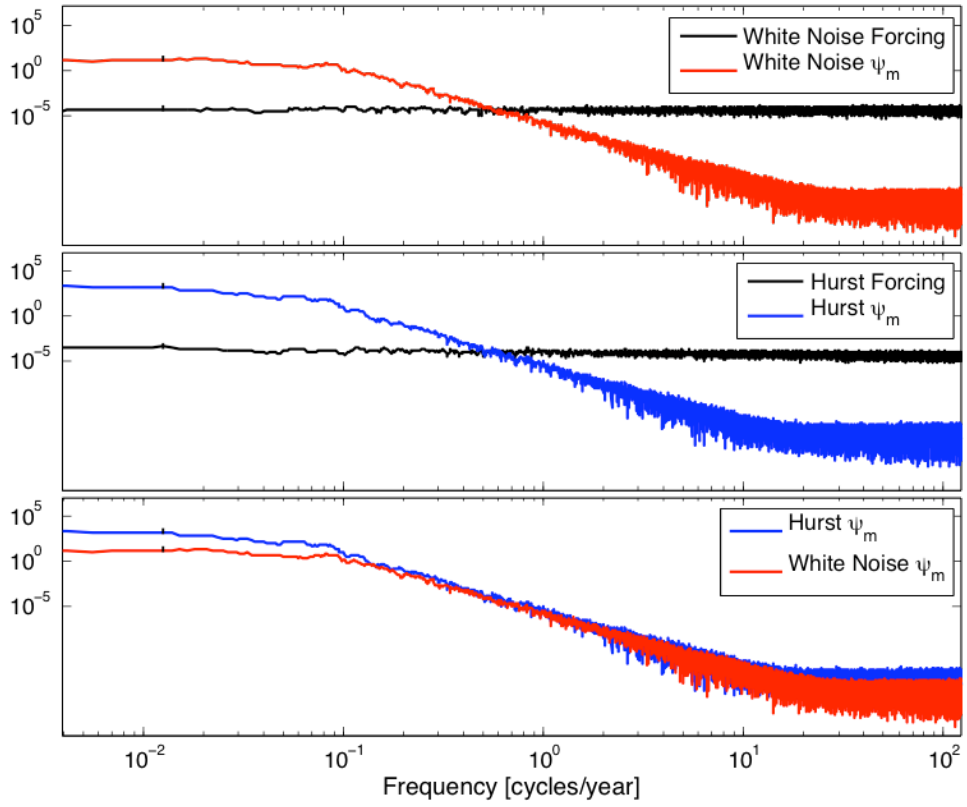

Figure 4.3 W3/WW3 MOC spectra comparison. Power spectra time series derived from synthetic (W3) and white noise (WW3) wind experiments. (Top) WW3 (white noise) wind forcing and MOC spectra, (middle) W3 (synthetic) wind forcing and MOC spectra, (bottom) comparison of spectra for WW3 and W3 MOC responses. Reddening of MOC response forced by the synthetic W3 forcing is apparent in the bottom panel.

lower frequency band. However, we also note that the spectra of oceanic response is redder compared to spectra of "realistic" synthetic atmospheric forcing. This agrees well with a previous studies suggesting that the ocean acts as a low-pass filter to high-frequency atmospheric forcing (e.g. Bjerknes, 1964). One of the most interesting results of this analysis appears in the bottom panel where we compare the resulting spectra of simulated MOC anomalies generated by synthetic wind forcing (blue), and white noise forcing (red). The spectra of the synthetically forced model results in a redder power spectra than that of the white noise model at low frequencies. A maximum of this effect occurs in the simulated ocean temperature anomaly spectra (Figure B.9), which suggests that the system may generate a low-frequency response to atmospheric forcing with a period defined by a selected spatial scale L_x. This spatial scale is defined by Marshall et al. (2001b) as the time required for the first baroclinic Rossby wave to cross the basin. The effect of reddening spectra shows a fundamental feature of the natural air-sea interaction, as the response of the ocean is redder than the atmospheric forcing (Frankignoul et al., 1997; Neelin and Weng, 1999). A complete set of spectral analysis for each Wind experiment may be found in Appendix B.

4.2 Results of SAT experiments

In this section the results of the SAT experiments using synthetic SAT forcing (S4) and white noise forcing (SS4) are presented. The results of experiment S4 are displayed in Figure 4.4. Examination of the S4 results revealed a moderate correlation between the MOC and Gyre anomaly responses as confirmed by R=0.69 with 0 time lag (SAT Experiment section of Table 4.1). This correlation was not as high as that of the wind experiment results, but the response was immediate and, more importantly, Ψ_m and Ψ_g were positively correlated. A correlation was also found between the smoothed synthetic SAT forcing and the MOC and Gyre anomaly responses. Analysis revealed a higher correlation of synthetic SAT forcing with the MOC anomaly responses (R=0.75 with lag=-6 years) than with the Gyre anomaly

responses (R=0.52 with lag=0 years). In addition a weaker anti-correlation of R=-0.37 was found between the synthetic SAT forcing and upper ocean temperature response. This was somewhat unexpected and was further examined by determining the analytical solution for the governing equations. With the governing upper ocean temperature equation as:

$$\frac{\partial T}{\partial t} = -\lambda + F_T \tag{4.1}$$

where our stochastic forcing is simplified to a cosine forcing wave,

$$F_T = cos(\Theta t) \tag{4.2}$$

the analytical solution is determined to be:

$$T(t) = \frac{\lambda cos(\Theta t) + \Theta\, sin(\Theta t)}{\lambda^2 + \Theta^2}. \tag{4.3}$$

Examining this analytical solution we find that the balance of the cosine and sine terms in the numerator of Eq. (4.3) play an important role in determining the correlations between the model forcing and results for this experiment. The damping coefficient λ will determine whether the model results are dominated by the cosine part of the solution in Eq. (4.3) or the shared importance of both thems in Eq. (4.3). As a result, the correlations determined in Table 4.1 for the SAT experiment between model forcings and upper ocean temperature responses should be investigated in subsequent studies relative to this damping coefficient.

Similarly to the wind experiment, the simulated ocean temperature anomaly response for experiment S4 correlates with the simulated Gyre anomalies. An anti-correlation of R=-0.77 was found between these two model responses with the Gyre anomalies lagging behind the ocean temperature anomalies by 3 years. This could be in indication of an air-sea interaction feedback in the model system. For instance, as the ocean temperature anomalies took on a positive trending for a period of time

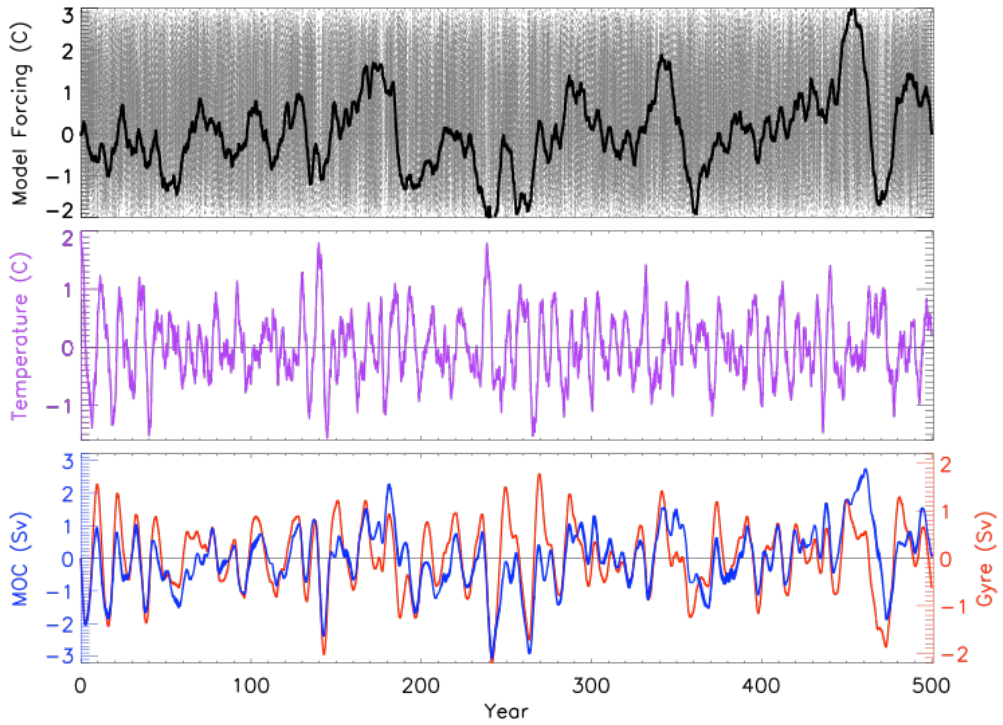

Figure 4.4 Model results for SAT experiment S4. Time series of simulated (middle) ocean temperature anomalies, (bottom) MOC (blue) and horizontal gyre (red, reverse axis) anomalies forced by (top) synthetic SAT. Upper panel shows daily (dashed line) and 7 year running mean (solid line) synthetic SAT forcing (°C).

in the northern portion of the basin, the N-S temperature gradient across the basin would eventually be weakened. Decreased temperature gradients would result in weaker thermal wind, thus forcing a negative gyre anomaly at some time delay. In the northern portion of the basin, the N-S temperature gradient across the basin would eventually be weakened. Decreased temperature gradients would result in weaker thermal wind, thus forcing a negative gyre anomaly at some time delay.

The results of the white noise forced SAT experiment (SS4) are notably different than those of the experiment with synthetic SAT forcing (S4). When comparing the two sets of model results (Figures 4.4 and 4.5), the most prominent difference is the decreased amplitude of the SS4 model forcing as well as each of the model system responses. Visually it is difficult to decipher any clear correlations in

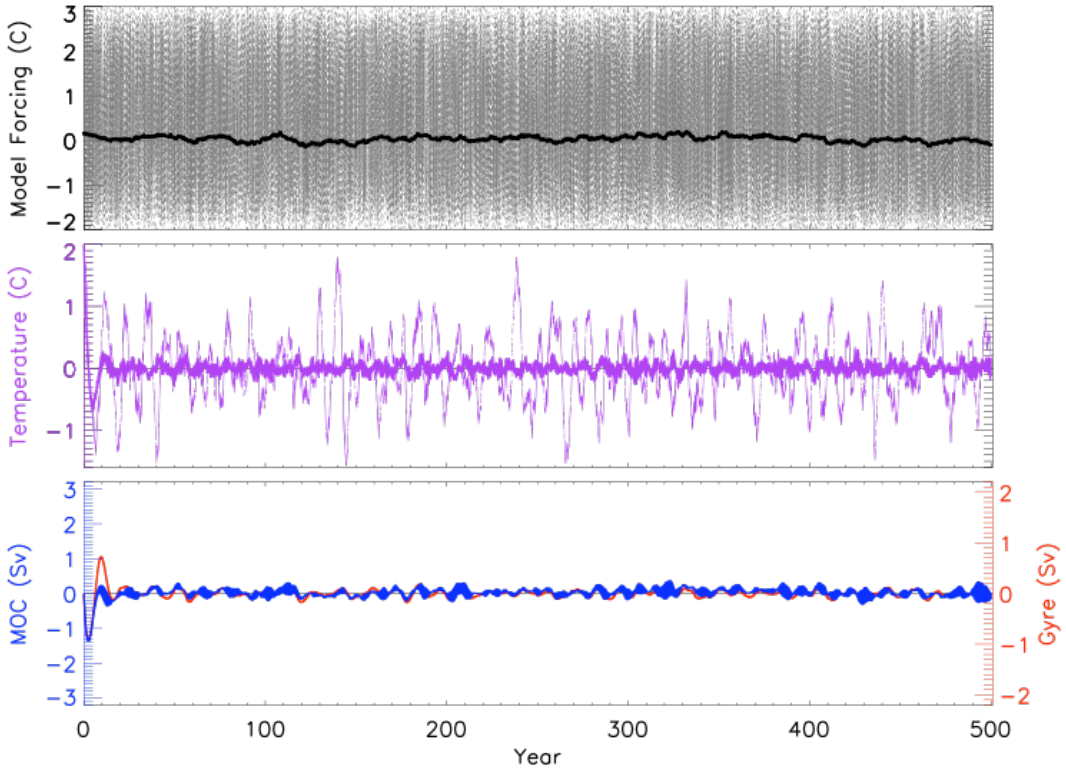

Figure 4.5 Model results for SAT experiment SS4. Figure panels are displayed as in Figure 4.4 with the addition of the S4 simulated ocean temperature anomaly time series (thin dashed purple line) in the middle panel.

the SS4 model results, however statistical analysis revealed a correlation of R=0.75 with no time lag between the simulated MOC and Gyre anomalies similar to Wind experiment WW4. In addition, an anti-correlation of R=-0.69 was found between the simulated ocean temperature anomalies and Gyre anomalies, with the Gyre anomalies once again responding to the ocean temperature anomalies with a lag of 3 years. While the SS4 white noise SAT forcing does not correlate highly with any of the model system components, the correlations between individual system components for this experiment agree remarkably well with those of the synthetically forced SAT experiment S4, suggesting that internal relations in the system play the key role in damping the system response to external forcing. Similar model results are present between system components regardless of

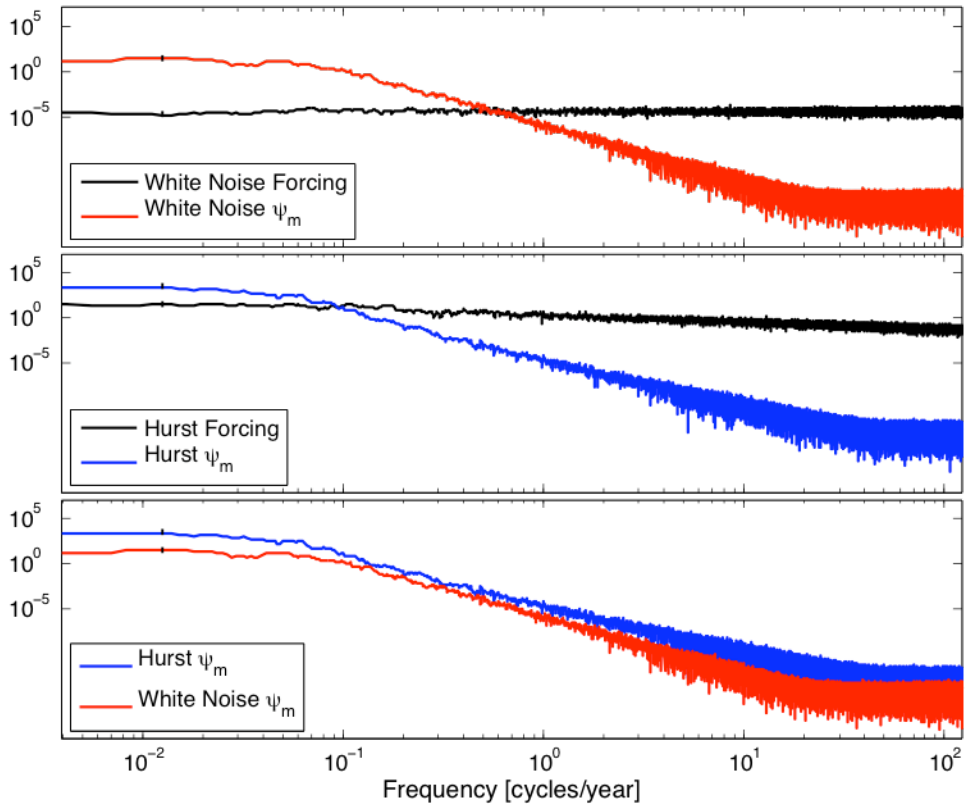

Figure 4.6 S4/SS4 MOC spectra comparison. Power spectra for synthetic (S4) and white noise (SS4) SAT experiments. (Top) power spectra of SS4 (white noise) SAT forcing and MOC, (middle) power spectra of S4 (synthetic) SAT forcing and MOC, (bottom) comparison of spectra for SS4 and S4 MOC responses. Reddening of MOC response forced by the synthetic S4 forcing is apparent in the bottom panel.

forcing, while correlations are enhanced when the synthetic forcing is utilized in driving the model.

Spectral analysis of the S4 and SS4 forcing and simulated MOC anomaly time series (Figure 4.6) further confirmed the validity of the above findings. Similar to the Wind experiment, the results of this analysis show a prominent result in the bottom panel of Figure 4.6. At low frequencies the spectra of the synthetically forced model is redder than that of the white noise forced model, even more than the Wind experiment results, reaffirming the presence of natural air-sea interaction,

where the ocean response is redder than that of the atmospheric forcing, in this case forced by SAT (Frankignoul et al., 1997; Neelin and Weng, 1999). Spectral analysis of simulated ocean temperature, MOC, and gyre anomalies by synthetic (S4) and white noise (SS4) forcing may be found in Appendix C.

4.3 Results of Labrador experiment

The results of the Labrador experiments forced using synthetic (L4) and white noise (LL4) forcing are presented in this section. The results of the Labrador experiment (L4) are shown in Figure 4.7. Each of the model system component responses in this experiment have an initially large oscillation (the extreme values of this oscillation are beyond the y-axis limits for the middle and bottom panel of

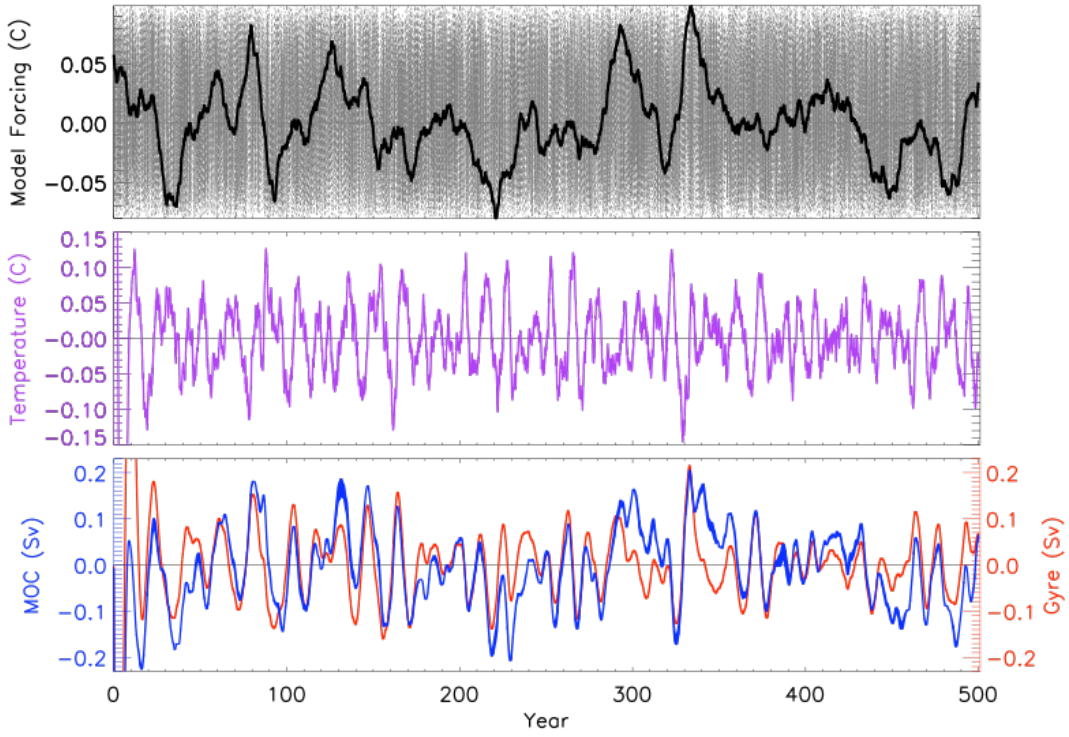

Figure 4.7 Model results for Labrador experiment L4. Time series of simulated (middle) ocean temperature anomalies, (bottom) MOC (blue) and horizontal gyre (red) anomalies forced by (top) synthetic Labrador. Upper panel shows daily (dashed line) and 7 year running mean (solid line) Labrador forcing (°C).

Figure 4.7), which was, probably due to numerical reasons, dampened to within ~20 years, and this part of the record was eliminated from the following analysis.

The L4 experiment MOC and Gyre anomaly responses display similar variability like that of the SAT experiments. This qualitative observation is confirmed quantitatively by the statistical correlation R=0.74 with no time lag (Labrador Experiment section of Table 4.1). Additionally an anti-correlation was found between the ocean temperature anomaly and gyre anomaly responses with the gyre anomaly time series responding to the ocean temperature anomaly with a lag of 3 years and a correlation R=-0.69. This correlation is also similar to the one calculated for the SAT experiments, further supporting air-sea interaction feedback of the ocean temperatures on the gyre dynamics.

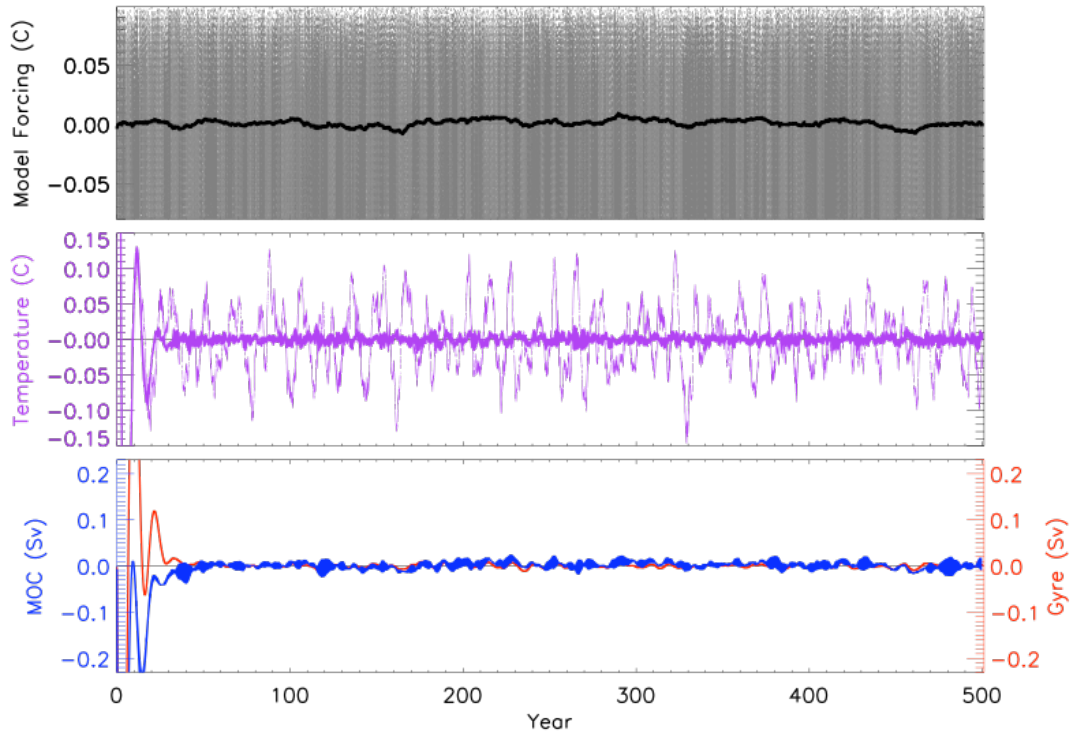

Figure 4.8 Model results for Labrador experiment LL4. Figure panels are displayed as in Figure 4.7 with the addition of the L4 simulated ocean temperature anomaly time series (dashed purple line) in the middle panel.

The white noise forced Labrador experiment (LL4) results displayed in Figure 4.8 illustrate once again the smaller amplitude of the smoothed white noise forcing compared with the smoothed synthetic forcing (Figure 4.7). This feature can also be seen in the middle panel of Figure 4.8 with the simulated ocean temperature anomalies by synthetic forcing (dashed purple line) oscillating nearly a factor of 10 higher than the oscillations of those by white noise forcing (solid purple line). The damping of the simulated model system components is also apparent in the results of this white noise forced experiment similar to the other Labrador experiments.

Visual correlations between the LL4 results were difficult to discern, however statistical analysis (Table 4.1) revealed a high correlation (R=0.62) between the simulated MOC and Gyre anomaly time series, similar to all previously discussed experiment results. A similar anti-correlation of R=-0.64 was found with simulated gyre anomalies lagging behind ocean temperature anomalies by 3 years. Furthermore, correlations between the white noise Labrador forcing time series and simulated model system component results were even weaker than those determined for the L4 experiment. These similar correlation patterns reaffirm the consistency of the model system component interactions within the model regardless of forcing mechanism.

The spectra of the simulated MOC anomaly time series as well as the L4 and LL4 Labrador forcing are displayed in Figure 4.9. These spectra results are very similar to those found in the previously discussed experiments (Figures 4.6 and 4.3). The synthetically forced model results display a slightly redder spectra than the spectra of the white noise forced model when examining low frequencies (bottom panel Figure 4.9). These low frequencies are important when investigating feedback mechanisms at the air-sea interface and these results further support the synthetic model forcing methodology. Additional spectra analysis for the set of Labrador experiments may be found in Appendix D.

It should be noted that the placement of the Labrador forcing term in Equation 3.1 may need further evaluation. We included the Labrador forcing in this

equation assuming the existence of relation between observed northern basin SST and 50-500 m Labrador Sea potential temperature as confirmed by a modest correlation (R=0.34, lag=0). There are, however, reasons to believe that convective processes in the sub-arctic seas may also impact horizontal ocean gyre circulations (Lab Sea Group, 1998), and vertical MOC ocean circulations (Pickart and Spall, 2007; Schott et al., 2009). Therefore, the Labrador forcing term would also be included in Eqs. 3.2 and 3.3, however due to the lack of observations, correlations between

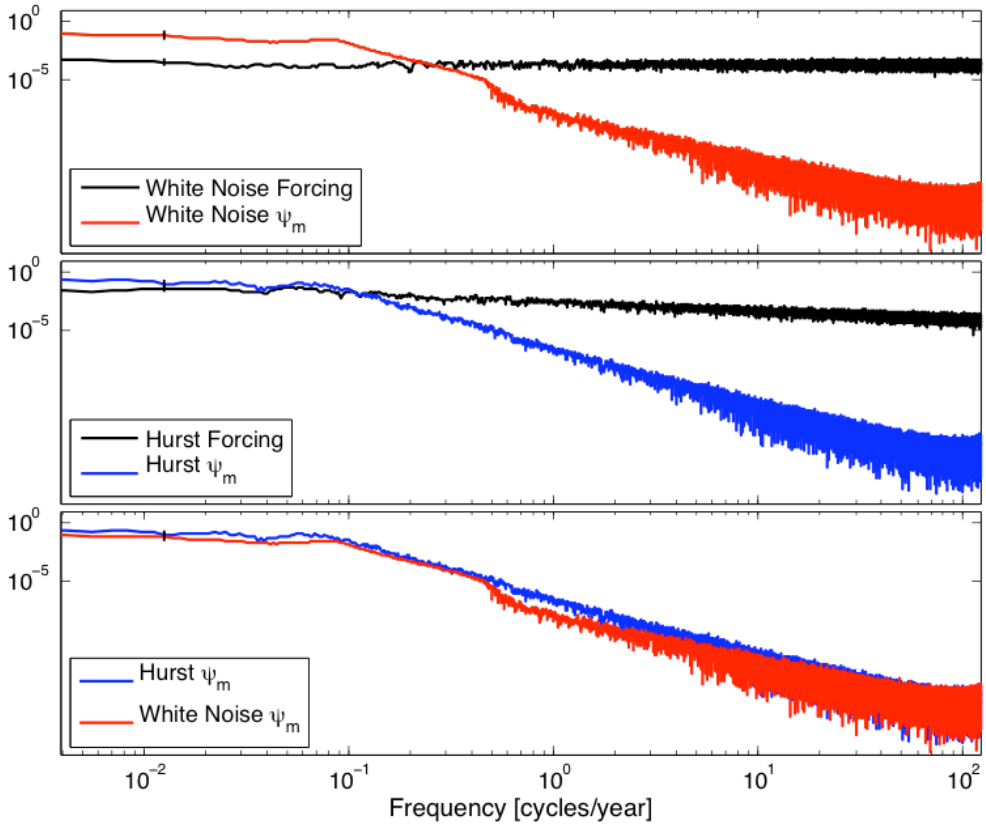

Figure 4.9 L4/LL4 MOC spectra comparison. Power spectra time series derived from synthetic (L4) and white noise (LL4) Labrador experiments. (Top) LL4 (white noise) Labrador forcing and MOC spectra, (middle) L4 (synthetic) Labrador forcing and MOC spectra, (bottom) comparison of spectra for LL4 and L4 MOC responses. Reddening of MOC response forced by the synthetic L4 forcing is apparent in the bottom panel.

MOC, Gyre, and Labrador Sea temperature could not be calculated. This hindered our ability to determine weights for the Labrador forcing for Eqs. 3.2 and 3.3. Further evaluation of these equations may be performed by modeling studies involving GCM simulations.

4.4 Results of General experiments

The General experiments were forced with a combination of Wind, SAT, and Labrador forcings, and are presented in this final section. Figure 4.10 displays the results of the synthetically forced General experiment (G1) with each of the

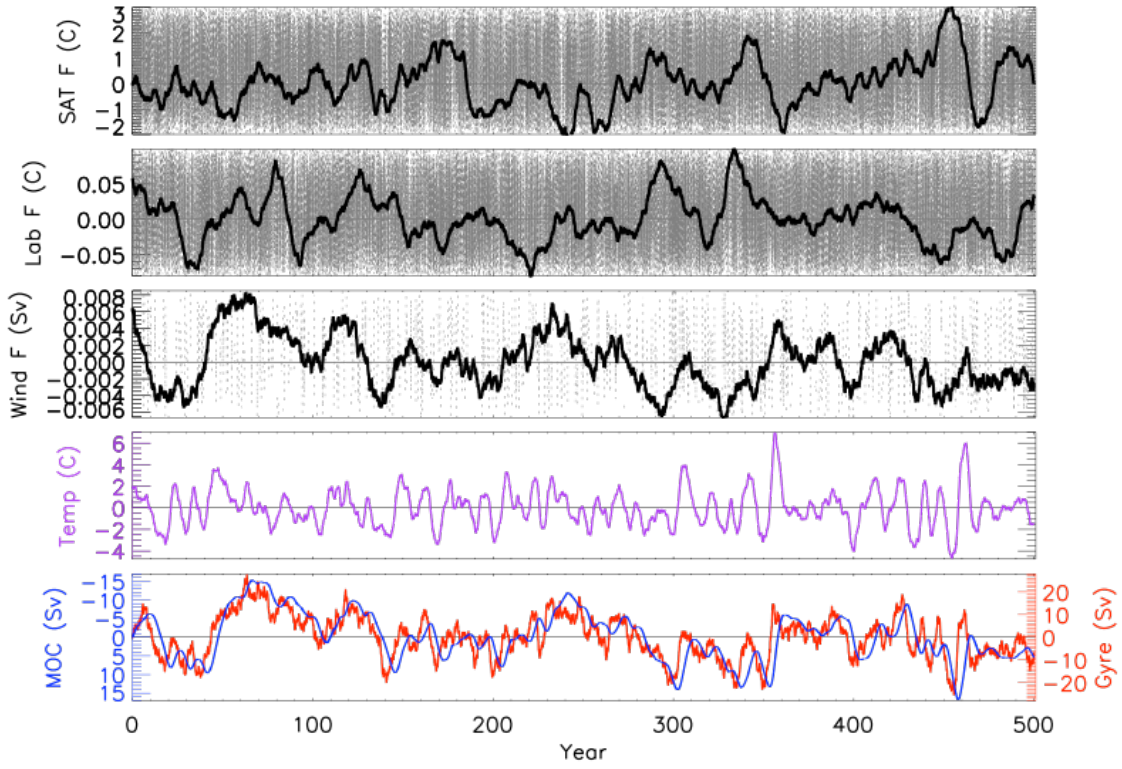

Figure 4.10 Model results for General experiment G1. Simulated time series of ocean temperature response (°C, 4th panel), MOC (blue) and horizontal gyre (red) anomalies (Sv, 5th panel) forced by the most complete synthetic forcing including SAT forcing (°C, 1st panel), Labrador forcing (°C, 2nd panel) and Wind forcing (Sv, 3rd panel). Note that the MOC scale is shown using a reverse scale. A striking correlation is apparent between the Wind forcing (3rd panel) and MOC and Gyre responses (5th panel).

individual forcings displayed in the top three panels, and the simulated model component results displayed in the bottom two panels. One of the most striking features of Figure 4.10 is the apparent dominance of the Wind forcing over the Labrador and SAT forcings. Remarkable agreement is evident between the smoothed wind forcing and the simulated MOC and Gyre anomalies, while similar conformities do not appear between the other two forcings and simulated results. This prominent feature is nearly indistinguishable from the coinciding responses of the synthetic Wind experiment (W3, Figure 4.1), suggesting that the wind forcing dominates other forcings in this General experiment. My results agree with a modeling study by Kushnir (1994) suggesting that inter-decadal SST variability may be governed by a basin-scale dynamical interaction between the large-scale oceanic circulation and the atmosphere, similar to the hypothesis proposed by Bjerknes (1964). In addition, a modeling study by Neelin and Weng (1999) found that atmospheric internal variability alone provided coherent spatial patterns in the oceanic response owing to large-scale atmospheric stochastic forcing.

The patterns of the simulated MOC and Gyre temporal anomalies appear to correspond very well. Statistical correlation analysis (Table 4.1) confirms this visual agreement, revealing a remarkable anti-correlation of R=-0.93 with the simulated MOC anomaly time series responding to the simulated Gyre anomaly time series with a lag of 4 years. A weaker correlation (R=0.52) is found between the simulated ocean temperature response and the simulated gyre response at zero lag. Both of these correlations are nearly identical to the corresponding correlations for the synthetic Wind experiment (W3, Table 4.1), providing further evidence of the dominant role of wind forcing in the General experiment.

The white noise forced General experiment (GG1) results are presented in Figure 4.11. Similar to the previously discussed experiment results, the white noise forced results in this study display weaker temperature and MOC amplitudes when compared with the corresponding synthetically forced experiment (Figure 4.10). While slightly harder to discern due to the vertical scale, a slight correlation seems

noticeable between the simulated MOC and Gyre anomaly results. The correlation analysis confirms this feature as the simulated MOC anomaly time series lags behind the simulated Gyre anomaly time series with an anti-correlation of R=-0.76. Further statistical analysis reveals a correlation of R=0.77 with simulated ocean temperature anomalies responding to simulated gyre anomalies with a lag of 1 year. Remarkably these correlations and time lags also agree considerably well with the coinciding white noise Wind experiment (WW3) results (Table 4.1), reaffirming the dominance of the wind forcing in the General experiments.

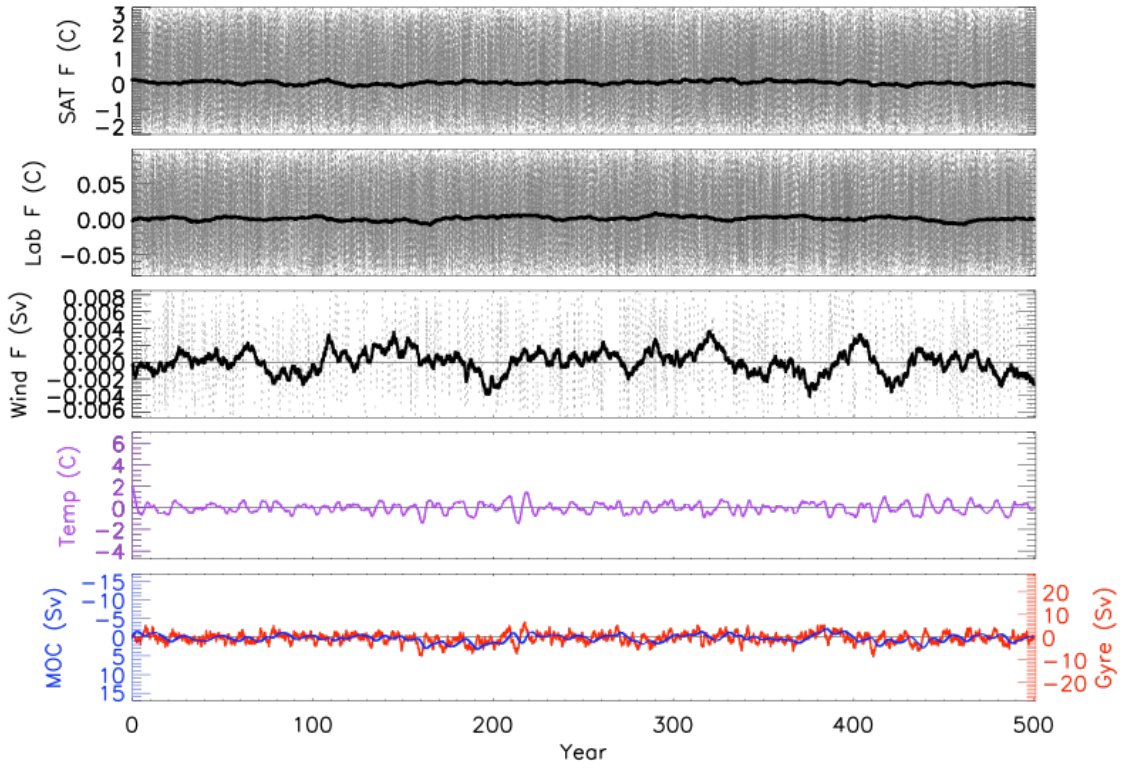

Figure 4.11 Model results for General experiment GG1. Simulated time series of ocean temperature (°C, 4th panel) and MOC and horizontal gyre (Sv, 5th panel) anomalies forced by most complete white noise forcing including SAT forcing (°C, 1st panel), Labrador forcing (°C, 2nd panel), and Wind forcing (Sv, 3rd panel), similar to panels displayed in Fiogure 4.10. Note that for comparison purposes all panels use the same vertical axes as those used in Figure 4.10, showing the results of the simulations with "realistic" forcing.

5. Conclusions

In this chapter of the thesis the overall study is summarized followed by the presentation and discussion of the main results from my set of model experiments. Additionally, ideas are presented for further investigation with the box model.

5.1 Summary

In this study, mechanisms driving the North Atlantic variability are investigated using a simple box model. The box model is based upon the framework developed by Marshall et al. (2001b), involving time evolution of interacting upper ocean temperature anomalies, horizontal ocean Gyre, and vertical MOC ocean circulations driven by stochastic SAT, wind, and Labrador forcings. In addition to the mechanisms proposed by Marshall et al., (2001b), a Labrador Sea forcing imitating the impact of deep-ocean convection frequently observed in the Labrador Sea is incorporated, thus taking into account that deep-ocean convection in the sub-arctic seas may be important to the North Atlantic variability. While previous studies used similar box models using white noise timeseries (e.g. Frankignoul et al., 1997; Frankignoul et al., 1998; Marshall et al., 2001b), a set of stochastic forcings based upon statistical properties of actual basin observations was also developed. Note that the general box-model design was proposed by Marshall et al. (2001b), however a full system response to external forcing was implemented here as an extension of their analysis, which only included evaluation of behavior of the system components. The synthetic forcing timeseries, along with similar white noise forcing timeseries, were evaluated in a series of model experiments in order to provide new insight into the mechanisms driving North Atlantic variability.

5.2 Main results and future work

In all of the experiments, the synthetically forced model responses resulted in redder spectra than those forced by white noise. This suggests that the ocean acts as a low-pass filter for the applied atmospheric forcing, resulting in the reddened

spectra in these experiments (Hasselmann, 1976; Frankignoul and Hasselmann, 1977; Battisti et al., 1995; Frankignoul et al. 1998; Marshall et al., 2001b).

Another new finding of this project was the strong correspondence between the smoothed synthetic wind forcing and the simulated Gyre and MOC responses. The correlation between the Wind forcing and resulting Gyre anomalies was R=0.83 with a lag of 6 years, while the anti-correlation with the resulting MOC anomalies was R=-0.92 with a lag of 8 years. This finding implies that the simulated ocean response was a reaction of the system to the cumulative effect of atmospheric forcing averaged over a limited time window; the width of the window is defined by damping properties of the system and in the Wind experiment the interval was found to be 7 years. Caution should however be added to the determination of a specific time frame since it may vary dependent upon the non-dimensional scaling factors utilized in the model, thus this feature should be further evaluated. This cummulative effect is confirmed in theoretical analyses showing practically identical spectral transfer functions, one of which links spectra of external forcing and the reaction of the system for the model as shown by Frankignoul et al. (1997), and another describes the effect of the running mean operation averaging (Bekryaev, personal communication).

Experiment results clearly demonstrated the dominance of the Wind forcing over SAT and Labrador forcings. The simulated model responses suggest that the wind forcing is the foremost mechanism driving changes for the North Atlantic upper ocean temperature anomalies as well as the intensity of both the horizontal and vertical cells of the ocean circulation. This finding is consistent with results of a modeling study by Kushnir (1994). Kushnir suggested that inter-decadal SST variability may be governed by a basin-scale dynamical interaction between the large-scale oceanic circulation and the atmosphere, similar to the hypothesis proposed by Bjerknes (1964). This finding is further supported by the results of a modeling study by Neelin and Weng (1999) who found that atmospheric internal

variability alone provided coherent spatial patterns in the oceanic response owing to large-scale atmospheric stochastic forcing.

The strong anti-correlation found between the simulated Gyre and MOC suggests a mechanism in which the horizontal Gyre circulation and vertical MOC circulation act together to compensate for a lack or excess supply of heat northward, thus maintaining the heat balance in the system. Based on the results of this analysis, the compensation mechanism can be explained by an initially induced wind forcing on the model, resulting in a strengthened horizontal Gyre circulation cell. Over a period of time this circulation increases the net pole-ward transfer of heat, increasing the average SST over the northern portion of the basin, in turn decreasing the N-S temperature gradient. This weakened temperature gradient results in a weaker vertical MOC circulation, decreasing the net pole-ward heat transport, which would be compensated for by an enhanced horizontal Gyre circulation increasing net pole-ward heat transport. A somewhat similar mechanism was proposed by Bjerknes (1964), who suggested that atmosphere and ocean work together in order to stabilize northward heat supply in the atmosphere-ocean system and the deficit of heat transport by the atmosphere is compensated for by enhanced oceanic heat transport and vise versa. This mechanism may exist in the ocean alone through heat flux compensations provided by intensification of one (horizontal or vertical) component of oceanic circulation and simultaneous weakening of another component. A similar compensation mechanism was also proposed by Marshall et al. (2001b) and is presented schematically in Figure 2.8. They propose that shifts in the phase of the NAO induce changes in intergyre gyre circulations, altering the meridional heat transport, which is compensated for by adjustments of heat transport by MOC circulation.

Following the discussion above, the major findings are summarized as follows:

- The simulated response of the upper North Atlantic Ocean to atmospheric forcing using the box model, results in model solutions with redder spectra than the spectra of atmospheric forcing. This fact implies that the ocean acts as a low-pass filter utilizing the lower-frequency part of the forcing.
- The simulated ocean dynamic response may be viewed as a cumulative effect of atmospheric forcing over limited time; the length of the time interval is defined by the damping properties of the system.
- A strong anti-correlation between the simulated intensity of horizontal (gyre) and vertical (MOC) circulation cells suggests a mechanism, in which heat balance in the system is maintained via communication between these two dynamic system components. For instance, an increase of heat supplied by an anomalously strong gyre circulation would be balanced by a decrease of heat provided by a weaker MOC circulation and vise versa.
- The model suggests that wind is the dominant forcing for the North Atlantic upper ocean temperature anomalies and the intensity of both horizontal and vertical cells of the ocean circulation.
- Further investigation of parameterizations of thermal damping and heat transport used in the model is necessary to better understand simulated feedbacks and interactions.

The investigation of air-sea interactions over the North Atlantic utilizing a simple stochastically-forced box model provided a means for discerning the feedbacks and mechanisms impacting variability in the basin. Links identified in simple models such as the one presented in this study are useful as they may be compared with results found in more complex models and observations. Finally, the importance of continuing to investigate the mechanisms driving North Atlantic variability may be stressed, as these climate variability patterns are of great

importance to sustaining the global transport of heat in the ocean through the thermohaline circulation, and the implications of a weakened MOC should be taken seriously. Furthermore, attempts to better understand mechanisms driving variability over the basin should continue, with the focus on changes occurring in the atmosphere, air-sea interface, as well as the interior ocean.

References

Alessio, E., A. Carbone, G. Castelli, and V. Frappietro, 2002: Second-order moving average and scaling of stochastic time series. *European Physical Journal B,* 27: 197.

Alexander, M.A. and C. Deser, 1995: A mechanism for the recurrence of wintertime midlatitude SST anomalies. *Journal of Physical Oceanography,* 25: 122–137.

Bacon, S. and J.T. Carter, 1993: A connection between mean wave height and atmospheric pressure gradient in the North Atlantic. *International Journal of Climatology,* 13: 423–436.

Baldwin, M.P. and T.T. Dunkerton, 1999: Propagation of the Arctic Oscillation from the stratosphere to the troposphere. *Journal of Geophysics Research*, 104: 30937–30946.

Barnston, A. and R.E. Livezey, 1987: Classification, seasonality and persistence of low-frequency circulation patterns. *Monthly Weather Review,* 115: 1083–1126.

Barsugli, J.J. and D.S. Battisti, 1998: The basic effects of atmosphere-ocean thermal coupling on middle-latitude variability. *Journal of Atmospheric Science,* 55: 477–493.

Battisti, D.S., U.S. Bhatt, and M.A. Alexander, 1995: A modeling study of the interannual variability in the North Atlantic Ocean. *Journal of Climate,* 8: 3067-3083.

Belkin, I.M., S. Levitus, J. Antonov, and S.A. Malmberg, 1998: Great Salinity Anomalies in the North Atlantic. *Progress in Oceanography*, 41: 1–68.

Beniston, M., 1997: Variations of snow depth and duration in the Swiss Alps over the last 50 years: links to changes in large-scale climatic forcings. *Climatic Change,* 36: 281–300.

Bjerknes, J., 1964: Atlantic air – sea interaction. *In Advances in Geophysics*, vol. 10, Landberg, H.E., J. van Mieghem (eds). Academic Press: New York; 1–82.

Broecker, W.S. and G.H. Denton, 1989: The role of ocean – atmosphere reorganizations in glacial cycles. *Geochimica et Cosmochimica Acta,* 53: 2465–2501.

Carbone, A., G. Castelli, and H. Stanley, 2004: Time dependent Hurst exponent in financial time series, *Physica.* A344 (1–2) 267–271.

Cayan, D.R., 1992: Latent and sensible heat-flux anomalies over the northern oceans — the connection to monthly atmospheric circulation. *Journal of Climate,* 5: 354–369.

Cessi, P., 2000: Thermal feedback on wind stress as a contributing cause of climate variability. *Journal of Climate*, 13(1): 232–244.

Chapra, S.C. and R.P. Canale, 2006: Numerical Methods for Engineers, 5th ed., McGraw-Hill Company Inc., 926 pp.

Curry, R.G. and M.S. McCartney, 2001: Ocean gyre circulation changes associated with the North Atlantic Oscillation. *Journal of Physical Oceanography,* 31: 3374– 3400.

Czaja, A. and C. Frankignoul, 1999: Influence of the North Atlantic SST anomalies on the atmospheric circulation. *Geophysics Research Letters,* 26: 2969–2972.

Czaja, A. and C. Frankignoul, 2002: Observed impact of Atlantic SST anomalies on the North Atlantic Oscillation. *Journal of Climate*, 15, 606-623.

Czaja, A. and J. Marshall, 2001: Observations of Atmosphere Ocean coupling in the North Atlantic. *Quarterly Journal of the Royal Meteorological Society*, 127: 1893–1916.

Delworth, T.L. and K.W. Dixon, 2000: Implications of the recent trend in the Arctic/North Atlantic Oscillation for the North Atlantic thermohaline circulation. *Journal of Climate,* 13: 3721–3727.

Delworth, T.L. and M. E. Mann, 2000: Observed and simulated multidecadal variability in the Northern Hemisphere. *Climate Dynamics,* 16: 661–676.

Delworth, T.L., S. Manabe, and R.J. Stouffer, 1993: Interdecadal variations of the thermohaline circulation in a coupled ocean-atmosphere model. *Journal of Climate,* 6: 1993–2011.

Deser, C. and M.L. Blackmon, 1993: Surface climate variations over the North Atlantic Ocean during winter: 1900 – 1989. *Journal of Climate*, 6: 1743–1753.

Dickson, R., J. Lazier, J. Meincke, P. Rhines, and J. Swift, 1996: Long-term co-ordinated changes in the convective activity of the North Atlantic. *Progress in Oceanography,* 38: 241–295.

Dickson, B., I. Yashayaev, J. Meincke, B. Turrell, S. Dye, and J. Holfort, 2002: Rapid freshening of the deep North Atlantic ocean over the past four decades. *Nature*, 416: 832–837.

Encyclopædia Britannica, 2010: Atlantic Ocean. *Encyclopædia Britannica Online*, Retrieved January 28, 2010, http://www.britannica.com/EBchecked/topic/41191/Atlantic-Ocean.

Enfield, D.B. and D.A. Mayer, 1997: Tropical Atlantic sea surface temperature variability and its relation to El Nino Southern Oscillation. *Journal of Geophysical Research — Oceans,* 102: 929–945.

Enfield, D.B., D.A. Mayer, and P.J. Trimble, 2001: The Atlantic multidecadal oscillation and its relation to rainfall and river flows in the continental U.S. *Geophysical Research Letters*, 28, 2077–2080.

Esbensen, S.K., 1984: A comparison of intermonthly and interannual teleconnections in the 700 mb geopotential height field during the Northern Hemisphere winter. *Monthly Weather Review,* 112: 2016–2032.

Feder, J., 1988: *Fractals.* Plenum Press, 283 pp.

Folland, C.K., N.A. Rayner, S.J. Brown, T.M. Smith, S.S.P. Shen, D.E. Parker, I. Macadam, P.D. Jones, R.N. Jones, N. Nicholls, and D.M.H. Sexton, 2001: Global temperature change and its uncertainties since 1861. *Geophysical Research Letters,* 28: 2621-2624.

Frankignoul, C. and K. Hasselmann, 1977: Stochastic climate models, Part II: Application to sea-surface temperature variability and thermocline variability. *Tellus,* 29: 289-305.

Frankignoul, C, 1985: Sea surface temperature anomalies, planetary waves and air-sea feedback in the middle latitudes, *Review of Geophysics*, 23, 357-390.

Frankignoul, C., P. Muller, E. Zorita, 1997: A simple model of decadal response of the ocean to stochastic wind forcing. *Journal of Physical Oceanography,* 27: 1533-1546.

Frankignoul, C., A. Czaja, and B. L'Heveder, 1998: Air – sea feedback in the North Atlantic and surface boundary conditions for ocean models. *Journal of Climate,* 11: 2310–2324.

Glantz, M.H., 1996: Currents of Change: El Niño's Impact on Climate and Society. *Cambridge University Press*. 194 pp.

Goldenberg, S.B., C.W. Landsea, A.M. Mestas-Nuñez, and W.M. Gray, 2001: The recent increase in Atlantic hurricane activity: Causes and implications: *Science*, v. 293, 5529: 474–479, doi: 10.1126/science.1060040.

Goodman, J. and J. Marshall, 1999: A model of decadal middle-latitude atmosphere-ocean coupled modes. *Journal of Climate*, 12: 621–641.

Gray, W.M, 1990: Strong association between west African rainfall and US landfall of intense hurricanes. *Science*, 249: 1251–1256.

Gray, S.T., L.J. Graumlich, J.L. Betancourt, and G.T. Pederson, 2004: A tree-ring based reconstruction of the Atlantic Multidecadal Oscillation since 1567 A.D. *Geophysical Research Letters*, 31:L12205, doi:10.1029/2004GL019932.

Hakkinen, S., 2000: Decadal air – sea interaction in the North Atlantic based on observations and modeling results. *Journal of Climate,* 13: 1195–1219.

Hall, M.M. and H.L. Bryden, 1982: Direct estimates and mechanisms of ocean heat transport. *Deep Sea Research*, 29: 339–359.

Hameed, S. K.R. Sperber, and A. Meinster, 1993: Teleconnections of the Southern Oscillation in the tropical Atlantic sector in the OSU coupled ocean – atmosphere GCM. *Journal of Climate,* 6: 487–498.

Hasselman, K., 1976: Stochastic climate models. Part I: theory. *Tellus*, 28: 289–305.

Hendry, R.M., 1982: On the structure of the deep Gulf Stream. *Journal of Marine Research*, 40, 119-142.

Hogg, N.G., 1992: On the transport of the Gulf Stream between Cape Hatteras and the Grand Banks. *Deep-Sea Research*, 39, 1231-1246.

Hurrell, J.W., 1995a: Transient eddy forcing of the rotational flow during northern winter. *Journal of Atmospheric Science*, 52: 2286–2301.

Hurrell, J.W., 1995b: Decadal trends in the North-Atlantic Oscillation: regional temperatures and precipitation. *Science*, 269: 676–679.

Hurrell, J.W., Y. Kushnir, M. Visbeck, and G. Ottersen, 2003: An Overview of the North Atlantic Oscillation. *The North Atlantic Oscillation: Climate Significance and Environmental Impact,* J.W. Hurrell, Y. Kushnir, G. Ottersen, and M. Visbeck, Eds. Geophysical Monograph Series, 134, pp. 1-35.

Hurrell, J. W., and C. Deser, 2009: North Atlantic climate variability: The role of the North Atlantic Oscillation. *J. Mar. Syst.*, 78, No. 1, 28-41, DOI:10.1016/j.jmarsys.2008.11.026.

Hurst, H. E., 1951: Long-term storage capacity of reservoirs. *Transactions of the American Society of Civil Engineers*, 116: 770–808.

IPCC, 2007: IPCC fourth assessment report. *Intergovernmental Panel on Climate Change*, 106 pp.

Jin, F.F., 1997: A theory of interdecadal climate variability of the north Pacific ocean – atmosphere system. *Journal of Climate,* 10: 324–338.

Kalnay, et al., 1996: The NCEP/NCAR 40-year reanalysis project, *Bulletin of the American Meteorological Society*, 77: 437-470.

Kerr, R.A., 1997: A new driver for the Atlantic's moods and European weather? *Science*, 275: 754-755.

Klein, S.A., B.J. Soden, and N.C. Lau, 1999: Remote sea surface temperature variations during ENSO: evidence for a tropical atmospheric bridge. *Journal of Climate*, 12: 917–932.

Knight, J. R., R. J. Allan, C. K. Folland, M. Vellinga, and M. E. Mann, 2005: A signature of persistent natural thermohaline circulation cycles in observed climate, *Geophysical Research Letters,* 32, L20708, doi:10.1029/ 2005GL024233.

Kodera, K., H. Koide, and H. Yoshimira, 1999: Northern hemisphere winter circulation associated with the North Atlantic Oscillation and the stratospheric polar night jet. *Geophysical Research Letters,* 26: 443–446.

Kushnir, Y., and J.M. Wallace, 1989: Low-frequency variability in the Northern Hemisphere winter-geographical-distribution, structure and time-scale dependence. *Journal of Atmospheric Science,* 46: 3122–3142.

Kushnir, Y., 1994: Interdecadal variations in North-Atlantic sea-surface temperature and associated atmospheric conditions. *Journal of Climate,* 7: 141–157.

Kushnir, Y., V.J. Cardone, J.G. Greenwood, and M. Cane, 1997: On the recent increase in North Atlantic wave heights. *Journal of Climate,* 10: 2107–2113.

Lab Sea Group, 1998: The Labrador Sea deep convection experiment, *Bulletin of the American Meteorological Society,* 79: 2033-2058.

Lan, L.W., F.Y. Lin, and Y.C. Huang, 2003: Diagnosis of freeway traffic incidents with Chaos Theory. *Journal of the Eastern Asia Society for Transportation Studies,* 5: 2025-2038.

Latif, M., 2001: Tropical Pacific/Atlantic Ocean interactions at multi-decadal time scales. *Geophysical Research Letters,* 28: 539-54.

Latif, M. and T.P. Barnett, 1994: Causes of decadal climate variability in the North Pacific/North Atlantic sector. *Science,* 266: 634–637.

Lavin, A., H.L. Bryden, and G. Parrilla, 1998: Meridional transport and heat flux variations in the subtropical North Atlantic. *The Global Atmosphere and Ocean System*, 6: 269–293.

LeVeque, R. J., 2002: *Finite Volume Methods for Hyperbolic Problems*. Cambridge University Press. 578 pp.

Levitus, S., 1989: Interpentadal variability of temperature and salinity at intermediate depths of the North Atlantic Ocean, 1970 – 1974 versus 1955 – 1959. *Journal of Geophysics Research,* 94: 6091–6131.

Marotzke, J., 2000: Abrupt climate change and thermocline circulation: mechanisms and predictability. *Proceedings of the National Academy of Sceinces,* 97: 1347–1350.

Marshall, J. and F. Molteni, 1993: Toward a dynamical understanding of planetary-scale flow regimes. *Journal of Atmospheric Science,* 50: 1792–1818.

Marshall, J. and F. Schott, 1999: Open ocean deep convection: observations, models and theory. *Review of Geophysics*, 37: 1-64.

Marshall, J., Y. Kushnir, D. Battisti, P. Chang, A. Czaja, R. Dickson, M. McCartney, R. Saravanan, and M. Visbeck, 2001a: North Atlantic Climate Variability: phenomena, impacts and mechanisms. *International Journal of Climatology*, vol.21, No.15, 1863-1898.

Marshall, J., H. Johnson, and J. Goodman, 2001b: Interaction of the North Atlantic Oscillation with ocean circulation. *Journal of Climate,* vol 14, no 7, 1399-1421.

Marshall, J. and R.A. Plumb, 2008: *Atmosphere, Ocean, and Climate Dynamics: An Introductory Text*. Elsevier Academic Press Press. 319 pp.

McCartney, M.S. and L. D. Talley, 1984: Warm-to-cold water conversion in the northern North Atlantic Ocean. *Journal of Physical Oceanography*, 14: 922-935.

McCartney, M. S., 1997: Is the Ocean at the Helm? *Nature*, 388: 521-522.

Neelin, J.D. and W. Weng, 1999: Analytical prototypes for ocean-atmosphere interaction at midlatitudes. Part I: coupled feedbacks as a sea surface temperature dependent stochastic process. *Journal of Climate,* 12(3): 697–721.

Nobre, P. and J. Shukla, 1996: Variations of sea surface temperature, wind stress, and rainfall over the tropical Atlantic and South America. *Journal of Climate,* 9: 2464–2479.

Perlwitz, J. and H.F. Graf, 1995: The statistical connection between tropospheric and stratospheric circulation of the Northern-Hemisphere in winter. *Journal of Climate,* 8: 2281–2295.

Pickart, R. S. and M. A. Spall, 2007: Impact of Labrador Sea convection on the North Atlantic meridional overturning circulation. *Journal of Physical Oceanography*, 37: 2207-2227.

Pielke, R.A., 2002: *Mesoscale Meteorological Modeling*. Academic Press, 2nd Ed., 676pp.

Polyakov, I.V., V.A. Alexeev, U.S. Bhatt, E.I. Polyakova, and X. Zhang, 2009: North Atlantic warming: patterns of long-term trend and multi-decadal variability, *Climate Dynamics*, doi:10.1007/s00382-008-0522-3.

Qian, B., and K. Rasheed, 2007: Stock market prediction with multiple classifiers. *Applied Intelligence*, 26(1): 25–33.

Qiu, B. and R.X. Huang, 1995: Ventilation of the North Atlantic and North Pacific: subduction versus obduction. *Journal of Physical Oceanography,* 25: 2374–2390.

Rahmstorf, S. and A. Ganopolski, 1999: Long-term global warming scenarios computed with an efficient coupled climate model. *Climatic Change,* 43: 353–367.

Rahmstorf, S., 1999: Shifting seas in the greenhouse? *Nature*, 399: 523–524.

Rangarajan, G. and D.A. Sant, 2004: Fractal dimension analysis of Indian climate dynamics. *Chaos, Solitons & Fractals* , 19: 285–291.

Rayner, N.A., P. Brohan, D.E. Parker, C.K. Folland, J.J. Kennedy, M. Vanicek, T. Ansell and S.F.B. Tett, 2006: Improved analyses of changes and uncertainties in marine temperature measured in situ since the mid-nineteenth century: the HadSST2 dataset. *Journal of Climate*, 19, 446-469.

Redfern, R., 2001: *Origins, the Evolution of Continents, Oceans and Life*, University of Oklahoma Press, p. 26.

Rehman, S. and M. El-Gebeily, 2009: A study of Saudi climatic parameters using climatic predictability indices. *Chaos, Solitons Fractals*, 41(3): 1055–1069.

Reverdin, G., D. Cayan, and Y. Kushnir, 1997: Decadal variability of the hydrography in the upper northern North Atlantic in 1948 – 1990. *Journal of Geophysics Research* 102: 8505–8531.

Rodwell, M.J., D.P. Rowell, and C.K. Folland, 1999: Oceanic forcing of the wintertime North Atlantic Oscillation and European climate. *Nature*, 398: 320–323.

Roemmich, D. and C. Wunsch, 1985: Two transatlantic sections: Meridional circulation and Heat flux in the subtropical North Atlantic Ocean. *Deep-Sea Research,* 32: 619-664.

Rogers, J.C., 1984: The association between the North-Atlantic Oscillation and the Southern Oscillation in the Northern Hemisphere. *Monthly Weather Review*, 112: 1999–2015.

Schlesinger, M.E. and N. Ramankutty, 1994: An oscillation in the global climate system of period 65 – 70 years. *Nature,* 376: 723–726.

Schmittner, A., J. C. H. Chiang, and S. Hemming, 2007: Introduction: The ocean's meridional overturning circulation, *Ocean Circulation: Mechanisms and Impacts*, AGU Geophysical Monograph Series, vol. 173, edited by A. Schmittner, J. C. H. Chiang, and S. R. Hemming, American Geophysical Union. pp. 1-4.

Schott, F.A., L. Stramma, B.S., Giese, R. Zantopp, 2009: Labrador Sea convection and subpolar North Atlantic Deep Water export in the SODA assimilation model. *Deep-Sea Research I.* 56: 926-938.

Selten, F.M., R.J. Haarsma, and J.D. Opsteegh, 1999: On the mechanism of North Atlantic decadal variability. *Journal of Climate,* 12: 1956–1973.

Spall, M.A., 1996: Dynamics of the Gulf Stream/Deep Western Boundary Current crossover. Part II: low frequency internal oscillations. *Journal of Physical Oceanography*, 10: 2170–2182.

Stommel, H., 1979: Determination of water-mass properties of water pumped dowm from the Ekman layer to the geostrophic flow below. *Proceedings of the National Academy of Science US,* 76: 3051–3055.

Sutton, R.T. and M.R. Allen, 1997: Decadal predictability of North Atlantic sea surface temperature and climate. *Nature*, 388: 563–567.

Sutton, R.T. and D.L.R. Hodson, 2003: Influence of the ocean on North Atlantic climate variability 1871-1999. *Journal of Climate*, 16: 3296-3313.

Thompson, D.W.J and J.M. Wallace, 1998: The Arctic Oscillation signature in the wintertime geopotential height and temperature fields. *Geophysical Research Letters,* 25: 1297–1300.

Timmerman, A., M. Latif, R. Voss, and A. Grotzner, 1998: Northern Hemispheric Interdecadal Variability: a coupled air-sea mode*. Journal of Climate,* 11: 1906–1931.

Tomczak, M. and J. S. Godfrey, 2003: *Regional Oceanography: an introduction.* Online book. 2nd Ed. 390 pp. http://www.es.flinders.edu.au/~mattom/regoc/pdfversion.html.

Trenberth, K.E., 1997: The Definition of El Nino. *Bulletin of the American Meteorological Society,* 78: 2771-2777.

Trenberth, K.E., G.W. Branstator, D. Karoly, A. Kumar, N.-C. Lau, and C. Ropelewski, 1998: Progress during TOGA in understanding and modeling global teleconnections associated with tropical sea surface temperature. *Journal of Geophysical Research*, 103(C7): 14291-14324.

van Aken, H. M., 2007: The oceanic thermohaline circulation: An introduction, New York, Springer, 326 pp.

Walker, G. T., 1924: Correlation in seasonal variations of weather. IX. A further study of world weather. *Memoirs of the Indian Meteorological Department* 24 (Part 9) 275–332.

Wallace, J.M., 1996: *Observed climatic variability: spatial structure. In Decadal Climate Variability*, Anderson, D.L.T. and J. Willebrand (eds). Springer: Berlin, 31–81.

Wallace, J.M. and D.S. Gutzler, 1981: Teleconnections in the geopotential height field during the Northern Hemisphere winter. *Monthly Weather Reviews,* 109: 784–812.

Wanner, H., S. Brönnimann, C. Casty, D. Gyalistras, J. Luterbacher, C. Schmutz, D.B. Stephenson, and E. Xoplaki, 2001: North Atlantic Oscillation – Concepts and studies. *Surveys in Geophysics,* 22: *321–382*.

Watanabe, M. and M. Kimoto, 2000: On the persistence of decadal SST anomalies in the North Atlantic*. Journal of Climate,* 13: 3017–3028.

Weng, W. and J.D. Neelin, 1998: On the role of ocean – atmosphere interaction in middle-latitude interdecadal variability. *Geophysical Research Letters,* 25: 167–170.

Wunsch, C. and D. Roemmich, 1985: Is the North Atlantic in Sverdrup balance? *Journal of Physical Oceanography,* 15: 1876-1880.

Yelland, M. J., and P. K. Taylor, 1996: Wind stress measurements from the open ocean. *J. Phys. Oceanogr.,* **26,** 541–558. termination. *Journal of Atmospheric and Oceanic Technology,* 11: 1093–1108.

Appendix A. Box model stability tests

Before utilizing the work of Marshall et al. (2001) as the foundation of the box model for this study, it was imperative to verify the quality of the model. In order to do so, numerical solutions were first generated, and then analytical solutions were derived and compared to the numerical solutions for agreement. This was completed by first selecting a subset of individual terms from the complete model to test accuracies of numerical solutions, and then the system was solved by incorporating the combined terms as explained in Marshall et al. (2001b) with the exception of stochastic forcing. The stochastic forcing component was excluded from this initial analysis due to its complex nature, and but was incorporated into the final box model as described in Section 3.2.

The non-dimensional box model proposed by Marshall et al. (2001b) is explained in Section 3.1, followed by a description of the initial conditions and numerical methods (Section 3.3) utilized in solving the model equations. The numerical scheme utilized for approximating derivatives is described along with any assumptions made, followed by a derivation of the analytical solutions. Then the numerical and analytical solutions are compared and the results are discussed to address the individual accuracies. The analysis is continued in section (A1.4d) by incorporating the combined components as explained in Marshall et al. (2001b) with the exception of stochastic forcing. The conclusions from the comparisons are summarized in section (A1.5).

In the stability experiments carried out in this appendix the model was initialized with an ocean temperature perturbation, T_o = 2°C, as was discussed in Section 3.1. Initial MOC, Ψ_{mo}, and gyre, Ψ_{go}, streamfunctions were initialized with values of $\Psi_{mo} = \Psi_{go} = 0$ Sv, providing the opportunity to observe how ocean temperature anomalies alone would affect the model behavior. Initial conditions (IC) utilized in individual model experiments are provided in Table A.1, and are organized by experiment name, ocean temperature IC, and streamfunction IC.

The equations describing these temperature anomalies and time derivatives were derived from Eqs. (3.1 - 3.4). Model equations were simplified to only include associated terms for each separate experiment. For example, during the "MOC" experiment, Eq. (3.1) was simplified to examine ocean temperature anomalies associated with the model MOC component alone:

$$\frac{\partial T}{\partial t} = m\Psi_m . \qquad \text{(A.1)}$$

Using the model IC described above, yields:

$$T\big|_{t=0} = T_o = 2, \qquad \text{(A.2)}$$

and $$\Psi_m\big|_{t=0} = \Psi_{mo} = 0. \qquad \text{(A.3)}$$

Therefore, at t = 0, the ocean temperature time derivative would be explained by:

$$\left.\frac{\partial T}{\partial t}\right|_{t=0} = m\Psi_{mo} = m \cdot 0 = 0 . \qquad \text{(A.4)}$$

Time derivatives and anomalies for ocean temperature and associated steamfunctions utilized for each test experiment can be found similarly and are listed by experiment in Table A.1.

Table A.1 Initial conditions (IC) used in model experiments. T_o is the IC for water temperature anomalies, Ψ_{mo} is the IC for MOC streamfunction anomalies, and Ψ_{go} is the IC for Gyre steamfunction anomalies.

Model Experiments	Temperature anomalies and time derivatives	Streamfunction anomalies and time derivatives
"MOC"	$T\big\|_{t=o} = T_o = 2$ $\left.\frac{\partial T}{\partial t}\right\|_{t=o} = 0$	$\Psi_m\big\|_{t=o} = \Psi_{mo} = 0$ $\left.\frac{\partial \Psi_m}{\partial t}\right\|_{t=o} = -2s$
"Gyre"	$T\big\|_{t=o} = T_o = 2$ $\left.\frac{\partial T}{\partial t}\right\|_{t=o} = 0$	$\Psi_g\big\|_{t=o} = \Psi_{go} = 0$ $\left.\frac{\partial \Psi_g}{\partial t}\right\|_{t=o} = -2f$
"Ekman"	$T\big\|_{t=o} = T_o = 2$ $\left.\frac{\partial T}{\partial t}\right\|_{t=o} = -2\lambda$	-
"MOC + Gyre + Ekman"	$T\big\|_{t=o} = T_o = 2$ $\left.\frac{\partial T}{\partial t}\right\|_{t=o} = -2\lambda$	-

The resulting simulated variables for each experiment listed in Table A.1 were dimensionalized using the scaling factors (Table 3.1) and the numerical solutions were plotted against the corresponding analytical solutions. The model solutions and the agreement between the numerical and analytical solutions were generated in order to examine stability of the numerical solutions. Figure A.1 displays an example of stable and unstable model solutions for the first 20 years of this test.

The top panel shows an ideal case that incorporated the Euler-Forward scheme every 10th time step and the CFL criteria determined timestep of 0.0013 yr (~0.47 days). The results show a stable solution with no numerical modes generated. The second panel from the top displays the impacts of using a timestep larger than the CFL criteria determined value when running the model, as well as the benefits of incorporating the Euler-Forward scheme. In this case, a timestep of 0.1 yr (~36.5 days) was utilized and as a result, derivative estimates were not as accurate and the model agreement displays a small computational mode through the timeseries. In addition, a computational mode also appeared in the solution until removed with the Euler-Forward scheme at the 10th timestep (1 year). The incorporation of the forward differencing scheme smoothes the solution and prevents the propagation of the computational mode in the calculated solution.

The third and fourth panels of Figure A2 display the importance of timestep alone, without the incorporation of the Euler-Forward scheme. Both cases show the generation of computational modes, however it is apparent that the modes are amplified in the later case where the timestep is much larger at 0.1 yr (~36.5 days). As a result of these tests, it was determined that the central differences scheme would be utilized for the model experiments. The experiments are set to incorporate the Euler-Forward scheme every 10th time step, and the timestep is set at Δt = 0.0013 yr (~0.47 days), in order to suppress artificial computational modes generated by the central difference scheme.

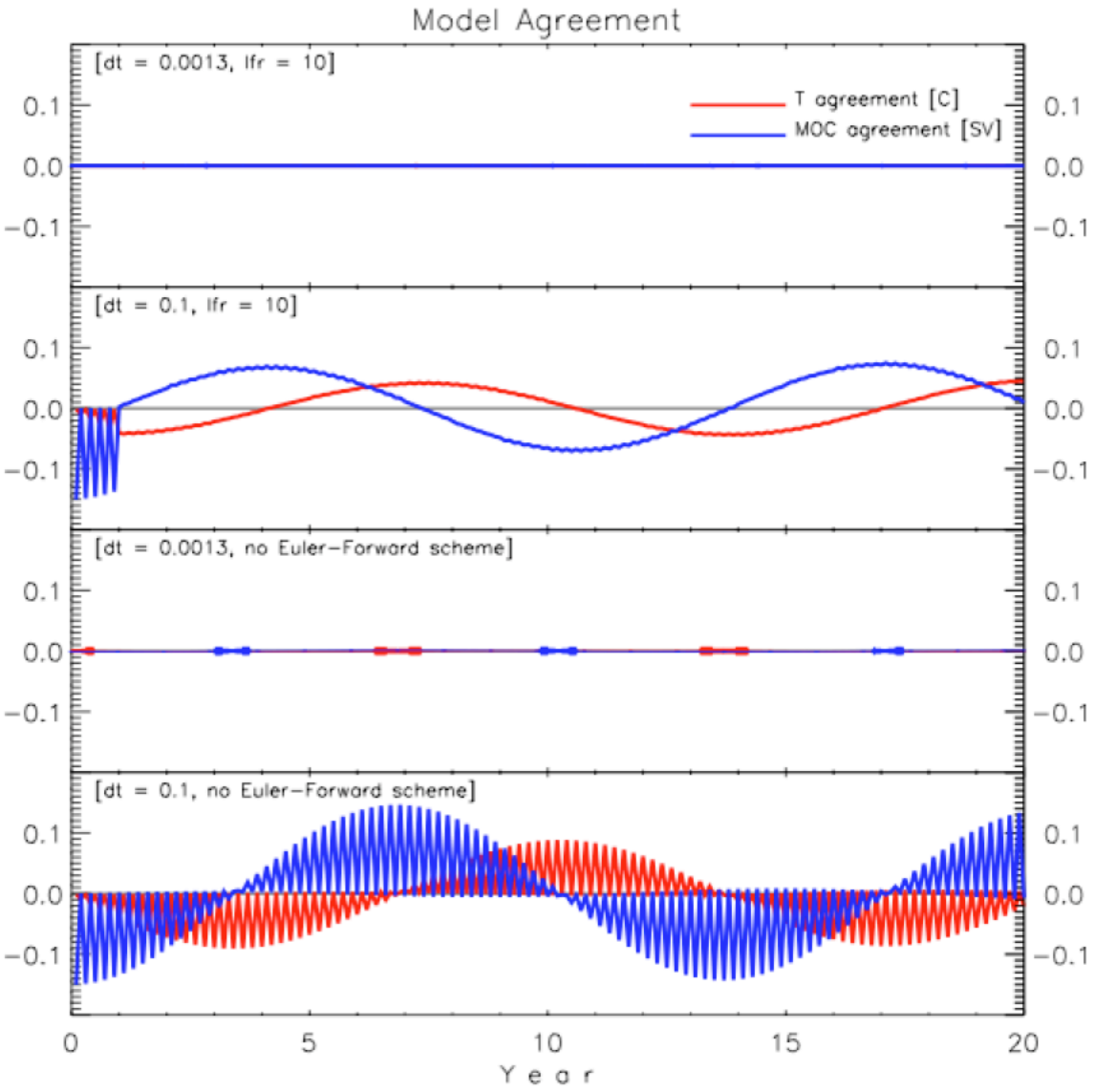

Figure A.1 Agreement of model solutions (numerical - analytical solutions) displaying impacts of different timesteps and incorporation of Euler-Forward scheme in central difference scheme. From top to bottom, (1) CFL criteria timestep and incorporation of Euler-Forward Scheme every 10 timesteps, (2) timestep greater than CFL criteria and incorporation of Euler-Forward every 10 timesteps, (3) CFL criteria timestep without Euler-Forward scheme, (4) timestep violating CFL criteria without Euler-Forward scheme.

The quality of numerical model solutions were evaluated by comparing them with analytical solutions for the test experiments presented in Table A.1. In the following subsections, the equations used for the model test are first described, followed by a derivation of the analytical model solutions. The resulting solutions are then plotted and discussed.

A.1 Numerical and analytical solutions for "MOC" experiment

The objective of this subsection is to examine and test the quality of the numerical solution of the part of the model, which describes temperature perturbations due to the MOC change alone. This may be described as the following subset of equations derived from Eqs. (3.1–3.4).

$$\frac{\partial T}{\partial t} = m\Psi_m, \tag{A.5}$$

$$\frac{\partial \Psi_m}{\partial t} = -sT. \tag{A.6}$$

Corresponding IC from Table A.1 complemented these equations. The subset of equations, (A.5 - A.6), was first solved numerically, and the solutions for T and Ψ_m are shown in Figure A.2.

The analytical solution for the ocean temperature anomalies, *T*, is obtained from Eqs. (A.5 – A6). Assuming that *m* and *s* are independent of time, taking the derivative of each of these equations with respect to time, *t*, and substituting the second equation into the first one yields:

$$\frac{\partial^2 T}{\partial t^2} + msT = 0. \tag{A.7}$$

The general solution of this simple differential equation is:

$$T(t) = C_1 cos(\omega t) + C_2 sin(\omega t), \tag{A.8}$$

where, $\omega_o = \sqrt{ms}$ and $\omega = \frac{\omega_o}{t_{delay}}$.

Taking into account initial conditions (Table A.1) and the temperature scale, *Y*, yields:

$$T(t) = 2Y\cos(\omega t). \qquad \text{(A.9)}$$

The analytical solution for the MOC anomalies may be found similarly, dimensionalized by the Ψ_M scale to yield:

$$\Psi_m(t) = \Psi_M \frac{-2s}{\omega}\sin(\omega t). \qquad \text{(A.10)}$$

The analytical solutions for the MOC and water temperature anomalies are displayed alongside the numerical solutions in Figure A.2.

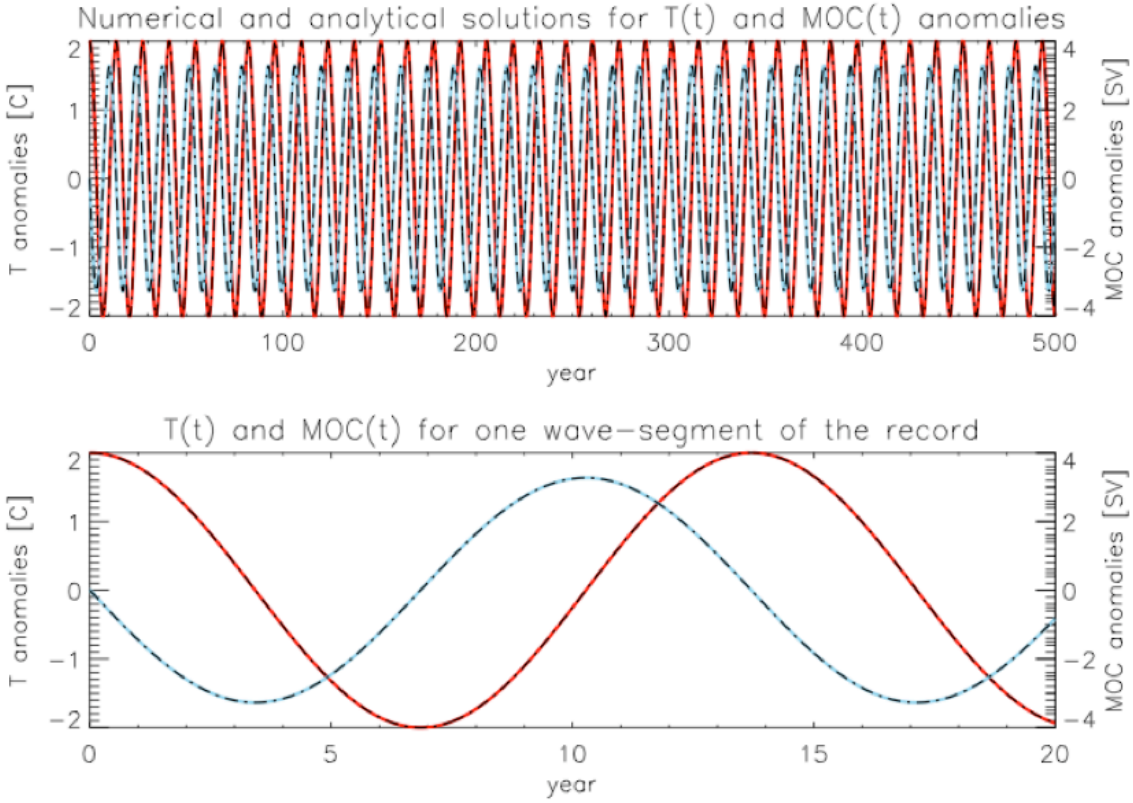

Figure A.2 Numerical and analytical solutions for the ocean temperature anomaly (red) response to MOC change only (blue) for "MOC" experiment. The numerical solutions are shown by solid lines, and the analytical solutions are shown by black-dashed lines. The top panel displays results for entire time period of 500 years, while bottom panel displays a segment at the time interval containing one wave only.

The analytical and numerical solutions are in excellent agreement, resulting in high confidence of the quality of the model's finite difference scheme approximating time derivative. There is also a clear pattern with the ocean temperature anomalies lagging the MOC anomalies. This implies that the ocean temperature anomalies respond to MOC changes, and indicates the importance of the MOC component in the overall model. The time delay between the MOC and ocean temperature anomaly signals (bottom panel of Fig. A.1) is approximately 3.5 years. It should be noted, however, that this model is fairly simple in regards to all forces actually occurring in the North Atlantic Ocean basin. The results of this model experiment therefore should only be looked at as just a test experiment.

A.2 Numerical and analytical solutions for "Gyre" experiment

The objective of this experiment is to examine and test the quality of the numerical solution of the part of the model, which describes temperature perturbations due to the ocean gyre changes alone. This may be described as the following subset of equations derived from Eqs. 3.1–3.4:

$$\frac{\partial T}{\partial t} = g\Psi_g \qquad \text{(A.11)}$$

$$\frac{\partial \Psi_g}{\partial t} = \tau \qquad \text{(A.12)}$$

$$\tau = -fT. \qquad \text{(A.13)}$$

For this analysis, we simplified the original system (3.1-3.4) even further by omitting the spatial derivative of Ψ_g, and integrated the streamfunction with respect to time alone. Corresponding IC from Table A.1 complemented Eq. (A.11-A.13), which were first solved numerically, and the solutions for T and Ψ_g are shown in Figure A.3.

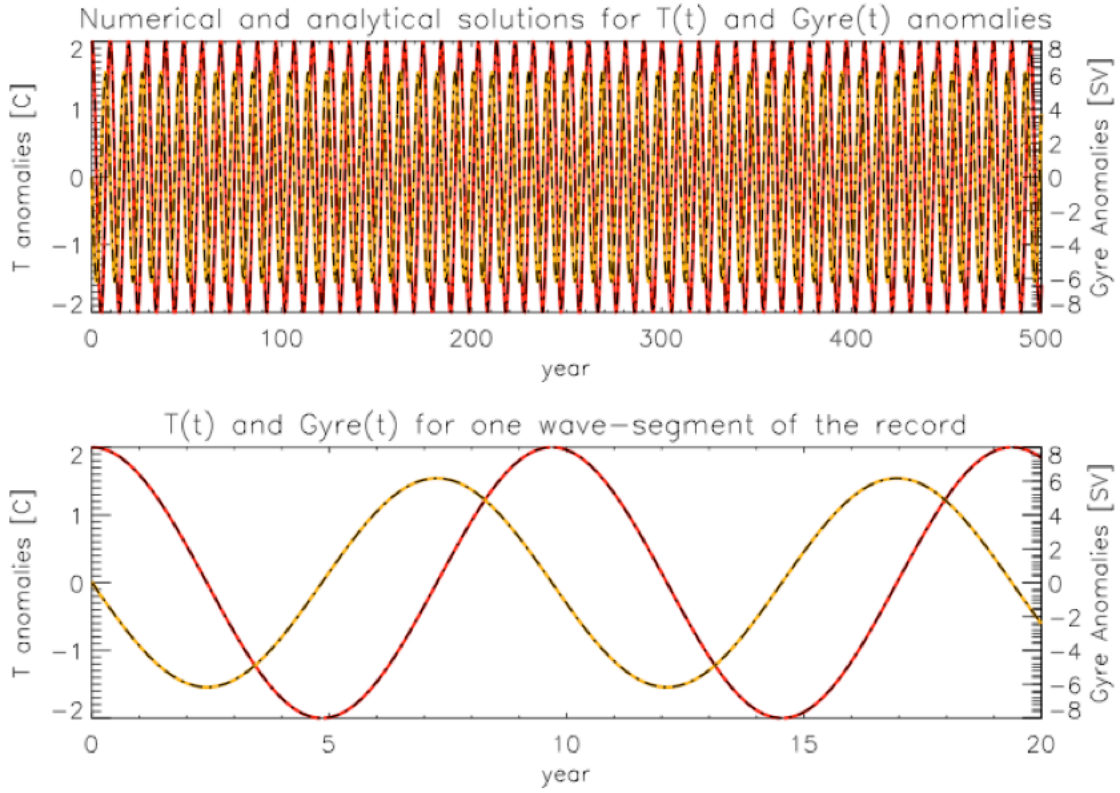

Figure A.3 Numerical (solid color) and analytical (dashed black) solutions for the ocean temperature anomaly (red) response to gyre change (yellow) only for "Gyre" experiment. The top panel displays results for entire time period of 500 years, while bottom panel displays a look at the time interval containing one wave only.

The analytical solution for the ocean temperature anomalies, *T*, is obtained from Eqs. (A.11 – A.13). Similar to experiment "MOC", analytical solutions for *T* and Ψ_g were derived:

$$T(t) = 2Y\cos(\omega t) \qquad \text{(A.14)}$$

$$\Psi_g(t) = \Psi_G\left(\frac{-2f}{\omega_o}\right)\sin(\omega t) \qquad \text{(A.15)}$$

where, $\omega_o = \sqrt{ms}$ and $\omega = \dfrac{\omega_o}{t_{delay}}$.

The analytical solutions for the gyre and water temperature anomalies are displayed alongside the numerical solutions in Figure A.3, and coincide quite well.

Minimal differences between the numerical and analytical solutions strengthen the confidence in the quality of the central differencing scheme incorporated into the numerical model solution. Aside from the agreement in solutions there is also a clear time-lag signature in the dataset with the ocean temperature anomaly lagging behind the gyre anomaly by approximately 2.5 years, which is one year faster than the response to MOC changes. This lag may be explained by the ratio of two non-dimensional factors used in the "Gyre" and "MOC" experiments. The non-dimensional factor, g, describing the efficiency of heat transport by ocean gyres is about half of the corresponding non-dimensional factor, *m*, describing the heat transport by MOC. The response time is determined by the non-dimensional factors coinciding with the streamfunctions for each experiment. In the case of the "MOC" experiment the streamfunction is multiplied by the solenoidal factor of 0.2, while in the "Gyre" experiment the streamfunction is multiplied by the feedback of ocean temperature anomalies on wind stress of 0.8. The larger non-dimensional factor for the "Gyre" experiment indicates that it has a greater impact on the ocean surface temperature anomalies, and as a result the time lag is shorter than that of the "MOC" experiment. Due to this lag response it may be implied that the gyre component plays an important role in the overall response of the surface ocean temperature.

A.3 Numerical and analytical solutions for "Ekman" experiment

The goal of this sub-section is to investigate the quality of the numerical solution of the part of the model describing the impacts of wind and Ekman components alone on mixed-ocean layer temperatures. This may be described by the following:

$$\frac{\partial T}{\partial t} = -\lambda T \qquad \text{(A.16)}$$

Corresponding IC from Table A.1 complemented this equation, and λ was obtained from Table 3.2. Equation A.16 was first solved numerically with IC, and the solution for T and wind-Ekman component are shown in Figure A.4.

The analytical solution for the ocean temperature anomalies, *T*, is obtained from Eq. (A.16). The general solution of this simple differential equation is:

$$T(t) = C_1 e^{-\lambda t} + C_2 e^{\lambda t}. \qquad \text{(A.17)}$$

Taking into account initial conditions (Table A.1) and the temperature scale, *Y*, yields:

$$T(t) = 2 \cdot Y \cdot e^{\frac{-\lambda t}{t_{delay}}}. \qquad \text{(A.18)}$$

The analytical solutions for the water temperature anomalies are displayed alongside the numerical solutions in Figure A.4.

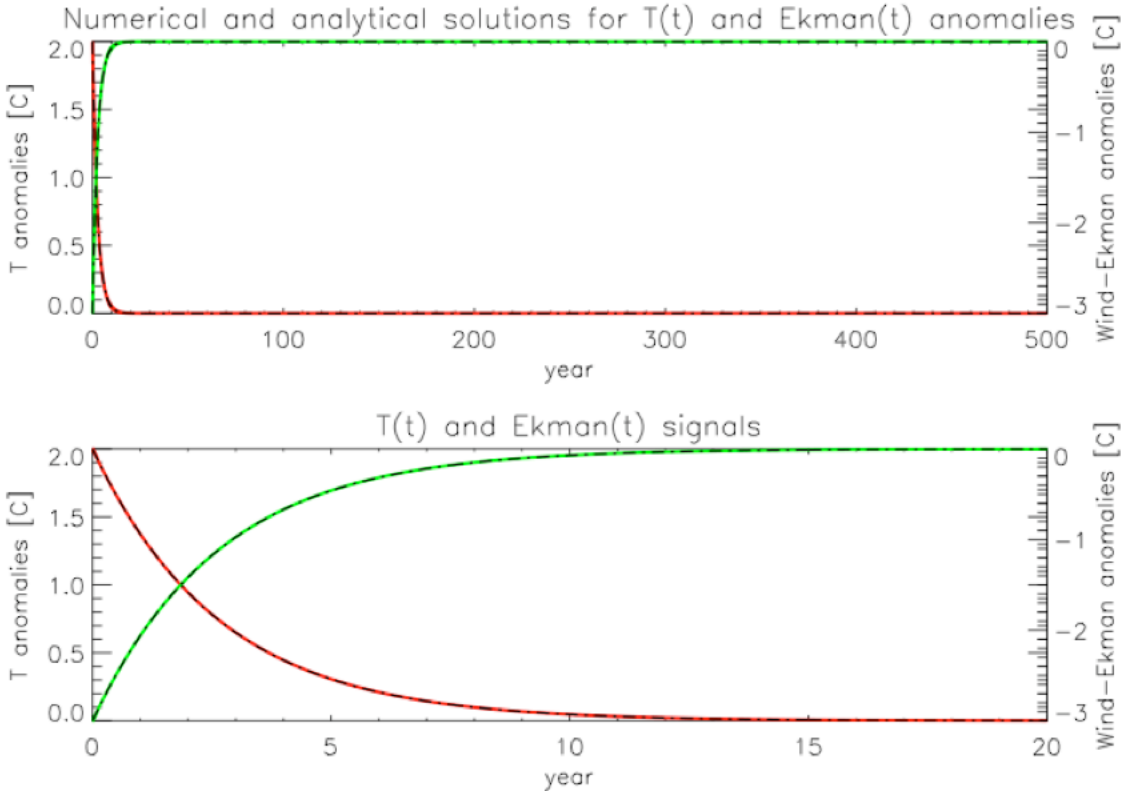

Figure A.4 Numerical (red) and analytical (black dashed) solutions for the ocean temperature anomaly response to "Ekman" experiment forcing. The top panel displays results for entire time period of 500 years, while bottom panel displays a segment of response during the first 20 years.

Once again we see that the numerical solution for this experiment agrees quite well with the numerical solution generated through the central differencing scheme. In this experiment we also see a different response to the forcing by the wind. Instead of a wave signature as in the previous two experiments, we see a damping of the ocean surface temperature anomaly by the wind forcing as an exponential decay. Based on this small experiment singling out the wind component it may be inferred that the wind-Ekman forcing should act to dampen the overall signature of the ocean surface temperature anomalies when combined together in the model.

A.4 Numerical and analytical solutions for combined forcings

The goal of this sub-section is to investigate the quality of the numerical solution of the experimental model describing the combined effects of the "MOC", "Gyre", and "Ekman" experiments.

$$\frac{\partial T}{\partial t} = m\Psi_m + g\Psi_g - \lambda T \qquad \text{(A.19)}$$

Following the same procedures used in the previous experiments, Eq. A.19 was solved numerically with IC and Figure A.5 displays the corresponding numerical solution.

The analytical solution for the ocean temperature anomalies, *T*, is obtained from Eq. A.19. Taking the derivative with respect to time, *t*, and substituting in the streamfunction partial time derivatives as in the previous experiments yields:

$$\frac{\partial^2 T}{\partial t^2} = m\frac{\partial \Psi_m}{\partial t} + g\frac{\partial \Psi_g}{\partial t} - \frac{\partial T}{\partial t}. \qquad \text{(A.20)}$$

Now simplifying Eq. A.17 we obtain:

$$\frac{\partial^2 T}{\partial t^2} + \lambda\frac{\partial T}{\partial t} + \alpha T = 0, \qquad \text{(A.21)}$$

where $\alpha = ms + gf$. The general solution of this simple differential equation is:

$$T(t) = e^{\alpha t}\left[C_1 \cos\beta t + C_2 \sin\beta t\right] \qquad \text{(A.22)}$$

Taking into account initial conditions (Table A.1) and the parameter scales yields:

$$T(t) = e^{-.75t}\left[2\cos(3.09t) - 0.1877\sin(3.09t)\right] \qquad \text{(A.23)}$$

The analytical solutions for the water temperature anomalies are displayed in black in Figure A.5 along with the numerical solutions.

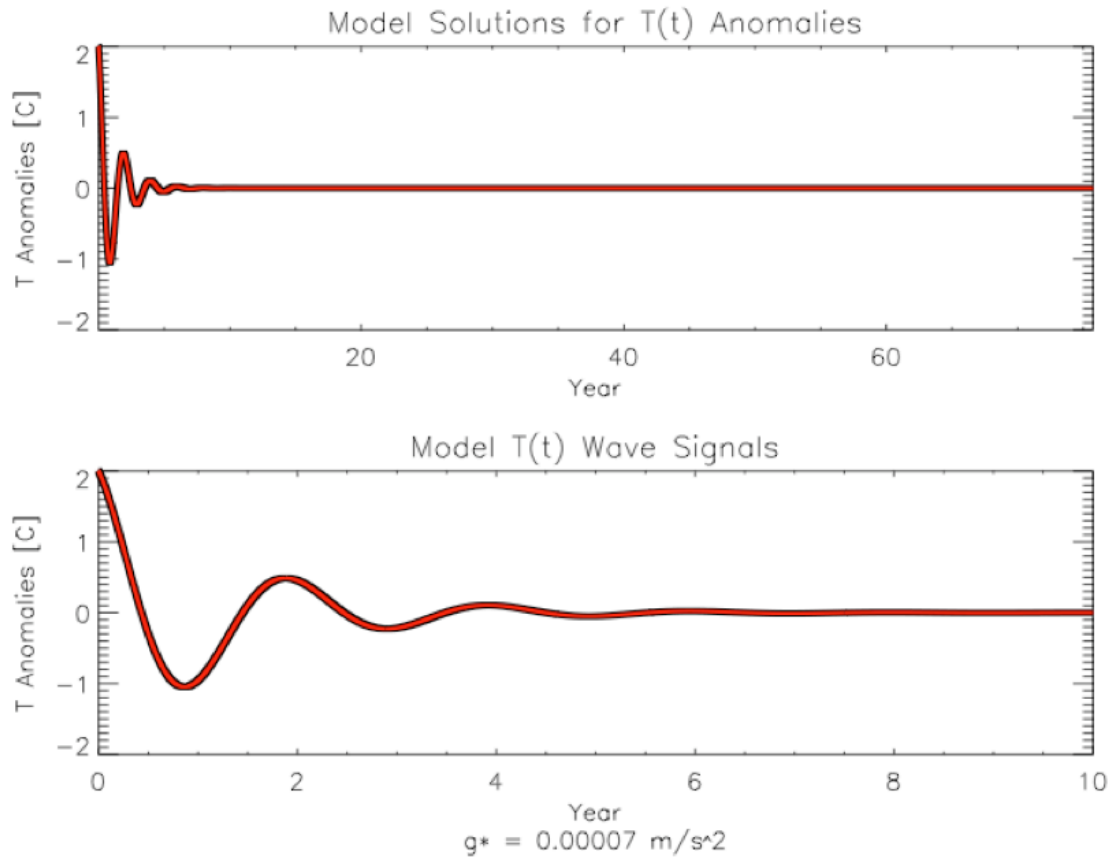

Figure A.5 Numerical (red) and analytical (black dashed) solutions for the ocean temperature anomaly response to combined effects of "MOC", "Gyre", and "Ekman" experiments. The top panel displays results for entire time period of 500 years, while bottom panel displays a segment during the first 20 years.

Appendix B. Wind experiment

This appendix provides the comprehensive set of figures associated with the Wind Experiment for completeness. Figures B.1 and B.2 provide an overview of the observed and synthetic daily Ekman pumping timeseries utilized in forcing the wind streamfunction component of the box model. The entire set of Wind Experiment model results based on the methods described in Chapter 3 of the thesis are also included. Synthetic model results are first presented in order of increasing model forcing complexity (Figures B.3 - B.5), followed by white noise forcing results (Figures B.6 - B.8) with results displayed on the same scales. Spectra analysis comparing synthetic and white noise forcings and their resulting temperature, MOC, and gyre anomalies are also included for each experiment (Figures B.9 - B.15).

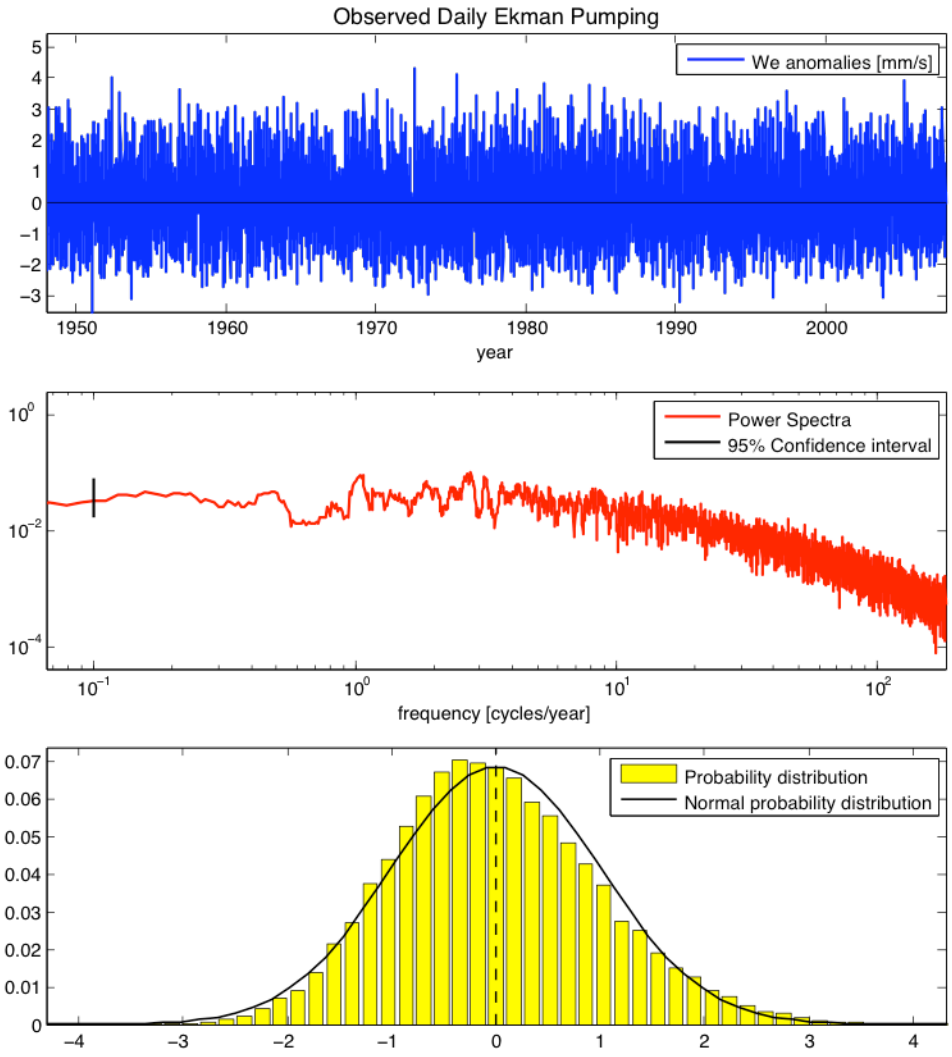

Figure B.1 Analysis of the observed daily Ekman Pumping dataset. (Top) Ekman pumping anomalies (mm/s) over the study region from the NCEP Reanalysis winds at 10m height, (middle) power spectra of displayed anomalies 95% confidence interval (vertical black bar), and (bottom) probability distribution of the displayed anomalies with the normal probability distribution (black bell curve).

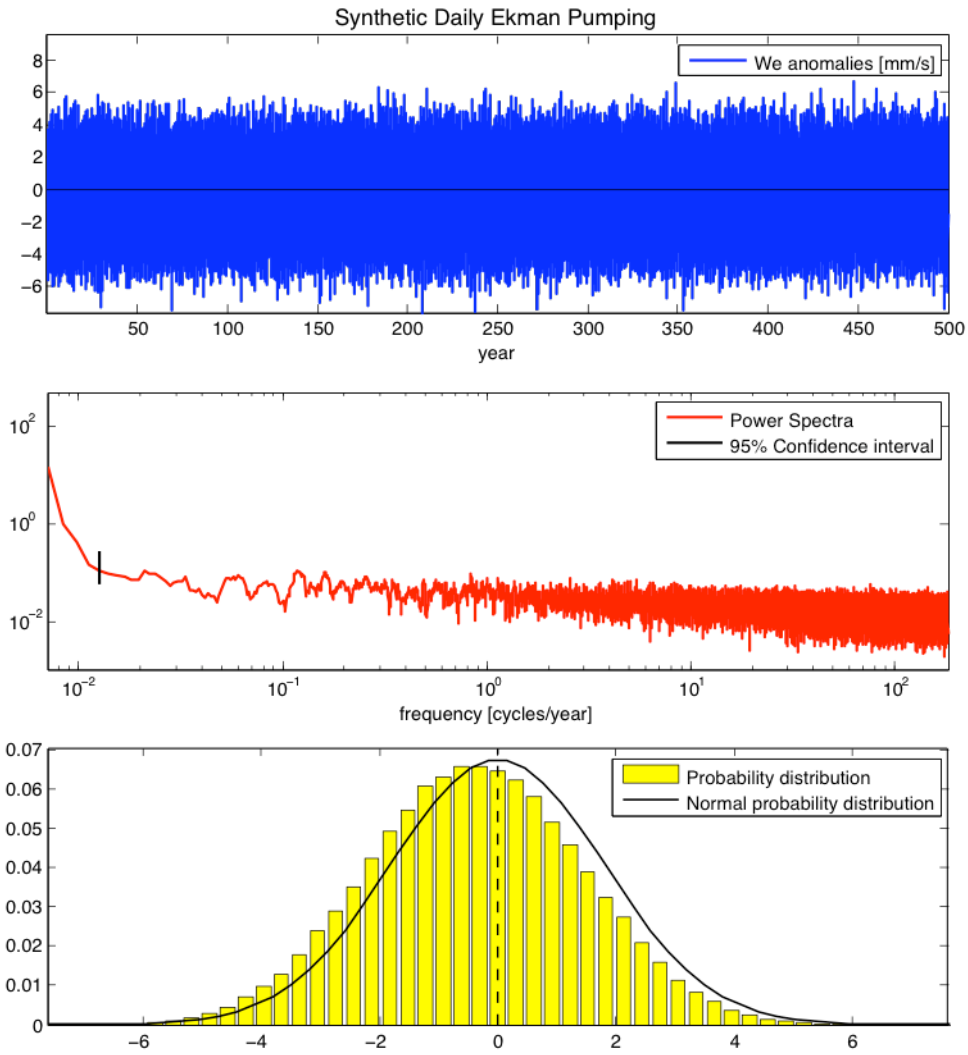

Figure B.2 Analysis of synthetic daily Ekman Pumping dataset. (Top) synthetic daily Ekman Pumping anomalies (mm/s) generated with a Hurst Exponent value of 0.6, and the middle and bottom panels displayed similarly to Figure B.1.

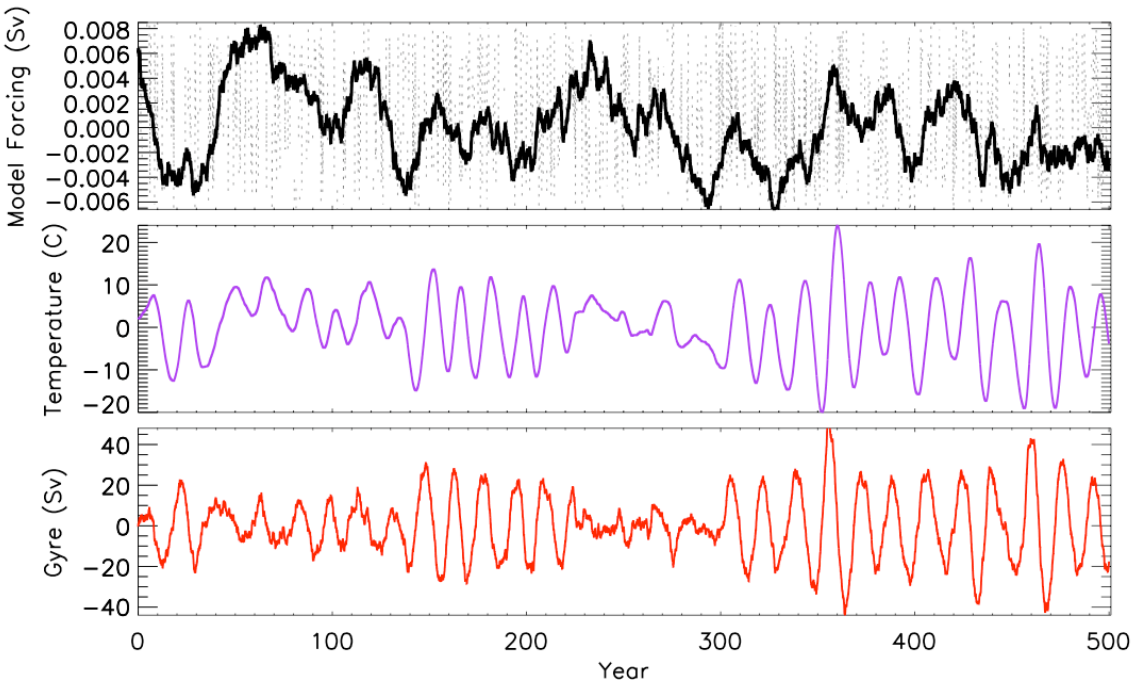

Figure B.3 Results of a 500-year model run for the synthetically forced Wind Experiment W1. (Top) synthetic daily (dashed line) and 7 year running mean (solid line) wind forcing (Sv), (middle) simulated response of SST anomalies (°C), and (bottom) simulated response of horizontal gyre anomalies (Sv).

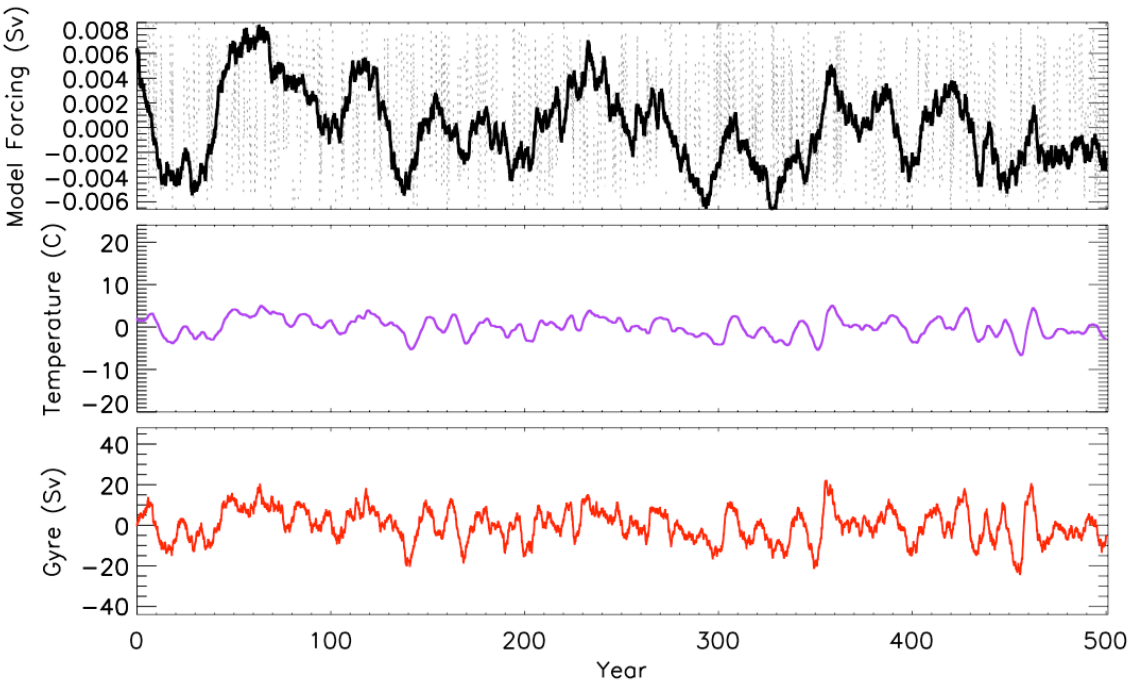

Figure B.4 Model results for the synthetically forced Wind Experiment W2. Figure panels are displayed as in Figure B.3.

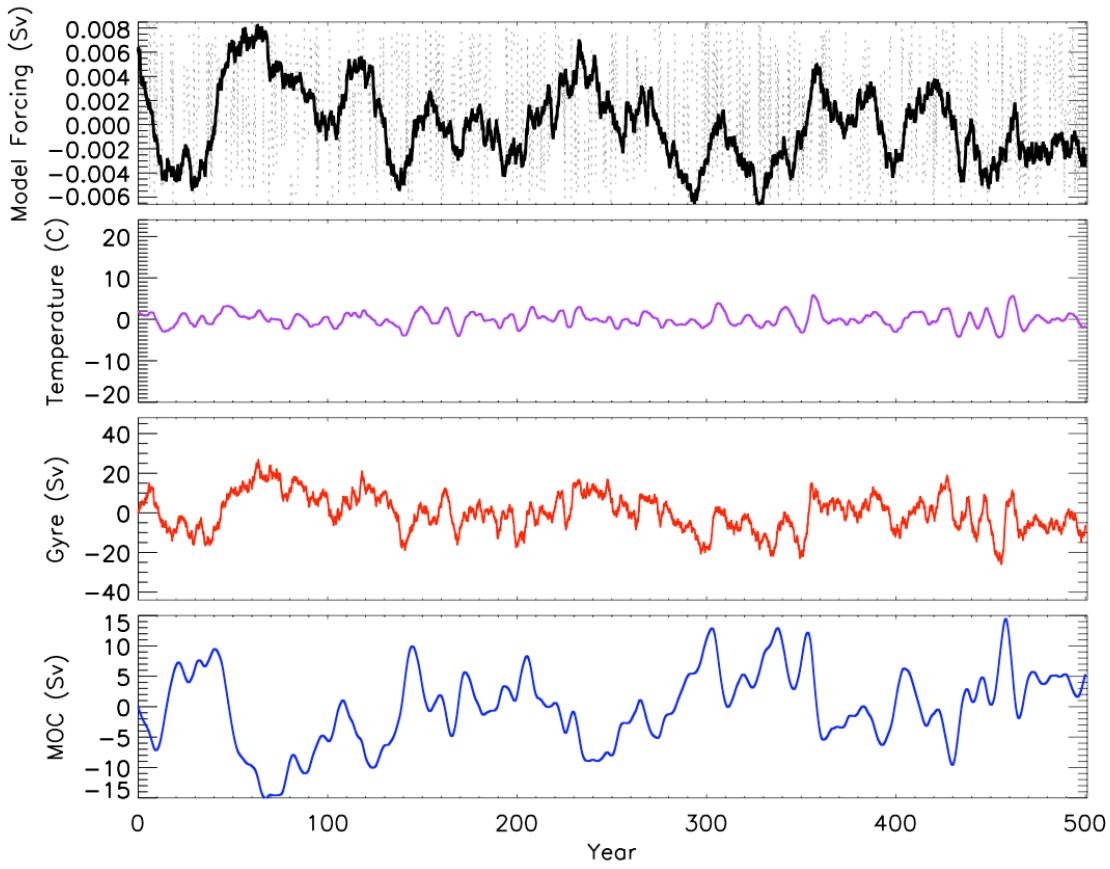

Figure B.5 Model results for the synthetically forced Wind Experiment W3. Figure panels are displayed as in Figure B.3, with the final panel displaying the simulated response of MOC anomalies (Sv).

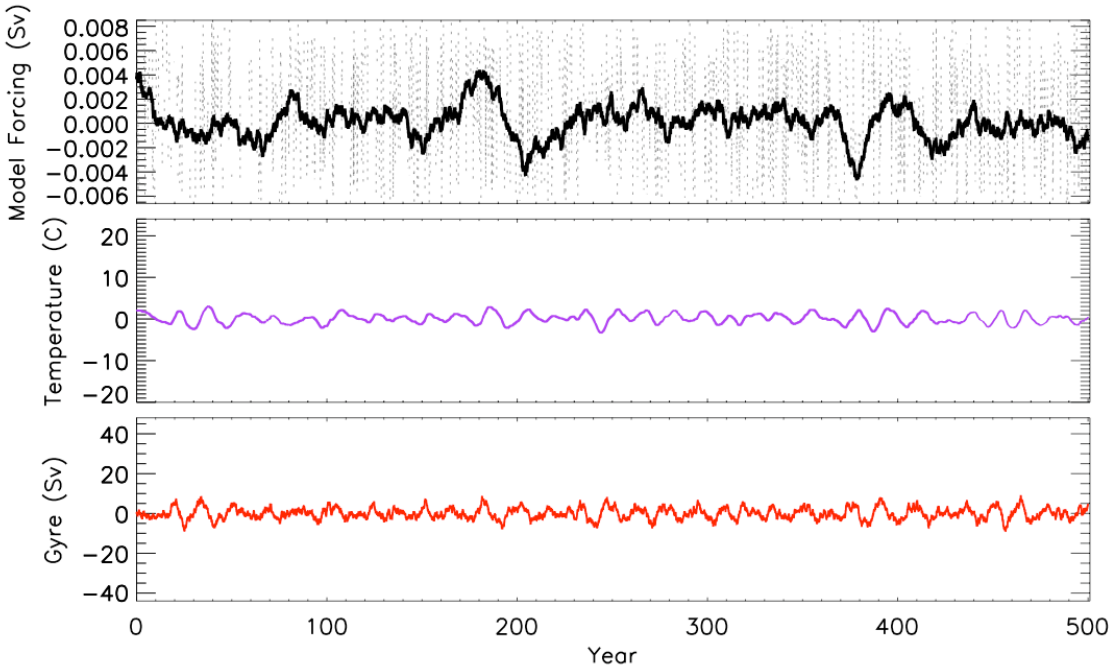

Figure B.6 Model results for the white noise forced Wind Experiment WW1. Figure panels are displayed as in Figure B.3.

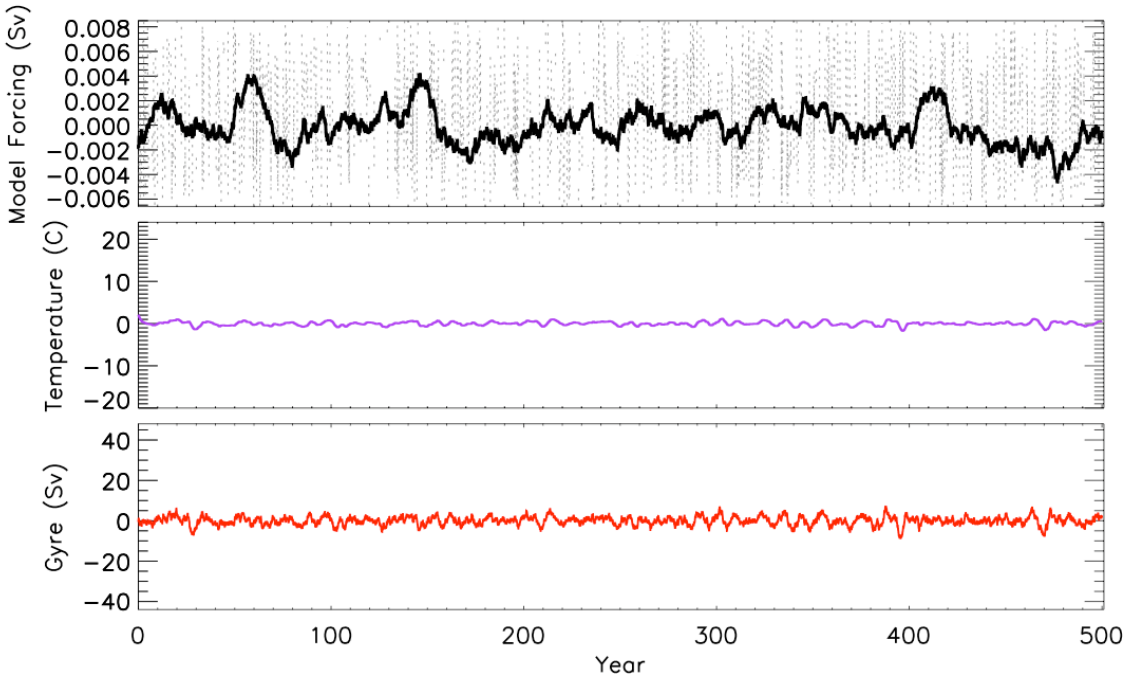

Figure B.7 Model results for the white noise forced Wind Experiment WW2. Figure panels are displayed as in Figure B.3.

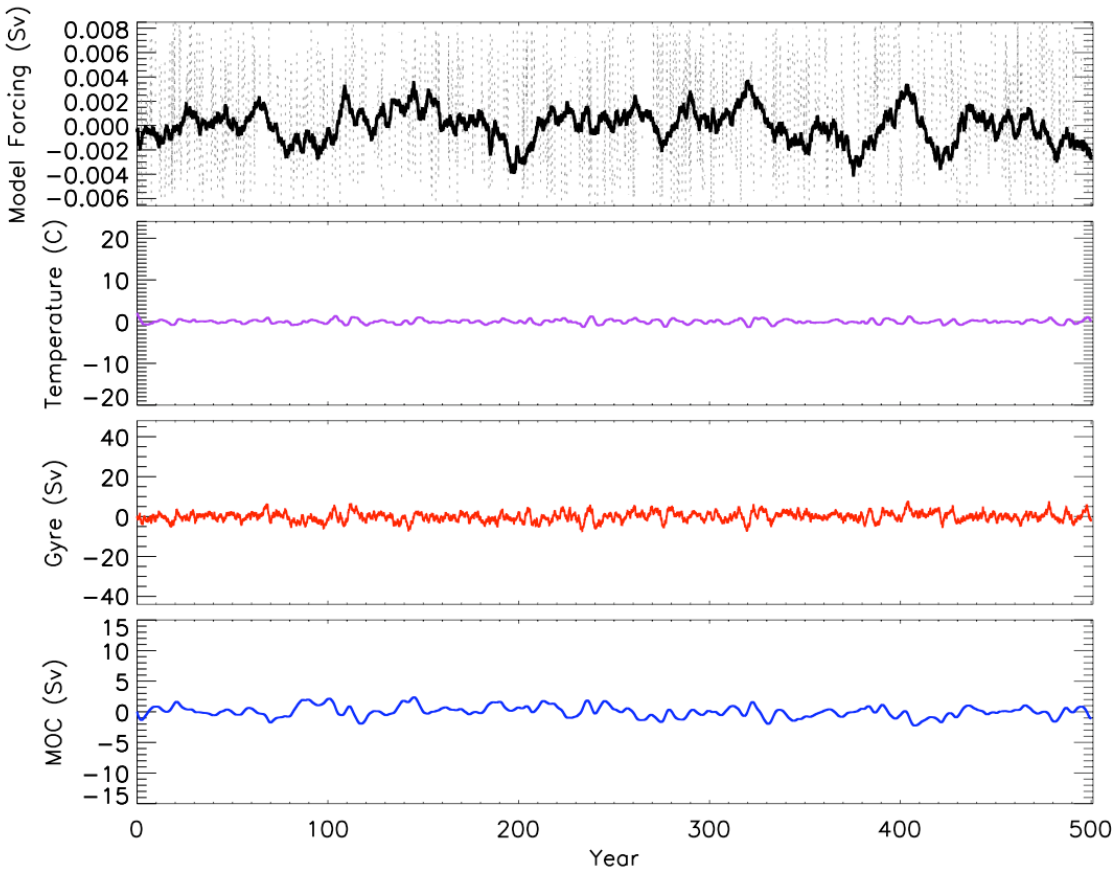

Figure B.8 Model results for the white noise forced Wind Experiment WW3. Figure panels are displayed as in Figure B.5.

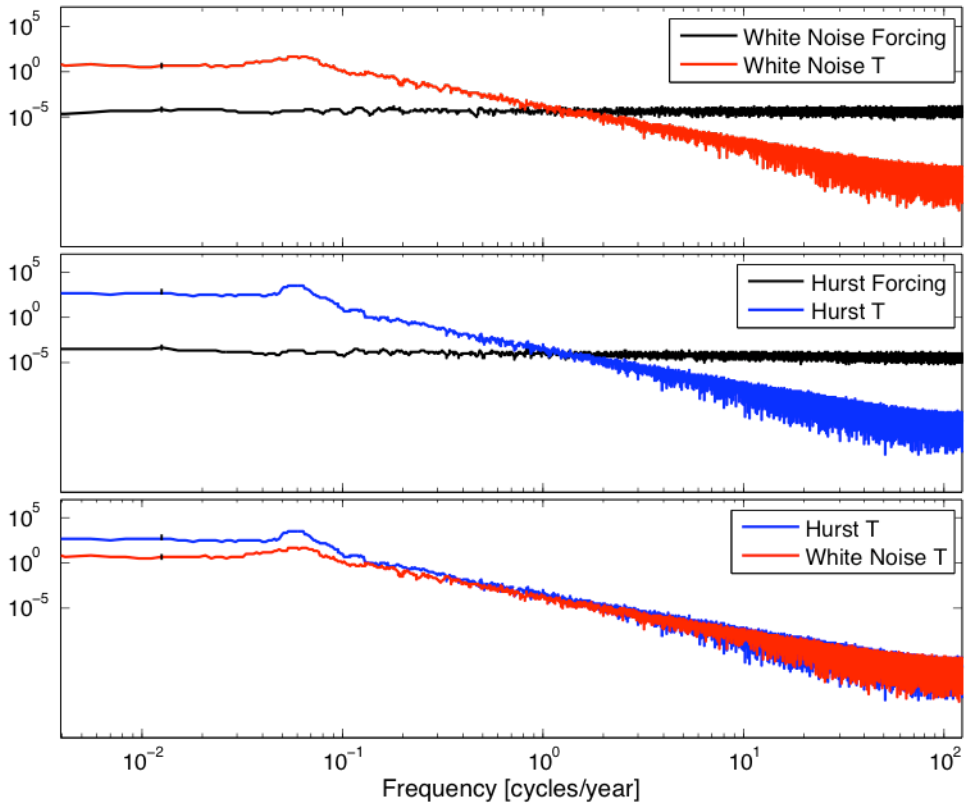

Figure B.9 Power spectra of the timeseries derived from synthetic (W1) and white noise (WW1) wind experiments. (Top) WW1 (white noise) wind forcing and SST spectra, (middle) W1 (synthetic) wind forcing and SST spectra, and (bottom) comparison of spectra for WW1 and W1 SST responses.

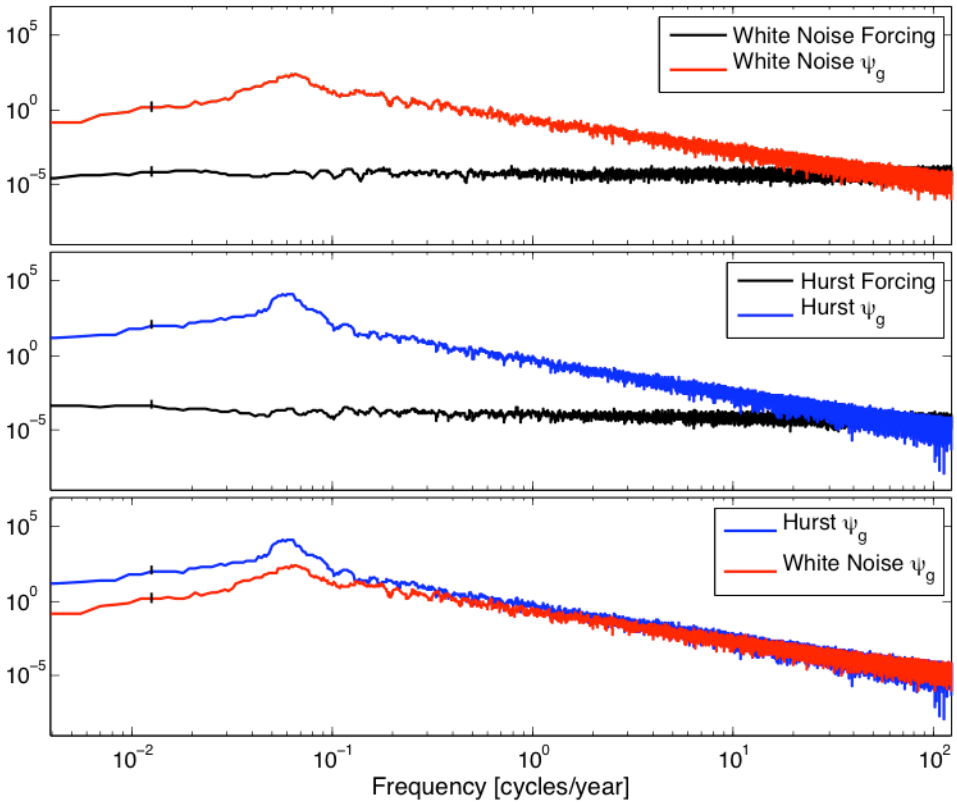

Figure B.10 Power spectra of the timeseries derived from synthetic (W1) and white noise (WW1) wind experiments, with panels displayed similarly to Figure B.9 with resulting horizontal gyre anomaly spectra.

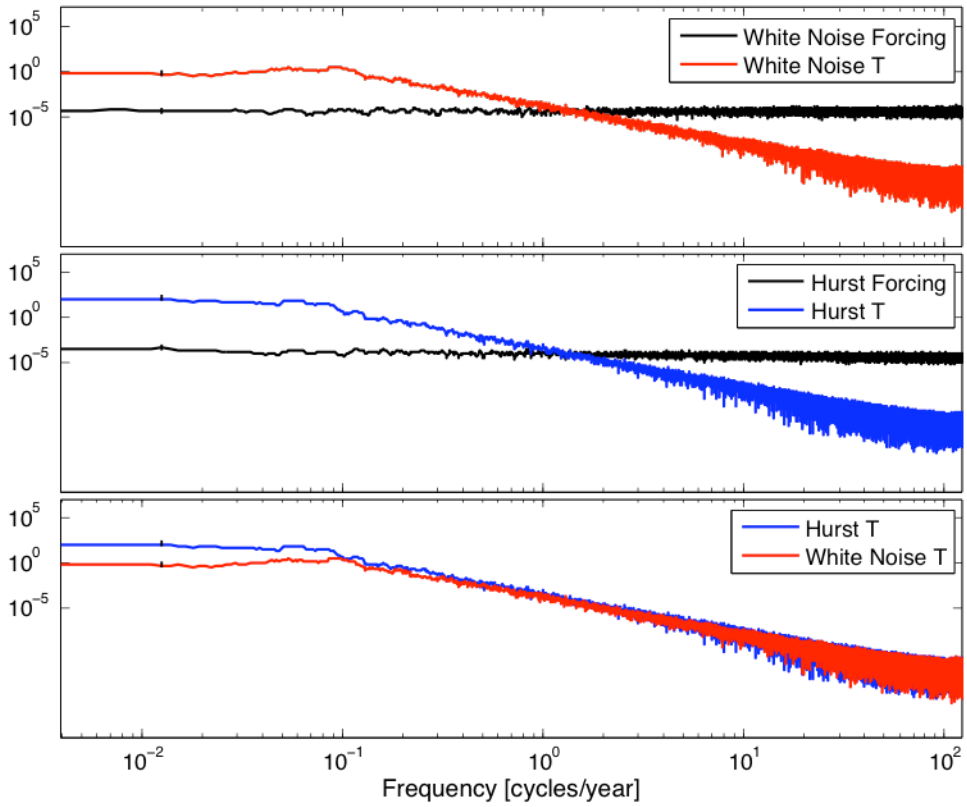

Figure B.11 Power spectra of the timeseries derived from synthetic (W2) and white noise (WW2) wind experiments, with panels displayed similarly to Figure B.9.

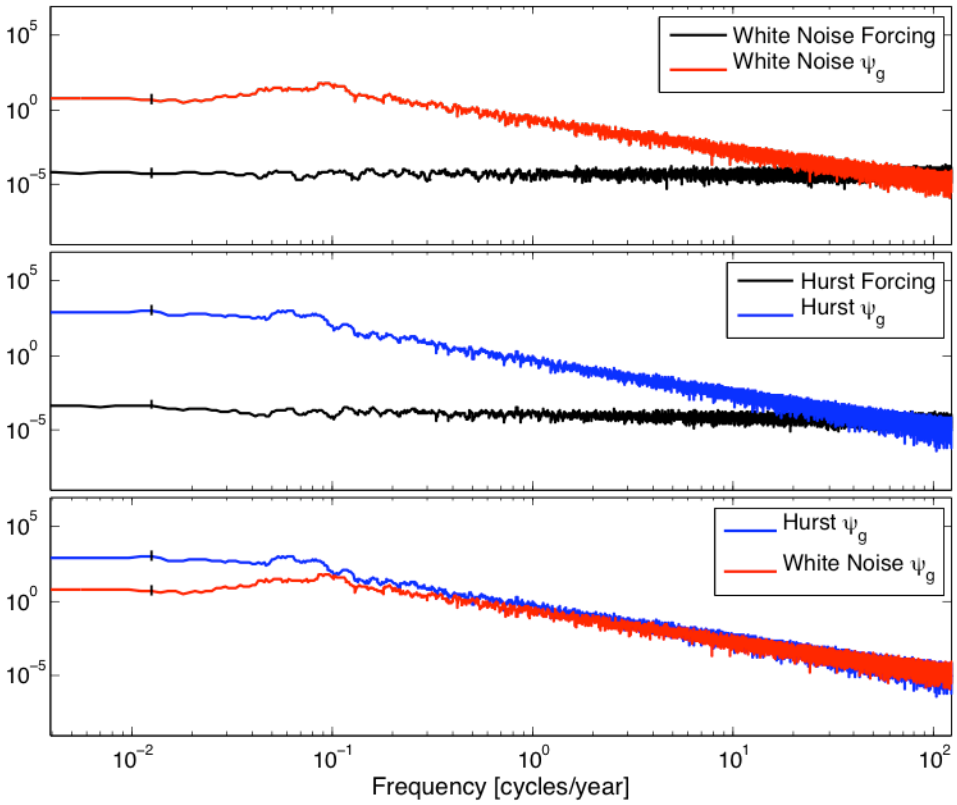

Figure B.12 Power spectra of the timeseries derived from synthetic (W2) and white noise (WW2) wind experiments, with panels displayed similarly to Figure B.10.

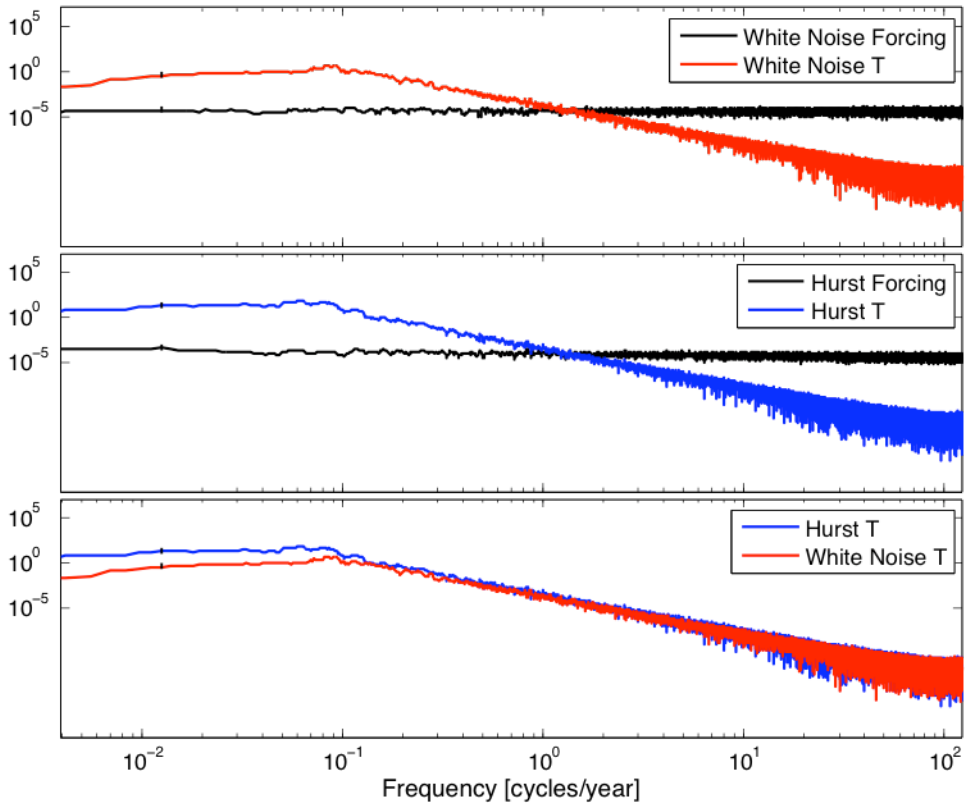

Figure B.13 Power spectra of the timeseries derived from synthetic (W3) and white noise (WW3) wind experiments, with panels displayed similarly to Figure B.9.

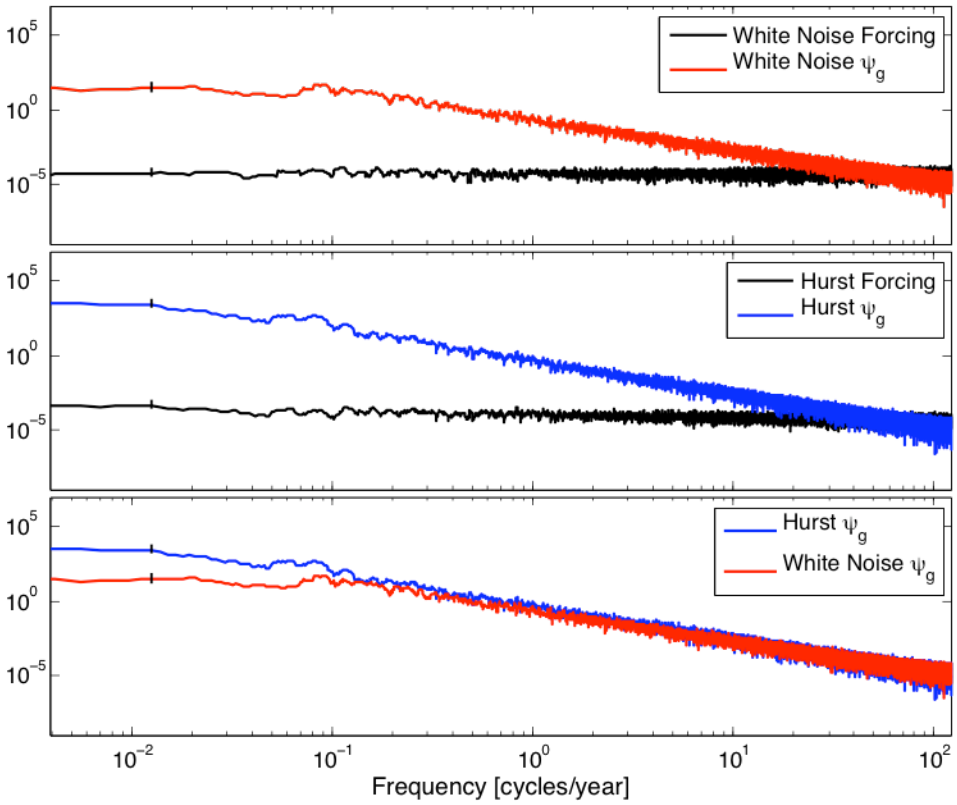

Figure B.14 Power spectra of the timeseries derived from synthetic (W3) and white noise (WW3) wind experiments, with panels displayed similarly to Figure B.10.

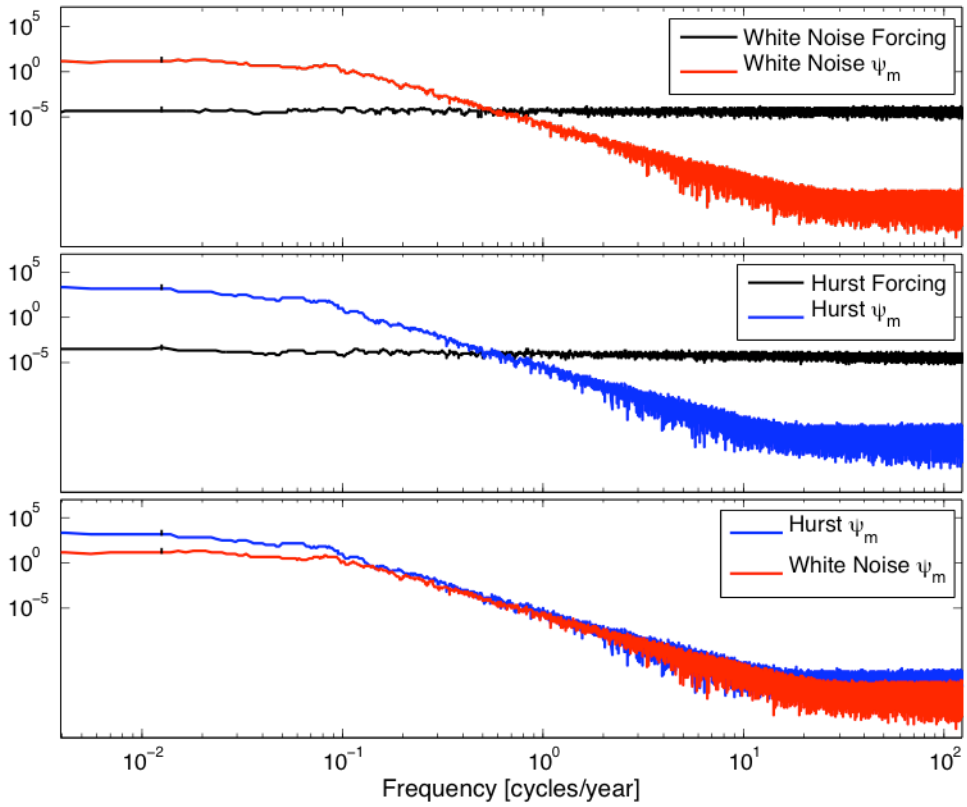

Figure B.15 Power spectra of the timeseries derived from synthetic (W3) and white noise (WW3) wind experiments, with panels displayed similarly to Figure B.9 with resulting MOC anomaly spectra.

Appendix C. SAT experiment

Similarly to Appendix B, this appendix provides the comprehensive set of figures associated with the SAT Experiments. The full set of synthetically forced SAT experiment model results are included (Figures C.1 - C.4) as well as the results of the most complete white noise forced SAT experiment (Figure C.5), with the results for each displayed on the same scales. Spectral analysis is also offered for the most complete SAT experiments (S4 and SS4) with their resulting temperature, MOC, and gyre anomaly spectra (Figures C.6 - C.8) for comparison.

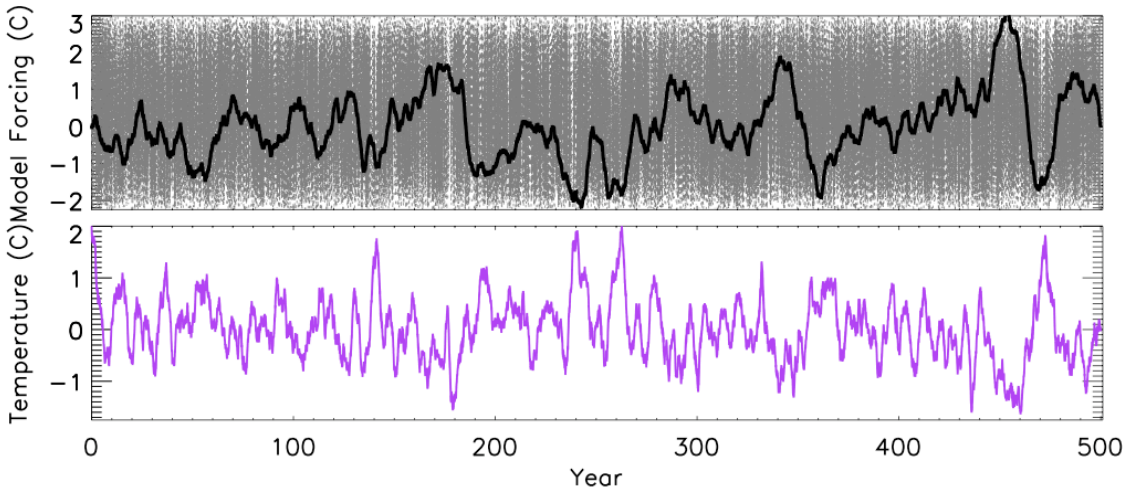

Figure C.1 Results of a 500-year model run for the synthetically forced SAT Experiment S1. (Top) synthetic daily (dashed line) and 7 year running mean (solid line) wind forcing (°C), (bottom) simulated response of SST anomalies (°C).

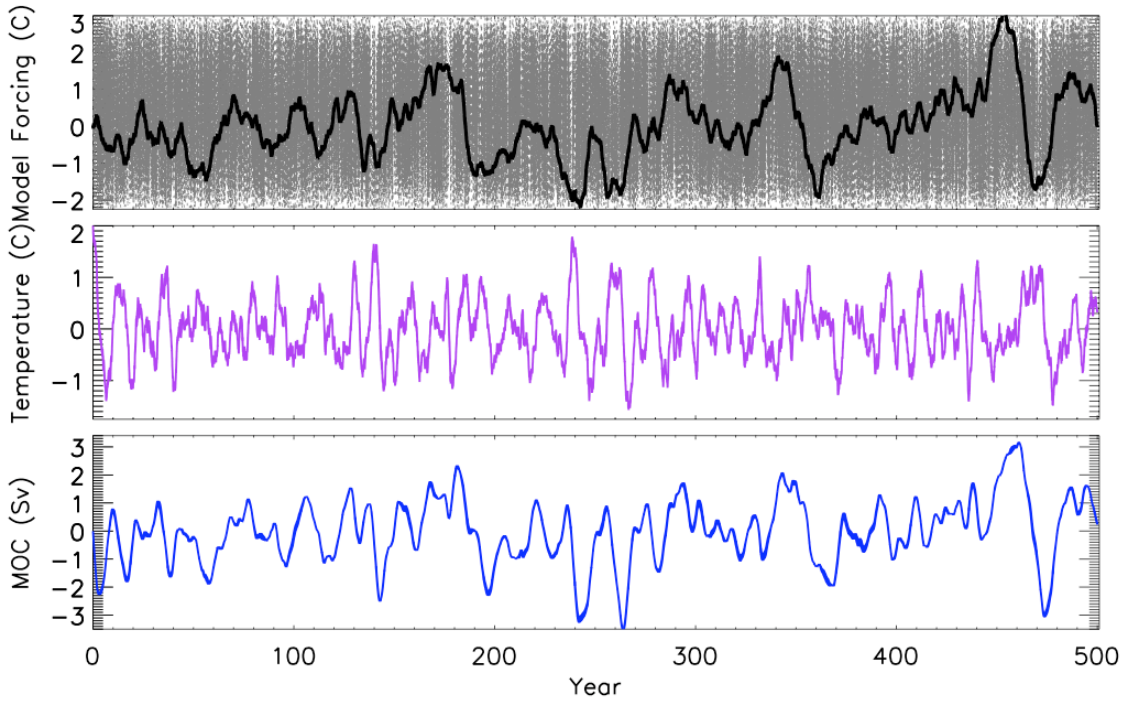

Figure C.2 Model results for the synthetically forced SAT Experiment S2. Figure panels are displayed as in Figure C.1, with the final panel displaying the simulated response of MOC anomalies (Sv).

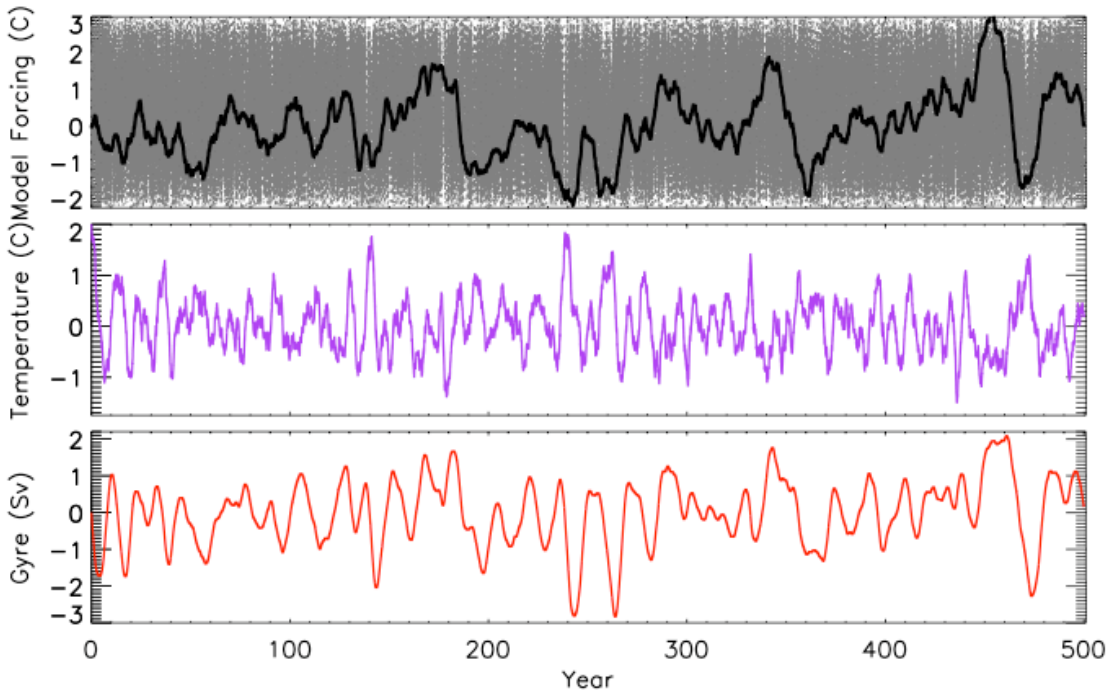

Figure C.3 Model results for the synthetically forced SAT Experiment S3. Figure panels are displayed as in Figure C.2, with the final panel instead displaying the simulated response of Gyre anomalies (Sv).

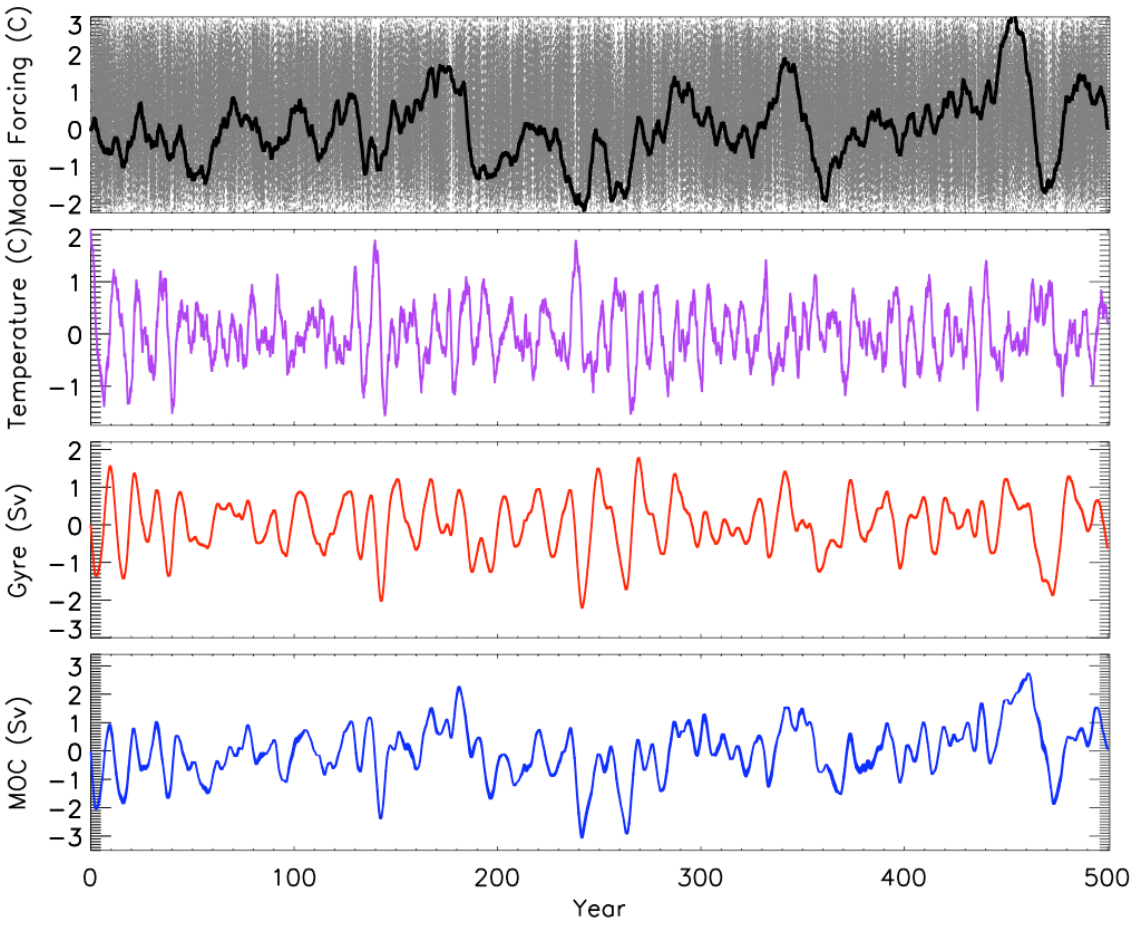

Figure C.4 Model results for the synthetically forces SAT Experiment S4. Figure panels are displayed as in Figure C.3, with the final panel displaying the simulated response of MOC anomalies (Sv).

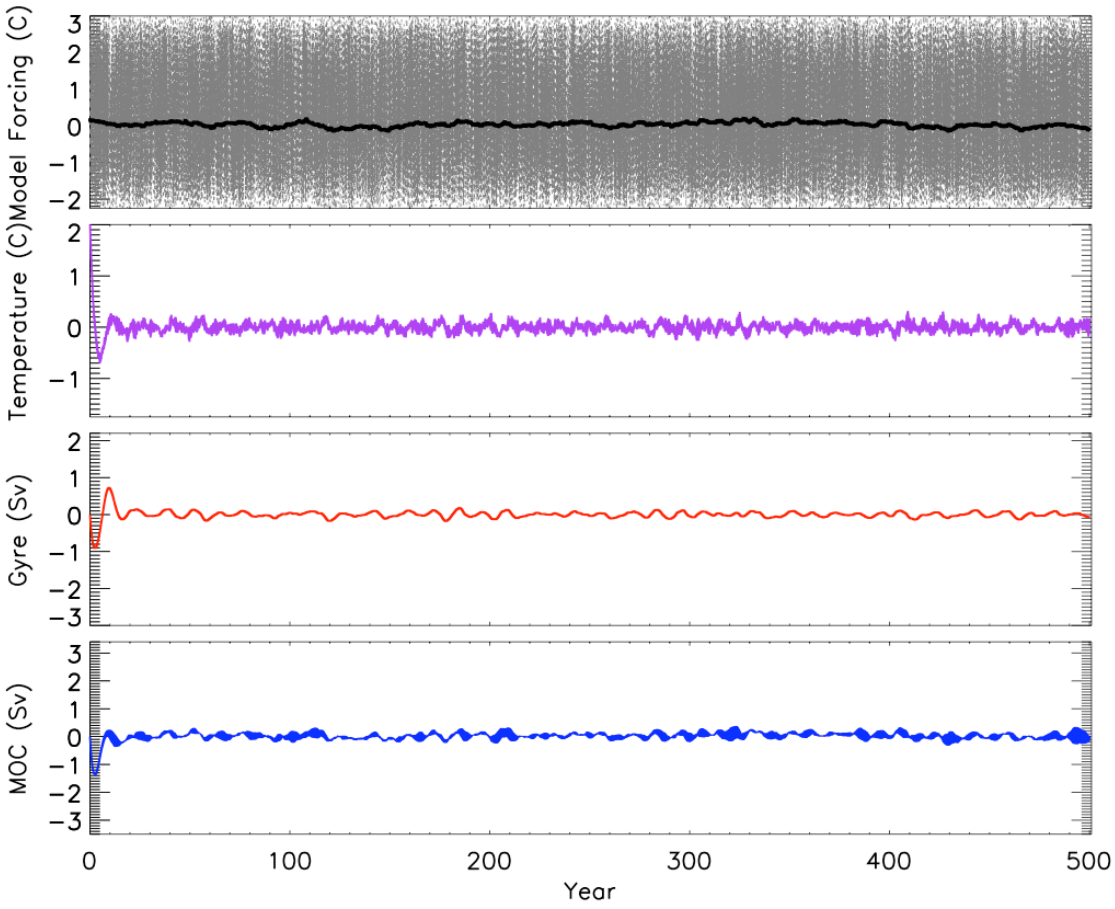

Figure C.5 Model results for the white noise forced SAT Experiment SS4. Figure panels are displayed as in Figure C.4.

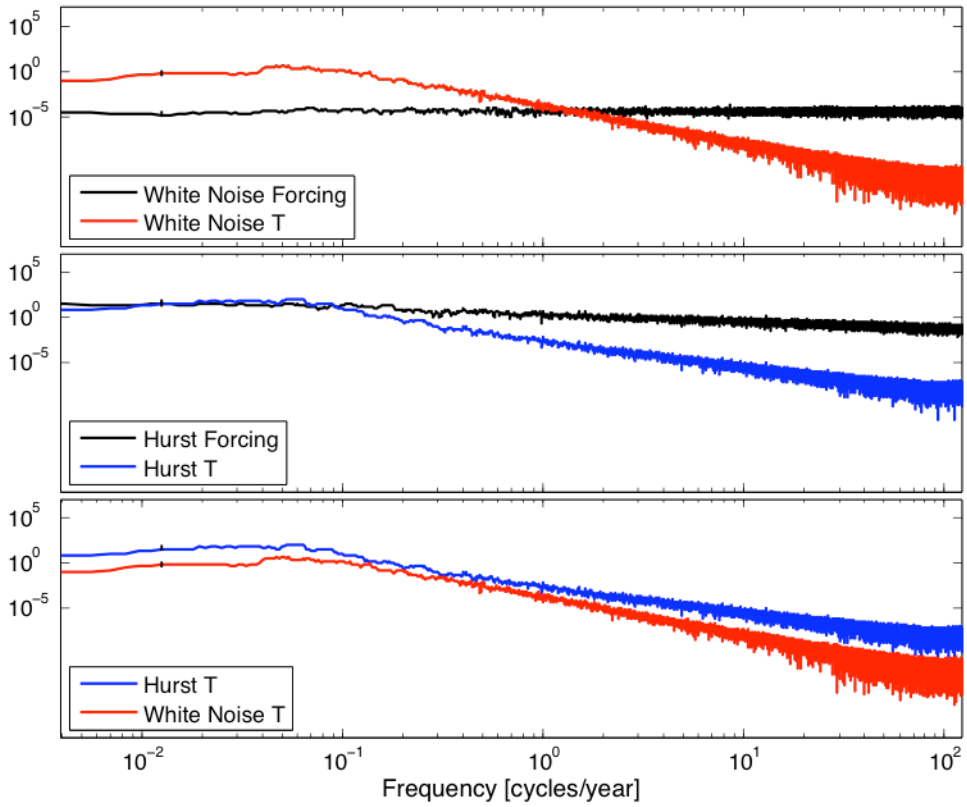

Figure C.6 Power spectra of the timeseries derived from synthetic (S4) and white noise (SS4) SAT experiments. (Top) SS4 (white noise) SAT forcing and SST spectra, (middle) S4 (synthetic) SAT forcing and SST spectra, and (bottom) comparison of spectra for SS4 and S4 SST responses.

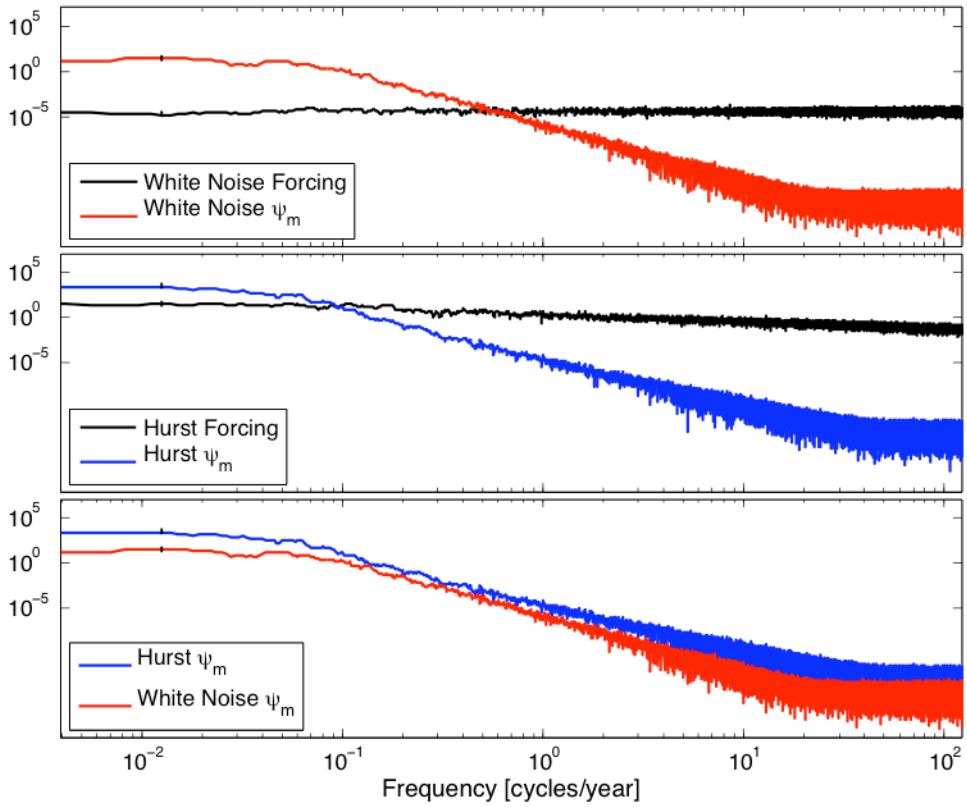

Figure C.7 Power spectra of the timeseries derived from synthetic (S4) and white noise (SS4) SAT experiments, with panels displayed similarly to Figure C.6 with resulting vertical MOC anomaly spectra.

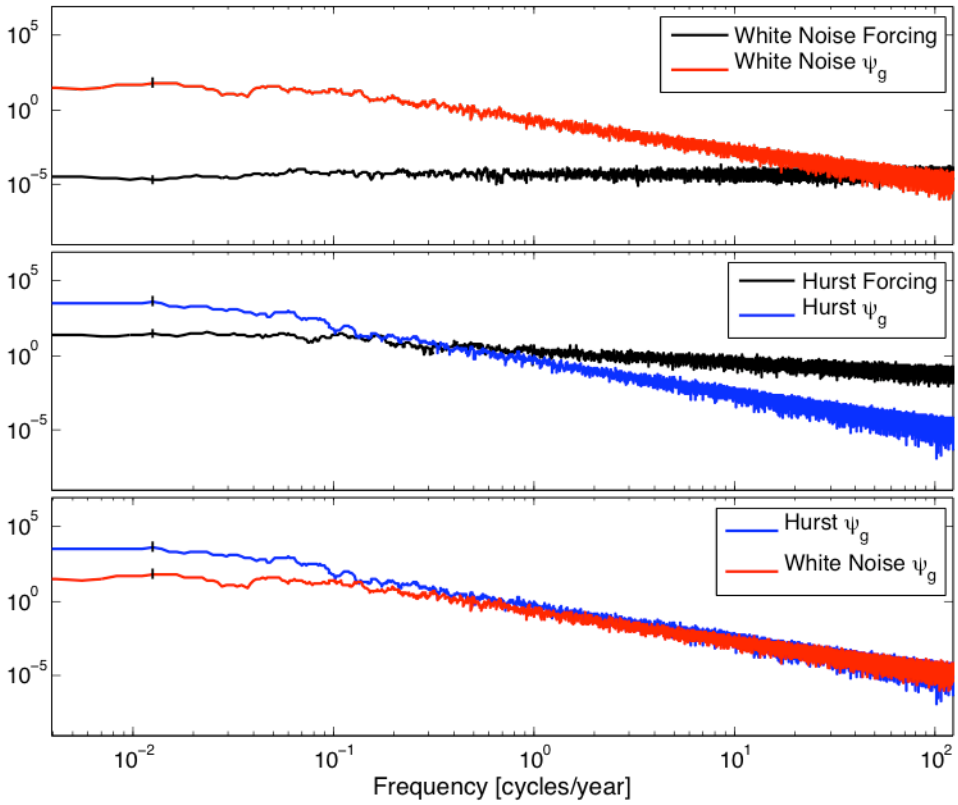

Figure C.8 Power spectra of the timeseries derived from synthetic (S4) and white noise (SS4) SAT experiments, with panels displayed similarly to Figure C.6 with resulting horizontal Gyre anomaly spectra.

Appendix D. Labrador experiment

This appendix completes the documentation of all model experiments completed during this study with the addition of the Labrador experiment results. The full set of synthetically forced Labrador experiment model results are included (Figures D.1 - D.4) as well as the results of the most complete white noise forced Labrador experiment (Figure D.5), with the results for each displayed on the same scales. Spectral analysis is also offered for the most complete Labrador experiments (L4 and LL4) with their resulting temperature, MOC, and gyre anomaly spectra (Figures D.6 - D.8) for comparison.

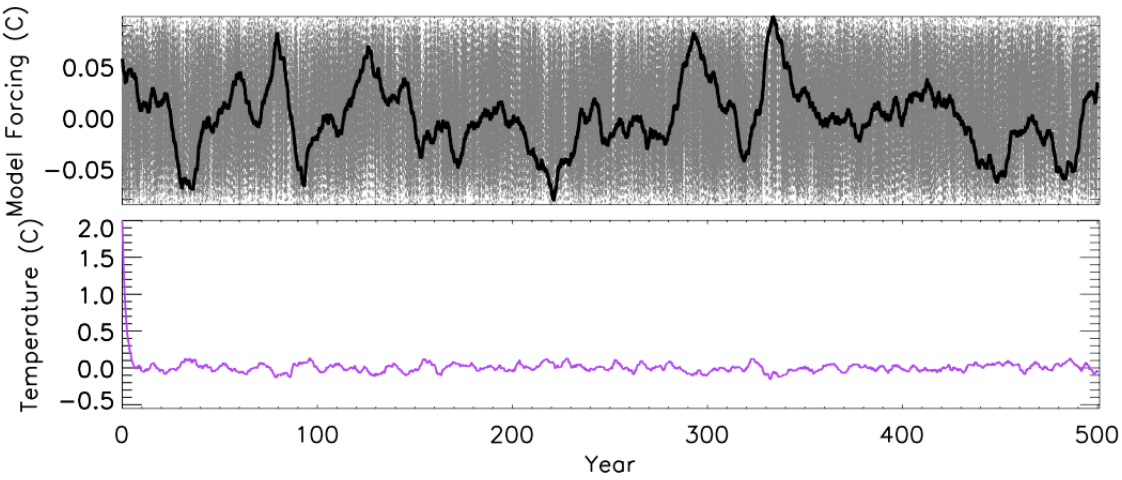

Figure D.1 Results of a 500-year model run for the synthetically forced Labrador Experiment L1. (Top) synthetic daily (dashed line) and 7 year running mean (solid line) Labrador forcing (°C), (bottom) simulated response of SST anomalies (°C).

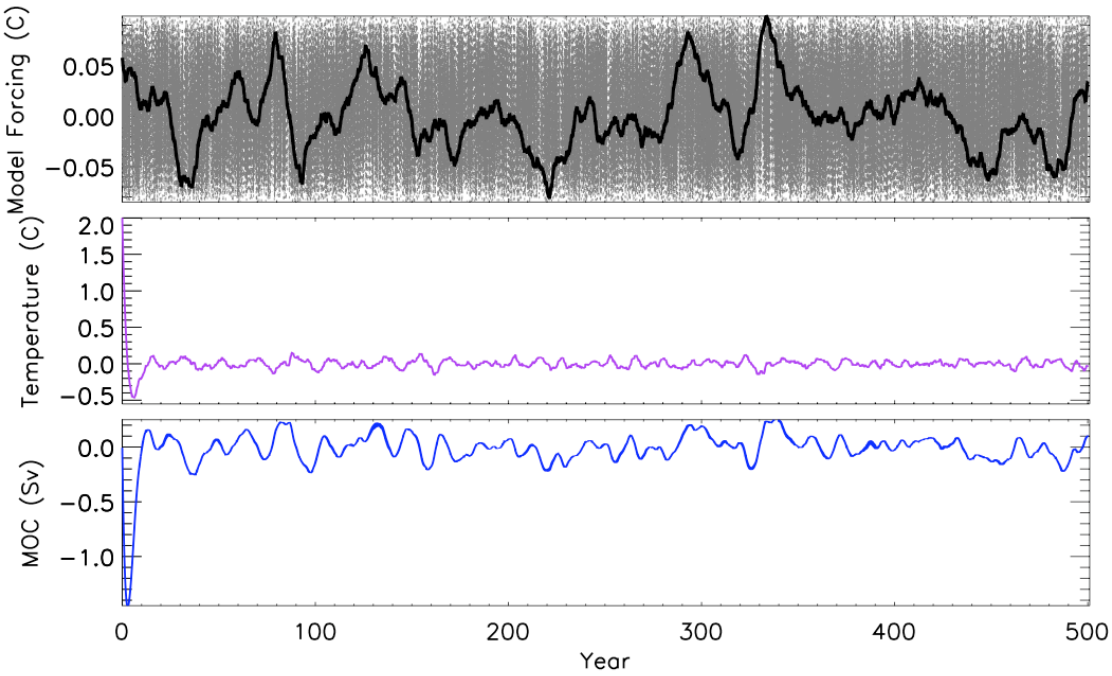

Figure D.2 Model results for the synthetically forced Labrador Experiment L2. Figure panels are displayed as in Figure D.1, with the final panel displaying the simulated response of MOC anomalies (Sv).

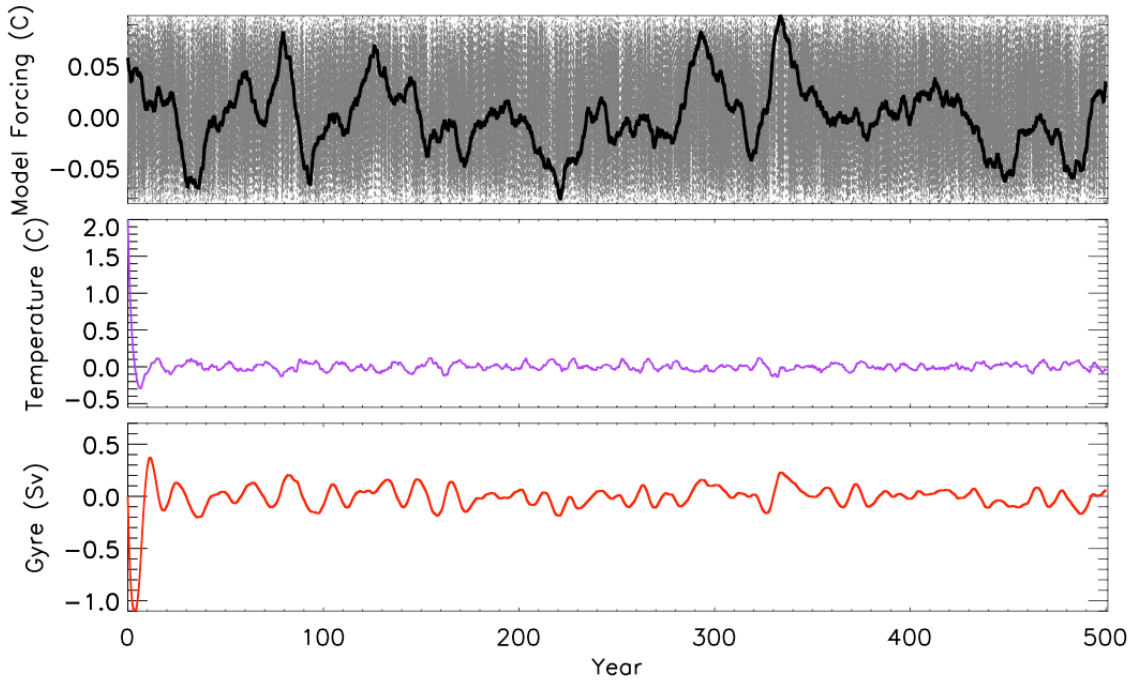

Figure D.3 Model results for the synthetically forced Labrador Experiment L3. Figure panels are displayed as in Figure D.1, with the final panel displaying the simulated response of horizontal Gyre anomalies (Sv).

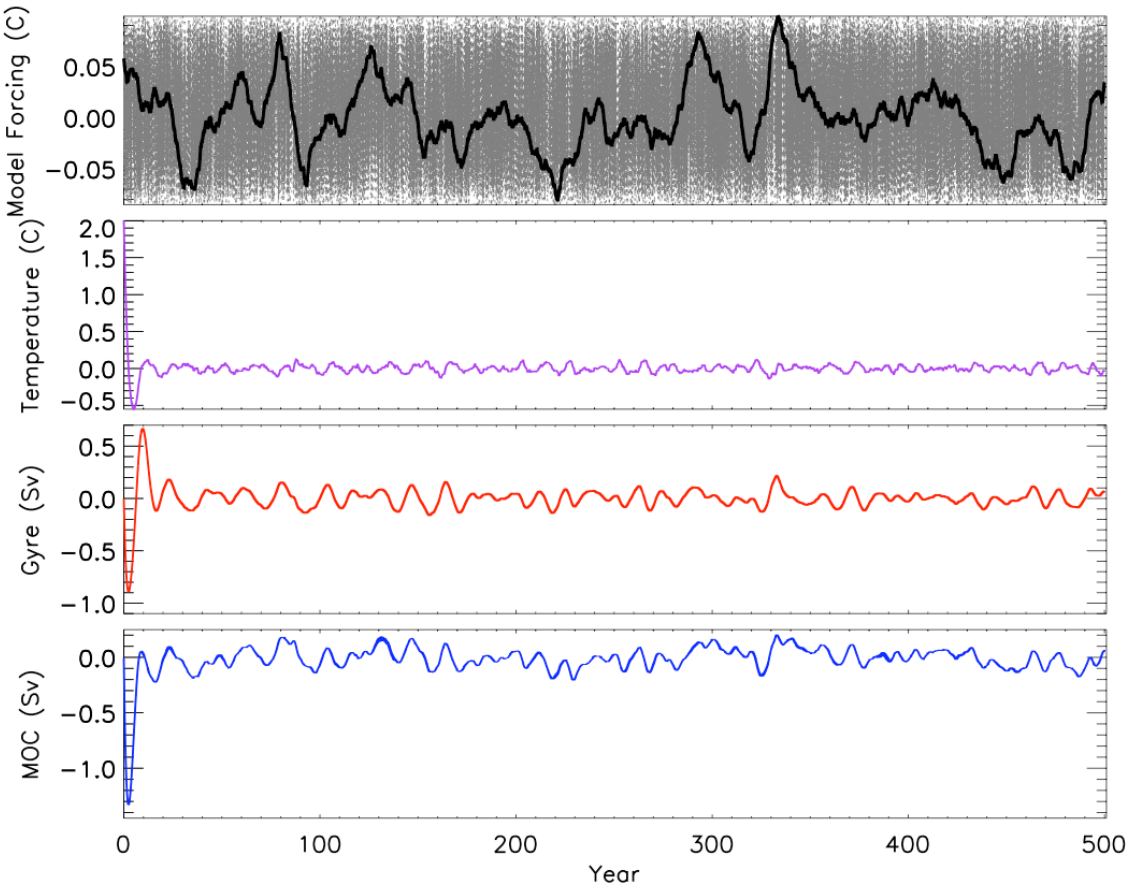

Figure D.4 Model results for the synthetically forces Labrador Experiment L4. Figure panels are displayed as in Figure D.3, with the final panel displaying the simulated response of MOC anomalies (Sv).

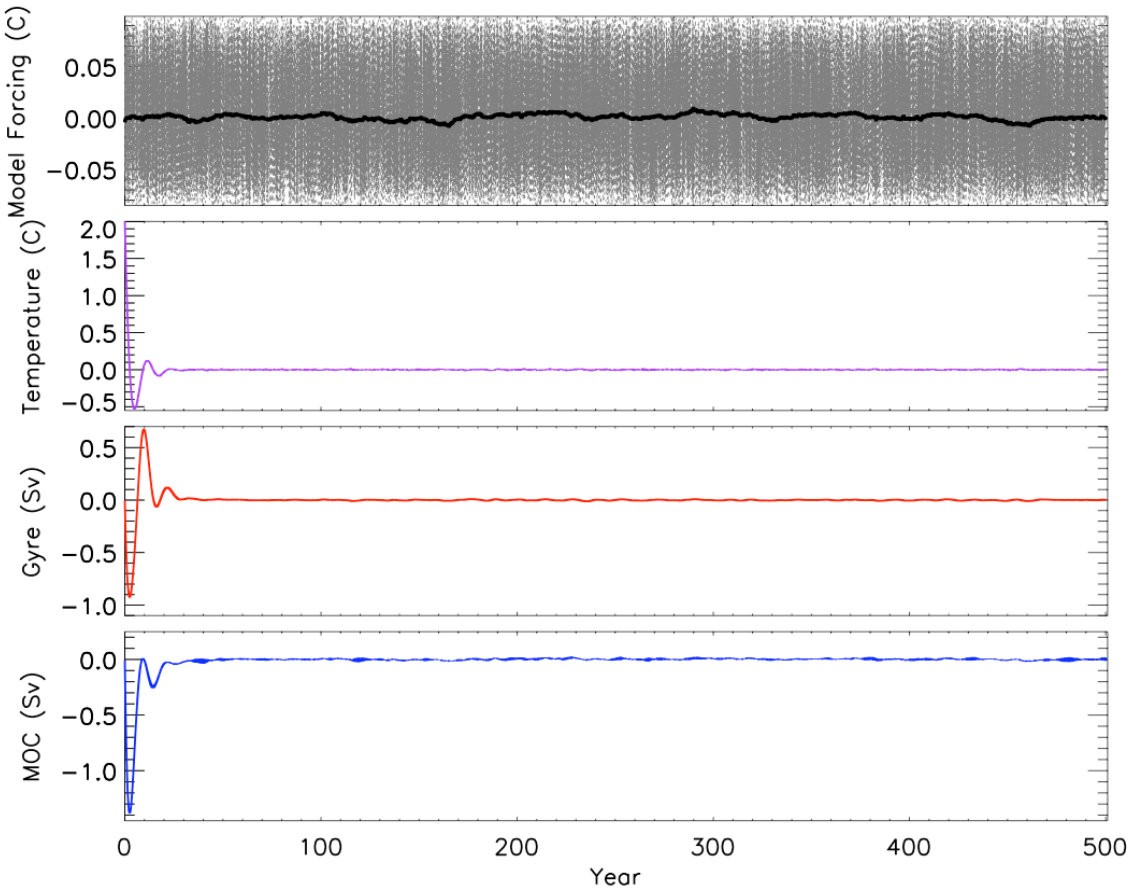

Figure D.5 Model results for the white noise forced Labrador Experiment LL4. Figure panels are displayed as in Figure D.4.

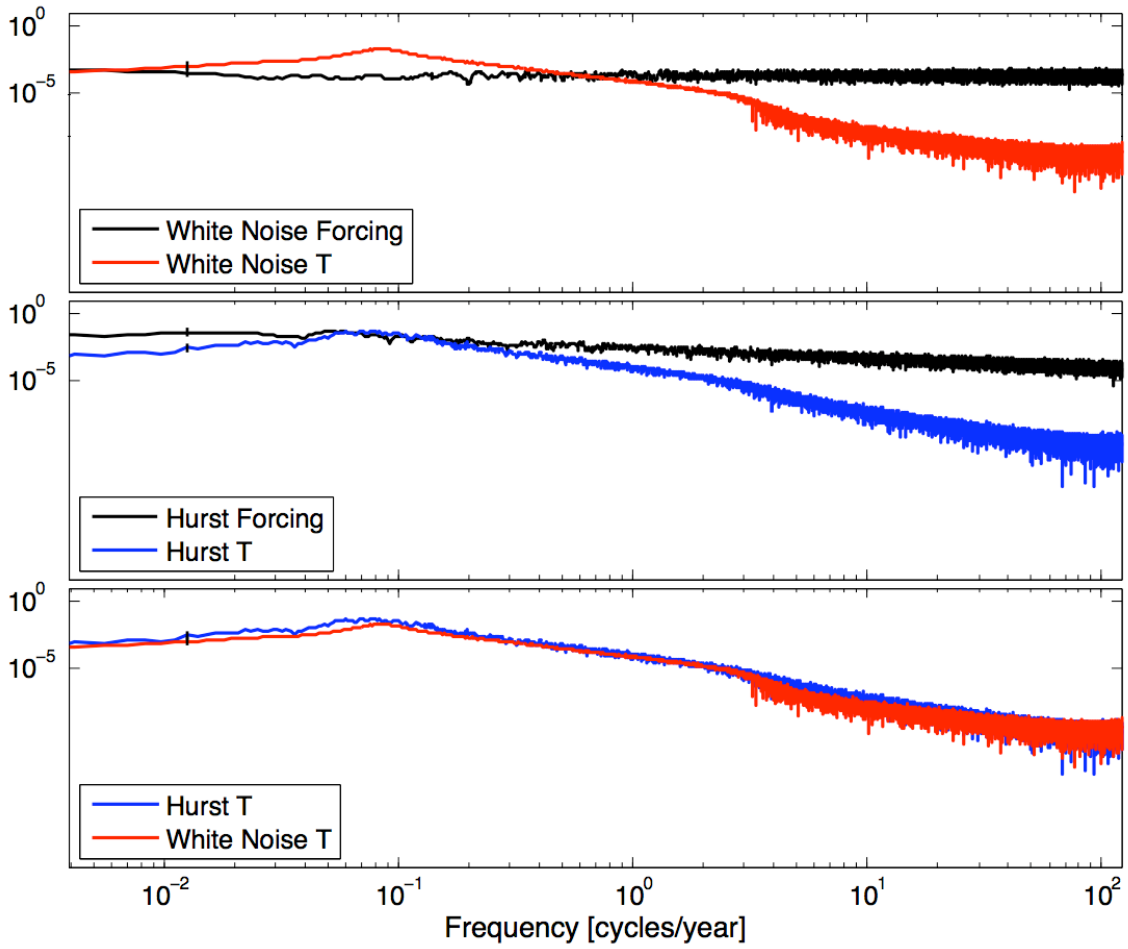

Figure D.6 Power spectra of the timeseries derived from synthetic (L4) and white noise (LL4) Labrador experiments. (Top) LL4 (white noise) Labrador forcing and SST spectra, (middle) L4 (synthetic) Labrador forcing and SST spectra, and (bottom) comparison of spectra for LL4 and L4 SST responses.

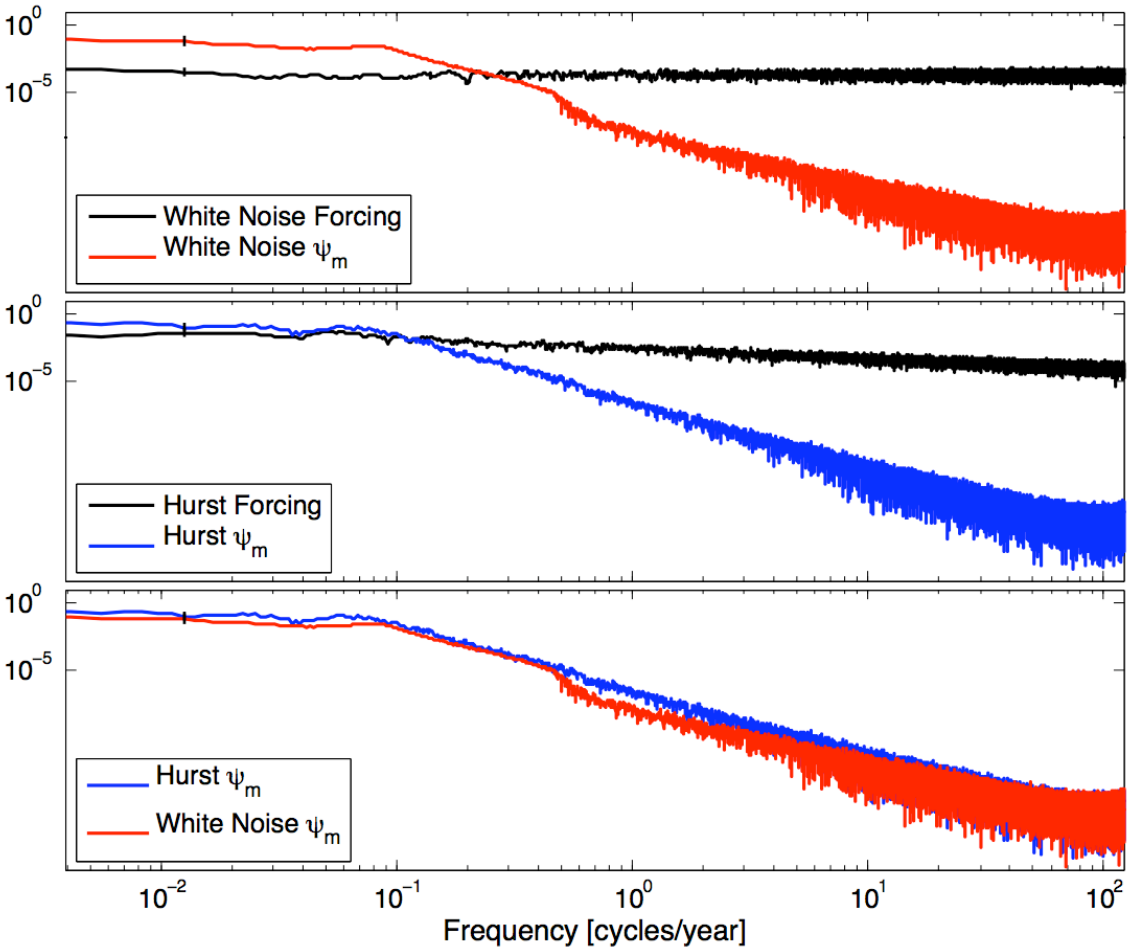

Figure D.7 Power spectra of the timeseries derived from synthetic (L4) and white noise (LL4) Labrador experiments, with panels displayed similarly to Figure D.6 with resulting vertical MOC anomaly spectra.

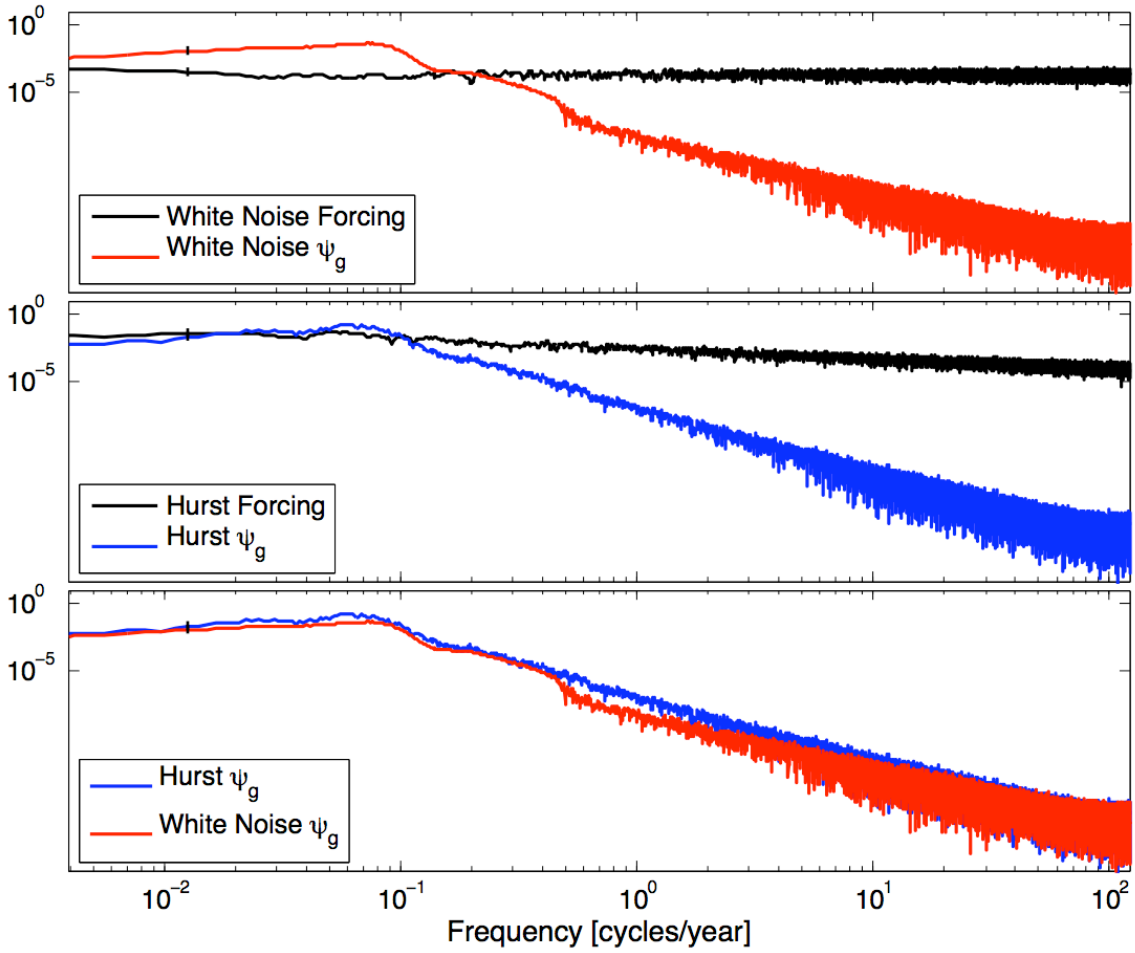

Figure D.8 Power spectra of the timeseries derived from synthetic (L4) and white noise (LL4) Labrador experiments, with panels displayed similarly to Figure D.6 with resulting horizontal Gyre anomaly spectra.